Doctoral Dissertation

Doctoral Program in Electrical, Electronic and Communications Engineering (38^{th}cycle)

Optical Networks for Environmental Surveillance and Early Warning Systems

By

Hasan Awad

******

Supervisor(s):

Prof. Vittorio Curri, Supervisor

Prof. Roberto Proietti, Co-Supervisor

Dr. Emanuele Virgillito ,Co-Supervisor

Doctoral Examination Committee:

Dr. Élie Awwad, External Reviewer, Télécom Paris, Polytechnic Institute of Paris, Paris, France and Dr. Roger Abou-Jaoude, External Reviewer, CTO at CITC, Critical Infrastructure Technologies Consultancy LLC - Abu Dhabi, United Arab Emirates

Politecnico di Torino

2026

Declaration

I hereby declare that, the contents and organization of this dissertation constitute my own original work and does not compromise in any way the rights of third parties, including those relating to the security of personal data.

Hasan Awad
2026

* This dissertation is presented in partial fulfillment of the requirements for **Ph.D. degree** in the Graduate School of Politecnico di Torino (ScuDo).

The foundation of every journey begins with its vision,
but its continuation lies in faith, dedication, and sacrifice.
Pursuing a PhD is not only a title to be earned,
it is a lifestyle, an elevation of purpose, public relations, and a dialogue
between what drives us and what challenges us.
To dedicate this milestone only to myself would be an act of arrogance;
the silent force behind every word in this thesis is from the people who
supported me, pushed me forward and sustained my spirits.
Blessed to have you all! Thank you!

Acknowledgements

I would like to acknowledge Politecnico di Torino for its excellence in academics and research; Prof. Vittorio Curri, a pragmatic leader and an academic mentor, and my co-supervisors - Prof. Roberto Proietti and Dr. Emanuele Virgillito. I extend this acknowledgment to colleagues and fellows for making the PLANET team's environment inspiring, collaborative, and productive. Special thanks to Mr. Stefano Straullu from LINKS Foundations, and Dr. Rudi Bratovich from SM-Optics, for their invaluable support and contributions.

Abstract

Optical fiber networks, commonly known for data communications can be extended beyond their conventional use. Modern coherent transceivers based on digital signal processing already track the evolution of the transmitted optical signal phase and polarization to recover the transmitted data at the receiver side. As those quantities are strongly affected by external strain, they already contain environmental information. To fulfill modern traffic requirements, optical networks are evolving towards multi-service autonomous, flexible, and software defined entities based on a centralized intelligence, enabling the orchestration of network functionality to communicate with network elements using standardized interfaces. This trend opens the perspective to exploit these networks for environmental sensing. In this thesis, we propose an optical data network architecture that exposes sensing functionalities with minimum or no additional hardware. Our focus is on light's polarization-based environmental sensing, with a special focus on early disaster warning. This thesis demonstrates computer-based simulation, followed by a laboratory-based experiment, to conclude with an in-field testing. In-field testing, not only showcase seismic wave detection, but also demonstrates other manual induced external events that might occur in everyday environments. The sensing system can co-exist with WDM networks, without interfering with communication services or even impose any network security threat. We achieve high accuracy in early earthquake detection, distinguishing its impact on polarization from a car passage to mimic real-world noisy environment. Transforming the existing fiber infrastructure into a large-scale sensing and localization grid, allows a country to re-purpose deployed telecommunications assets for early warning systems, oil & gas pipeline leakage, infrastructure monitoring, human activity monitoring, or security-relevant applications, supporting the vision of smart cities and national resilience frameworks.

Contents

List of Figures

List of Tables

List of Scientific Publications

A list of scientific contributions, including Journal and conference papers, with a special focus on the work carried out during the PhD, is presented here.

Publications Included in this PhD Thesis

Peer Reviewed International Journals

[1] H. Awad, F. Usmani, E. Virgillito, R. Bratovich, R. Proietti, S. Straullu, F. Aquilino, R. Pastorelli, and V. Curri. Environmental Surveillance through Machine Learning-Empowered Utilization of Optical Networks. Sensors. 2024; 24(10):3041. https://doi.org/10.3390/s24103041

Conference Publications Included in this PhD Thesis

[1] F. Usmani, H. Awad, S. Straullu, R. Bratovich and E. Virgillito F. Aquilino R. Proietti, and V. Curri. "Deep Learning Based Early Earthquake Detection through Terrestrial Optical Networks," 2025 25th Anniversary International Conference on Transparent Optical Networks (ICTON), Barcelona, Spain, 2025, pp. 1-6.

[2] H. Awad, R. Bratovich, S. Straullu, F. Usmani, E. Virgillito, F. Aquilino R. Proietti, F. Carpentieri, M. Hovsepyan, S. Gastaldello, and V. Curri. "Experimental Validation on Using Optical Network-as-a-Sensor for Earthquake Early Warning," 2025 International Conference on Optical Network Design and Modeling (ONDM), Pisa, Italy, 2025, pp. 1-5.

[3] H. Awad, F. Usmani, S. Straullu, R. Bratovich, E. Virgillito, F. Aquilino, R. Proietti, and V. Curri. "Experimental Validation for Early Earthquake Detection Using Transfer Learning," 2025 Optical Fiber Communications Conference and Exhibition (OFC), San Francisco, CA, USA, 2025, pp. 1-3.

[4] H.Awad, S. Straullu, F. Usmani, E. Virgillito, R. Bratovich, F. Aquilino, R. Proietti, V. Curri. "Experimental earthquake early detection through polarization changes in intelligent optical networks," Proc. SPIE 13310, Optical Fibers and Sensors for Medical Diagnostics, Treatment, and Environmental Applications XXV, 133100L (20 March 2025); **Invited Paper**.

[5] H. Awad, F. Usmani, E. Virgillito, R. Bratovich, S. Straullu, F. Aquilino, R. Proietti, R. Pastorelli, and C. Curri. "Machine Learning-Driven Earthquake Early Warning Using Optical Fiber Mesh Networks," - (2024), pp. 1-2. (2024 IEEE Photonics Conference, IPC 2024 Roma (Ita) 10-14 November, 2024), doi: https://doi.org/10.1109/ipc60965.2024.10799809.

[6] H. Awad, F. Usmani, E. Virgillito, R. Bratovich, S. Straullu, F. Aquilino, R. Proietti, R. Pastorelli and V. Curri. "Artificial Intelligence Driven Earthquakes Early Detection in Noisy Urban Areas," IEEE Middle East Conference on Communications and Networking (MECOM), Abu Dhabi, United Arab Emirates, 2024, pp. 65-70.

[7] H. Awad, F. Usmani, E. Virgillito, R. Bratovich, S. Straullu, F. Aquilino, R. Proietti, R. Pastorelli, and V. Curri. "Polarization-Based Sensing in Mesh Optical Networks for Early Earthquake Detection," ECOC 2024; 50th European Conference on Optical Communication, Frankfurt, Germany, 2024, pp. 1672-1675.

[8] H. Awad, F. Usmani, E. Virgillito, R. Bratovich, R. Proietti, S. Straullu, R. Pastorelli, and V. Curri. "A Machine Learning-Driven Smart Optical Network Grid for Earthquake Early Warning," 2024 24th International Conference on Transparent Optical Networks (ICTON), Bari, Italy, 2024, pp. 1-6, doi: https://doi.org/10.1109/ICTON62926.2024.10648206.

[9] E. Virgillito, H. Awad, F. Usmani, S. Straullu, R. Bratovich, R. Proietti, R. Pastorelli, and V. Curri. Environmental Sensing and Detection based

on State of Polarization Monitoring in Terrestrial Optical Data Networks, Galileo conference: Fibre Optic Sensing in Geosciences, Catania, Italy, 16–20 Jun 2024, GC12-FibreOptic-8, https://doi.org/10.5194/egusphere-gc12-fibreoptic-8, 2024.

[10] F. Usmani, H. Awad, E. Virgillito, R. Bratovich, S. Straullu, F. Aquilino, R. Proietti, R. Pastorelli, and V. Curri. "Earthquake Early Warning through Terrestrial Optical Networks: A Bi-GRU Attention Model Approach on SOP Data," in Optical Fiber Communication Conference (OFC) 2024, Technical Digest Series (Optica Publishing Group, 2024), paper Tu3J.2.

[11] H. Awad, F. Usmani, E. Virgillito, R. Bratovich, R. Proietti, S. Straullu, R. Pastorelli, and V. Curri. "Seismic detection through state-of-polarization analysis in optical fiber networks," Proc. SPIE 12835, Optical Fibers and Sensors for Medical Diagnostics, Treatment, and Environmental Applications XXIV, 128350L (12 March 2024); https://doi.org/10.1117/12.3007808. **Invited Paper**.

[12] H. Awad, F. Usmani, E. Virgillito, R. Bratovich, S. Straullu, R. Proietti, R. Pastorelli, and V. Curri. "Smart Grid Optical Fiber Network for Earthquake Early Warnings", EGU General Assembly 2024, Vienna, Austria, 14–19 Apr 2024, EGU24-4418, https://doi.org/10.5194/egusphere-egu24-4418, 2024.

[13] E. Virgillito, H. Awad, R. Bratovich, S. Straullu, R. Proietti, R. Pastorelli, and V. Curri. "Earthquake Emulation for Environmental Sensing in Terrestrial Telecom Networks," in Frontiers in Optics + Laser Science 2023 (FiO, LS), Technical Digest Series (Optica Publishing Group, 2023), paper FM1D.4.

[14] E. Virgillito, S. Straullu, F. Aquilino, R. Bratovich, H. Awad, R. Proietti, M. F. Rodriguez, R. Pastorelli, and V. Curri. "Detection and Localization of Metropolitan Anthropic Activities by SOP Monitoring of IM-DD Optical Data Channels," 2023 International Conference on Photonics in Switching and Computing (PSC), Mantova, Italy, 2023, pp. 1-3.

[15] H. Awad, E. Virgillito, S. Straullu, R. Bratovich, F. M. Rodriguez, R. Proietti, A. D'Amico, F. Aquilino, R. Pastorelli, and V. Curri. "En-

vironmental Sensing and Localization via SOP Monitoring of IM-DD Optical Data Channels," in Optica Sensing Congress 2023 (AIS, FTS, HISE, Sensors, ES), Technical Digest Series (Optica Publishing Group, 2023), paper JTu4A.8.

[16] E. Virgillito, S. Straullu, F. Aquilino, R. Bratovich, H. Awad, R. Proietti, A. D'Amico, R. Pastorelli, and V. Curri. "Detection, Localization and Emulation of Environmental Activities Using SOP Monitoring of IMDD Optical Data Channels," 2023 23rd International Conference on Transparent Optical Networks (ICTON), Bucharest, Romania, 2023, pp. 1-4, doi: 10.1109/ICTON59386.2023.10207513.

[17] E. Virgillito, S. Straullu, R. Bratovich, F. M. Rodriguez, H. Awad, A. Castoldi, R. Proietti, A. D'Amico, F. Aquilino, R. Pastorelli, and V. Curri. Exploiting Terrestrial Meshed Optical Data Networks as Environmental Sensing Smart Grids, EGU General Assembly 2023, Vienna, Austria, 24–28 Apr 2023, EGU23-6998, https://doi.org/10.5194/egusphere-egu23-6998, 2023.

Publications Not-Included in this PhD Thesis

Conference Publications Not-Included in this PhD Thesis

[1] A. Marchisio, L. Tunesi, H. Awad, E. Ghillino, V. Curri, A. Carena, and P. Bardella. "Comprehensive thermal crosstalk model of meshed MZI topologies for neuromorphic computing," Proc. SPIE 13375, AI and Optical Data Sciences VI, 133750F (21 March 2025); https://doi.org/10.1117/12.3043230

[2] L. Tunesi, H. Awad, A. Carena, V. Curri, and P. Bardella. "Toggleable transparency states in thermally-shifted multiMRR cascaded filters," Proc. SPIE 13371, Silicon Photonics XX, 133710T (20 March 2025).

Chapter 1

Introduction

In the early to mid 1960s, the pioneering work of Kao and Hockham had a profound impact on the communications industry [1]. They recognized that optical signals could be transmitted along glass or silica fibers with losses potentially lower than those in coaxial copper cables. Kao and Hockham's breakthrough laid the foundation of modern optical fiber networks, which have become the backbone of global communications with high-speed data transmission. The resultant information-driven era enables real-time analytics, predictive modeling, and automation, while also paves the way to exploit the entire network beyond its conventional use. Building on this foundation, optical fiber infrastructure used for data transmission can serve as a versatile array of sensors capable of detecting external events [2]. Due to applied mechanical stress and through the photoelastic effect, the local refractive index of the fiber core changes and give rise to birefringence. Fiber birefringence supports different propagation speeds of the optical wave along the x and y axes of the fiber core. This velocity mismatch leads to measurable changes in the polarization and phase of the transmitted light. Intelligent analytical algorithms on top of the velocity mismatch can define, detect and localize external perturbations. These perturbations can be, vibration, strain, or even temperature changes, as they modulate the optical wave's physical properties as it travels through the fiber. Devices like Re-Configurable Add/Drop Multiplexers and amplifiers include crucial information like power levels and temperature variations, whereas devices like coherent transceivers capture alterations in phase and polarization of optical signals. Even if these transceivers are inaccessible due to vendor lock, intensity modulated-direct detected optical signals can still be monitored. Monitoring phase and polarization has led to the development of several sensing techniques collectively known as Distributed Fiber Optics Sensing (DFOS) techniques. These techniques provide the capability of measuring slow-varying environmental variables, which can be influenced by external events, at any point along the fiber's length with a given sharp spatial resolution. The global DFOS market size was valued at USD 1.40 billion in 2024 and is projected to reach USD 2.8 billion by 2030, growing at a Compound Annual Growth Rate of 11.4% from 2025 to 2030. DFOS is driving increased investments and development efforts by enterprises world-wide due to their broad applications across various industries, including Energy, Oil & Gas, Civil, Aerospace, Seismology and others, enabling real-time data-driven monitoring [3].

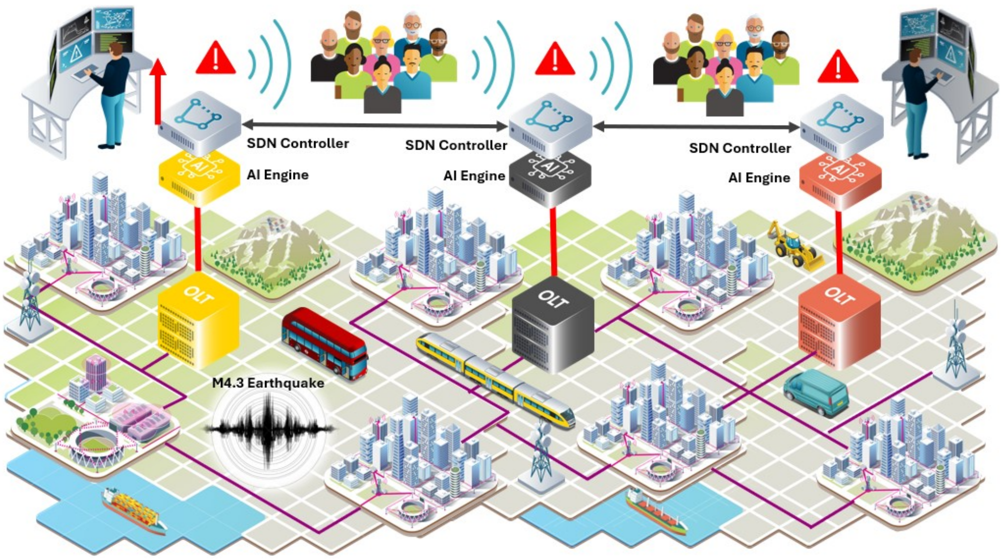

Fig. 1.1 AI-enabled sensing using existing optical fiber telecommunications networks. The core idea is to transform national fiber infrastructure into a large-scale sensing grid, capable of monitoring external events beyond traditional communications. Such an approach allows a country/city to repurpose deployed telecommunications assets for early disaster warning, infrastructure protection, human activity monitoring, and security-relevant applications, without the need for additional field sensors. These techniques are already attracting strong international interest in oil & gas, defense, smart cities, and national resilience frameworks.

Optical Network-as-a-Sensor plays a vital role in supporting the vision of smart cities, enabling a foundational intelligent and environment-aware infrastructure. The *Killer App* here is that optical fiber cables are extensively deployed around the globe, capable of driving a paradigm shift of how these cables can be utilized beyond their conventional telecommunications use. Cities, being dense concentration of human activity, have drawn increased research attention aimed at informing urban policy, improving quality of life, and driving long-term sustainability. Within this context, the development of effective disaster early warning systems has emerged as a central requirement for resilient urban environments.

Among nature hazards, Earthquakes represent one of the greatest threats to human life and built infrastructure. According to plate tectonics theory, the earth's lithosphere is divided into plates by seismic zones that move relative to each other. The majority of earthquakes occur along these plates' boundaries, with seismogenic faults being the geological origins of destructive earthquakes [4]. However, predicting earthquakes is a common scientific challenge for researchers globally. Much of this difficulty stems from the lack of reliable precursory indicators that meet the sufficient and necessary conditions of their occurrence, which is often considered the primary cause of failure in earthquake prediction efforts in earth science research. However, monitoring these seismic events is an essential part in trying to predict them, and that employs range of different methods. For instance, absolute measurement of geostress was done to assess the stress characteristics of significant faults [5], seen in the San Andreas Fault Observatory at Depth (SAFOD) project [6]. Li Siguang, a pioneer of earthquake prediction in China, pointed out that an earthquake is a process of accumulation of stress on seismogenic faults. Real time monitoring of geostress using tools like stress gauges can be leveraged to track changes in fault lines, providing insights into the release of seismic energy [7]. Crustal strain monitoring through strain gauges and GPS technology have been developed for seismic research and prediction as well [8, 9]. Additionally, infrared monitoring method, as the infra-sound signal in the far field is found to be strong within two to eleven days before an earthquake with a magnitude of M7.0 or higher strikes, and its spectral characteristics are apparently different from other natural events [10]. In 1988, seismologists in the United States deployed a dense network of monitoring stations focused mainly on "Surface Strain Monitoring", in addition to tracking geo-magnetic, geo-electric, ground-water level, and hydro-chemistry data, to predict an M6 earthquake occurring in the Park-field near the San Andreas fault. Yet, the anticipated earthquake didn't occur until 2004, 16 years later than expected, and the monitoring equipment failed to pick up any anomalies or precursors [11]. Similarly, in 1995, an M7 earthquake struck in Hanshin, Japan, killing more than 6500 people, where the high density GPS network in place did not capture warning signals. Consequently, the scientific community become increasingly skeptical about earthquake prediction. In March 1997, Robert J. Geller published a paper titled, "Earthquakes cannot be predicted" in Science magazine, which reflected the prevailing opinion on earthquake prediction efforts [12]. Therefore, it is crucial to address this challenge differently by adopting novel methods for widely distributed early detection systems capable of rapidly identifying the event. The first development of an Earthquake Early Warning System (EEWS) dates back to the 1960s, when Japan pioneered the UrEDAS system, designed to provide railroad warnings by utilizing seismic stations to detect ground motion induced by the arrival of primary earthquake wave that precedes the destructive surface wave by tens of seconds, allowing warnings to be issued before severe shaking occurs [13]. However, the global density of seismic stations is low, leading to a poor spatial sampling analysis of seismic activity. Moreover, the cost of deploying and maintaining a larger, denser, and homogeneous network of these stations pose great economic challenges, making this solution impractical even for highly developed nations [14]. In this context, the utilization of optical fiber networks presents a promising new direction. Primary earthquake waves propagate through earth's interior and precede destructive Surface waves that propagate along the Earth's surface. Surface waves carry the greatest amount of energy and are usually the primary cause of destruction [15]. Such changes in the Earth's crust are indicative of stress accumulation, potentially pointing towards upcoming seismic event. Consequently, as optical fiber cables are buried underground, they too experience stretching or compression in response to the strain rate change caused by these events, thus altering light's polarization and phase, and enabling the fiber infrastructure to act as a distributed sensing medium. Detecting Primary waves allows prompt initiation of emergency plans and earthquake counter-measures. These systems can be at the forefront of smart cities concepts, particularly in high-risk seismic areas, mitigating catastrophic humanitarian and economic impact and protecting industrial facilities and transportation hubs.

DFOS systems have the potential to provide sensing-as-a-service, creating new business opportunities for network operators. Not only fiber infrastructure can be used for sensing, but also radio networks in 6G, where coordinated Fiber-Radio sensing systems further contribute to different sensing modality frameworks. This potential is further demonstrated in this thesis. The core idea is to transform national telecommunications infrastructure into a large-scale sensing grid, capable of monitoring external events beyond traditional communications. Such an approach allows a country/city to re-purpose deployed telecommunications assets for environmental surveillance, without the need for additional field sensors.

Building on the aforementioned, we carry this work from a computer-based simulation to laboratory-based methodologies then to an in-field testing and presents existing optical networks into a commercially viable sensing paradigm. This thesis explores the potential of exploiting the existing underground optical fiber terrestrial network as a whole sensing and localization grid for environmental surveillance and early warning systems. This work is focused on polarization-based sensing, exploited over the modulated traffic-carrying light traveling through optical fibers. Thanks to the modern optical transceivers that intrinsically requires polarization measurements to demodulate the optical data signals, and external sensing cards that are compatible with IM-DD networks without interfering with telecommunications services. In this work, we present original contributions in the field of Optical Networks, particularly conceptualization of Optical-Network-as-a-Sensor paradigm, development of polarization-based sensing mechanism, modeling of fiber external and internal birefringence, intelligent detection framework, and experimental and in-field testing showcasing multi-application sensing capabilities. This thesis is part of projects funded under the Italian National Recovery and Resilience Plan (PNRR), financed by the NextGenerationEU (NGEU) initiative. This work has received funding from the Italian Ministry of University and Research (MUR) under Decree DM 117/2023 and has been partially supported by the European Union - NextGenerationEU, Mission 4, Component 2, Investment 1.3, CUP E13C22001870001, partnership on “Telecommunications of the Future” (PE00000001 - program “RESTART” and by the project FAAS funded by OpenFiber.

Chapter 2

Optical Network as a Sensor

Today's optical networks are undergoing a major transformation, driven by Software-Defined Networking (SDN), telemetry, and Artificial Intelligence (AI). With an Intent-Based Networking (IBN) framework, SDN controllers and telemetry techniques can be integrated [16]. For instance, using intuitive language, the IBN framework allows users to define their desired operational goals, while letting the network operating system find the most efficient and optimal way to meet these goals [17]. This allows network administrators to manage and control complex optical infrastructures based on high-level operational intents. In modern optical network, AI is increasingly being explored to empower management and control, driving intelligent and data-driven operations. In particular, a range of Machine Learning (ML) use cases have been recognized, mainly including traffic forecasting, optimized resource allocation, amplifier control and Quality of Transmission (QOT) estimation and prediction [18]. Moreover, optical telecommunication has entered a new era of digital coherent transmission, especially following the significant increase in spectral efficiency of coherent optics [19]. Unlike Intensity Modulated - Direct Detected (IM-DD) systems, coherent optics can monitor, not only the intensity, but also the phase and polarization of the optical signal utilizing coherent transceivers. Nowadays, coherent transceivers have been widely deployed in long-haul optical networks and are increasingly adopted even for short-reach interconnects below 80 km [20]. Because polarization and phase are inherently sensitive to environmental changes, analyzing their temporal evolution provides a powerful mechanism to detect and identify external events. Beyond their role in telemetry, AI techniques can leverage these evolutions, and train ML models on their dynamics. Consequently, AI systems can translate raw physical-layer measurements into actionable situational awareness, enabling intelligent optical telecommunications network and environment-aware network management.

2.1 Software-Defined Networking & Telemetry

SDN architecture allows an agile, scalable and programmable optical infrastructure to enable centralized control over network resources utilizing SDN controllers. SDN architecture consists of data, control, and management planes. The Data plane includes data forwarding devices (eg; Routers, transponders, etc) and a southbound interface to enable communication between data and control planes. The control plane manages network traffic through a centralized software controller and a northbound interface to link the control plane to external applications and services (eg; AI engines, etc) by means of Application Programming Interface (API) as shown in Fig. 2.1.

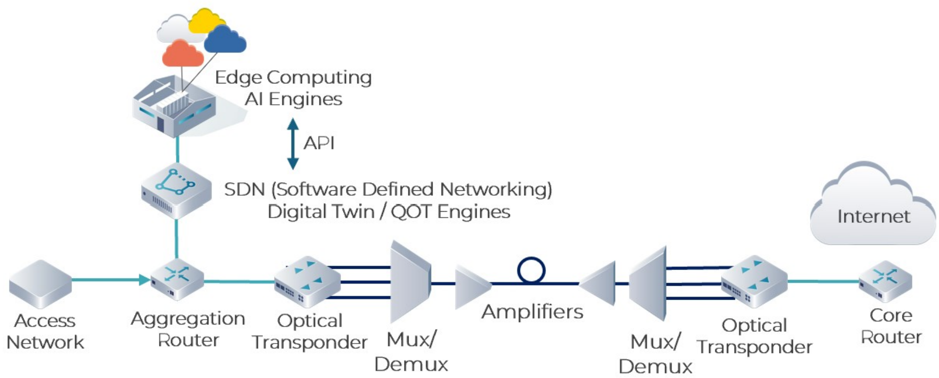

Fig. 2.1 SDN-enabled packet–optical network architecture.

The management plane aligns network behavior with business requirements and interface with underlying layers. SDN enables operators to manage and control optical networks by decoupling the control and data planes [21]. It further enhances the interoperability across heterogeneous optical systems. In traditional SDN architecture, the SDN controllers is also responsible for Routing and Spectrum Assignment (RSA). However, the recent trend, aimed to achieve more accurate QOT assessment, is to delegate RSA to specialized digital-twin computation engines or even QOT estimation modules, that can also provide the assignment of other parameters, such as the transmission power and the modulation format. This approach allows the effective evaluation of the physical impairments impact before activating a new lightpath. Telemetry on the other hand, has evolved into a key component for real-time network monitoring and for providing massive data for AI training by retrieving inline streams of time-series samples of packet-optical parameters enabling proactive management, automation, and the optimization of network performance and health. The integration of AI and edge computing has empowered network management and control, addressing the growing need for high-capacity and low-latency optical networks. These advancement have enabled wide range of applications in optical networks, including refined QOT modeling [22], amplifier control [23], failure and soft-failure identification [24], failure predication and localization [25, 26], alarm clustering [27], IBN [28], and sensing [29]. SDN controllers and telemetry techniques could be integrated within the IBN framework. This framework enables users to express desired operational goals using natural language, while allowing the network operating system automatically determines the optimal configuration, leveraging optimization processes to achieve low-latency routes, maximize bandwidth, or prioritize specific data flows [30]. As part of its assurance operations, if there is a fiber degradation or an optical link experiencing an increase in error rates or latency, the intent layer interprets network performance and re-route traffic or adjust signal parameters to maintain the QOT, significantly reducing setup time and human error. In fact, the IBN framework interprets the intents and translate them to actionable instructions for the SDN controller. The controller then program the underlying optical devices accordingly, adjusting wavelength and configuring modulations formats, and setting up the optical path. Consequently, enabling automation, scalability, and real-time adaptation.

2.1.1 Direct Detection and Coherent Optics

In IM-DD system, the optical transmitter only modulates the intensity of light, and the photodiode at the receiver directly converts power variation into electrical signal. The receiver sensitivity in conventional IM-DD scheme is neither dependent to the carrier phase nor to the polarization state of the incoming optical signal. In the contrary, when the incoming optical signal is interfered with a local oscillator, the receiver is said-to-be a coherent receiver. In the case of coherent receivers, we can retrieve all optical carrier related information, such as In-phase (I) and Quadrature (Q) components (amplitude and phase) as well as the signal State-of-polarization (SoP) [31]. It is important to note that, although conventional IM-DD systems do not inherently carry phase/polarization information, measurements can still be done using direct detection techniques when additional optical dedicated detectors are introduced. The most common optical modulation format for IM-DD systems is On-Off-Keying (OOK), where digital data is encoded by switching the optical power on and off to represent 1 and 0 states respectively. In coherent optical modulation, both I and Q components of the optical carrier can be independently modulated in each of the two orthogonal polarization states. For coherent optical detection, the received signal is mixed with a reference optical carrier generated by a local oscillator, enabling phase and amplitude sensitive detection and overcoming the limitation of IM-DD system's receiver [32]. Coherent systems support modulation formats with more bits per symbol, leading to a reduction in symbol rate and narrowed spectral width. Consequently, higher spectral efficiency per fiber capacities. Moreover, recovering the full multi-dimensional optical field provides additional benefits to compensate linear transmission impairments such as Chromatic Dispersion (CD) and Polarization Mode Dispersion (PMD). Thanks to the advancements in Digital Signal Processing (DSP)-based technologies. DSP techniques were also introduced to IM-DD systems, most notably with the first DSP-enabled 4-level Pulse Amplitude Modulation (PAM4) demonstrated in 2015 [33]. In today's infrastructure, long-haul and most metro networks rely on coherent systems, short-reach interconnects and access networks primarily rely on IM-DD. While SDN on top of an IM-DD system offers basic programmability and limited physical-layer visibility, SDN integrated with coherent optics enables AI-based intelligent telemetry, highly adaptive, and higher capacity optical networking.

2.1.2 Phase and State-of-Polarization

A coherent based transceiver can serve both as a communication endpoint and a high-resolution distributed sensor. The fundamental concept underlying coherent detection is to multiply the electric field of the modulated received signal with a continuous wave local oscillator [34]. For a given complex envelope, its associated band-pass real electric field can be written as:

$$E_s(t) = \Re\left\{\tilde{E}_s(t)e^{j\omega_s t}\right\} \tag{2.1}$$

In coherent detection, the meaningful information resides in the slowing varying complex baseband envelop embedded in $\tilde{E}_s(t)$ which is equal to $A_s(t)e^{j\phi_s(t)}$, particularly in its phase $\phi_s(t)$, since the fast carrier band-pass term $e^{j\omega_s t}$ is removed by coherent mixing and contain no usable information for DSP-based processing. Similarly, the local oscillator field can be represented by an equivalent complex envelop where $\tilde{E}_{LO}(t) = A_{LO}e^{j\phi_{LO}(t)}$, and:

$$E_{LO}(t) = \Re\left\{\tilde{E}_{LO}(t)e^{j\omega_{LO} t}\right\} \tag{2.2}$$

In an ideal coherent detection conditions, including perfect polarization alignment between the received signal and the local oscillator, and a self-homodyne configuration, the received signal and the local oscillator are combined with a 90° optical hybrid and detected with balanced photodiodes, we can detect the photocurrents to both I/Q components. The in-phase and quadrature branches become:

$$\begin{aligned} i_I(t) &\propto \Re\left\{\tilde{E}_s(t)\,\tilde{E}^*_{LO}(t)\right\}, \\ i_Q(t) &\propto \Im\left\{\tilde{E}_s(t)\,\tilde{E}^*_{LO}(t)\right\}. \end{aligned} \tag{2.3}$$

Therefore, the detected photocurrents can be written as:

$$\begin{aligned} i_I(t) &= KA_s(t)A_{LO}\cos(\phi_s(t) - \phi_{LO}(t)), \\ i_Q(t) &= KA_s(t)A_{LO}\sin(\phi_s(t) - \phi_{LO}(t)), \end{aligned} \tag{2.4}$$

Where K combine the photodiode reponsivity and hybrid coupling factors. Consequently, the I/Q components can be written as:

$$\begin{aligned} I(t) &\equiv A_s(t)\cos\theta(t), \\ Q(t) &\equiv A_s(t)\sin\theta(t), \end{aligned} \tag{2.5}$$

with

$$\theta(t) = \phi_s(t) - \phi_{LO}(t). \tag{2.6}$$

The complex baseband signal recovered by the coherent transceiver holding the amplitude and phase information is:

$$\tilde{E}_{\mathrm{rx}}(t) = I(t) + jQ(t) = A(t)e^{j\phi(t)} \tag{2.7}$$

This is the so-called phase diversity in homodyne coherent receivers. The polarization of light stands as one of the most remarkable phenomena in nature, having led to numerous scientific discoveries and technological applications. Today it continues to play a vital role in modern optical communication networks.Coherent detection can also perform polarization diversity, where the receiver captures both components of the optical field vector after a polarization beam splitter. The receiver splits the incoming signal into x and y polarization, perform I/Q mixing on each, and therefore obtain:

$$\begin{aligned} \tilde{E}_x(t) &= I_x(t) + jQ_x(t), \\ \tilde{E}_y(t) &= I_y(t) + jQ_y(t) \end{aligned} \tag{2.8}$$

In 1852, George Stokes introduced four parameters, now known as the Stokes parameters (S_0, S_1, S_2, S_3), to represent the polarization state of light. The optical field is generally elliptically polarized, however, several combinations of amplitude and phase have degenerate polarization states, such as Linearly Horizontal/Vertical Polarized Light (LHP/LVP), Linear ±45° Polarized light (L±45°P), and Right-Left Circularly Polarized light (RCP/LCP). Elliptically polarized light can be represented by its stokes parameters arranged as a column matrix, or equivalently, as a stokes vector. SoP stokes parameter can be then derived as follows [35]:

$$\begin{aligned} S_0 &= |\tilde{E}_x(t)|^2 + |\tilde{E}_y(t)|^2 = A_x^2(t) + A_y^2(t), \\ S_1 &= |\tilde{E}_x(t)|^2 - |\tilde{E}_y(t)|^2 = A_x^2(t) - A_y^2(t), \\ S_2 &= 2\Re\Big\{\tilde{E}_x(t)\tilde{E}_y^*(t)\Big\} = 2A_x(t)A_y(t)\cos\delta(t), \\ S_3 &= 2\Im\Big\{\tilde{E}_x(t)\tilde{E}_y^*(t)\Big\} = 2A_x(t)A_y(t)\sin\delta(t), \end{aligned} \tag{2.9}$$

Where the relative phase $\delta(t) = \phi_y(t) - \phi_x(t)$. Assuming light propagates along Z axis, linearly polarized light is caused by in-phase oscillations in the X-Y plane. In the contrary, left and right elliptical/circular polarization can be created if a phase shift is introduced between the horizontal and vertical components. Thus, the polarization of light can be defined by the direction of its three-dimensional electric field vector. The quantities $A_x(t)$ and $A_y(t)$ are the amplitudes of the orthogonal components of the electric field. This formulation considers the total intensity of the optical beam S_0, the preponderance of LHP light over LVP light S_1, the preponderance of L+45°P light over L−45°P light S_2, the preponderance of RCP light over LCP light S_3, and the degree of polarization P is given by [36]:

$$P = \frac{\sqrt{S_1^2 + S_2^2 + S_3^2}}{S_0}, \quad \text{such that } 0 \leq P \leq 1. \tag{2.10}$$

In practical scenarios involving modulated signals, noise, and finite measurement bandwidth, the measured degree of polarization may deviate from unity and depends on the temporal and spectral resolution of the stokes parameter estimation. However, in ideal continuous-wave optical signal, the degree of polarization is ≈ 1. For sensing SoP perturbation, the total intensity of the optical beam is not crucial, thus, we can normalize the stokes vector by dividing each component by S_0. The polarization evolution and the differential phase of the optical field are directly influenced by environmental perturbations such as vibration, temperature gradients, strain, and acoustic pressure. When integrated with SDN and streamed through real-time telemetry, these low-level physical indicators can provide multi-dimensional observable space. By further embedding edge computing and AI driven models, the optical infrastructure evolves from a passive transport medium into a geographically distributed sensing fabric. In this approach, coherent receivers serve as wide distributed array of sensors, while the AI models implemented in the control plane or at the edge leverage multi-dimensional telemetry streams, enabling sensing network functionalities, capable of detecting, classifying, and localizing environmental events. Consequently, opening a pathway toward intelligent, environment-aware, and autonomously managed optical infrastructure. The same concept can be applied to IM-DD systems, however, IM-DD systems requires additional instrumentation to indirectly monitor phase or polarization information.

2.2 Distributed Fiber Optic Sensing

DFOS exploits the evolutionary change of phase, polarization, or backscattered intensity, depending on the sensing technique, which can be detected by DSP-based coherent transceivers or monitored by external sensing devices in IM-DD systems. Driven by this progress, DFOS technologies involves distributed acoustic DAS, temperature DTS, strain DSS, and vibration DVS sensing. Around mid-2010, the telecommunications sector began exploring how DFOS could be leveraged to enable novel applications using the existing fiber footprint, even though the technology had already been used for decades in non-telecommunications domains, typically on a limited scale, for highly specific applications, and at very high cost. DFOS systems can be integrated to enable smart cities' applications such as: civil-structure health assessment [37], pipeline surveillance [38], campus perimeter security[39], underwater applications[40], and seismic activities [41], etc. Although, substantial research efforts and feasible use cases of DFOS have been presented, the broader industry eco-system is not yet matured for mass commercial deployments. The successful field trials and technology innovations should ultimately paves the way to market-ready solutions. To reach this, a healthy eco-system must be built through the developments of standards. Approved in October 2025, and responding to the lack of DFOS standards for telecommunications applications, the International Telecommunication Union Telecommunication (ITU-T) Study Group 15 plenary meeting held in Geneva, Switzerland, in December 2023, initiated the first DFOS standardization project.[42]. This work specifies DFOS optical interfaces requirements for terrestrial optical network deployments. For non-telecommunications applications, standards is developed by Fiber Optic Monitoring in Subsea Applications (SEAFOM), International Electrotechnical Commission (IEC), and IEEE Standards Association, to ensure product compatibility and interoperability for wide market solutions [43]. DFOS technologies are generally classified into two categories: back-scattering based systems that uses a dedicated DFOS system and feed-forward-based systems that has a sensing function in DSP-based receivers, both can be employed in IM-DD and coherent systems.

2.2.1 Backscattered Type Sensing

Backscattering approaches typically leverage raman, brillouin, or rayleigh signals. Rayleigh backscattering is utilized for DAS and DVS, brillouin backscattering for DSS and DTS, whereas raman for temperature sensing DTS. These sensing techniques employ optoelectronic interrogator units that lunch short light pulses into a fiber cable and then analyze distortions in the light that scatters back and compare it with the incident one, allowing the retrieval of strain-rate information proportional to the amount of physical stress impacting the fiber at a specific location. DFOS backscattered systems, theoretically speaking, can operate outside (out-band) or within (in-band) DWDM channel as shown in Fig. 2.2.

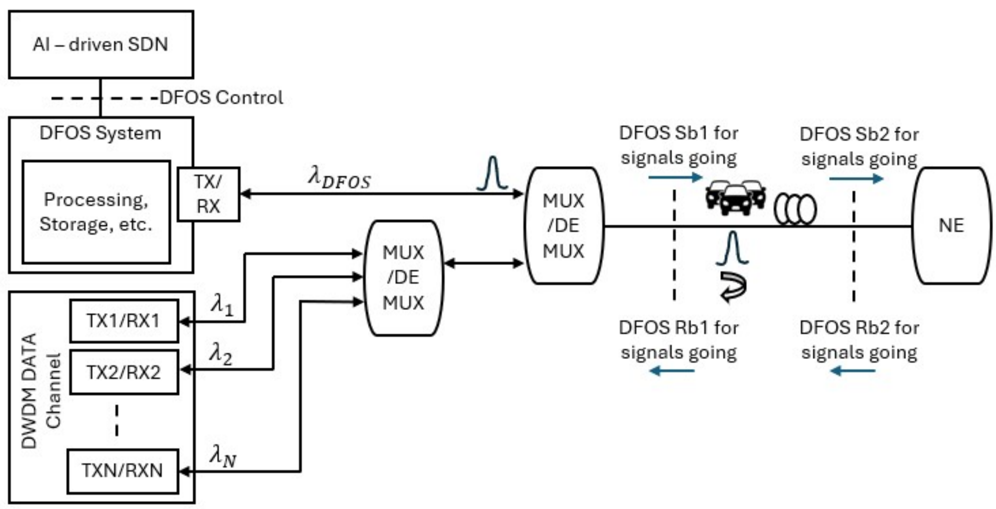

Fig. 2.2 Out-Band System Architecture for Backscattered Sensing

In-band sensing do not require additional Multiplexer/Demultiplexer (MUX/ DEMUX) as the sensing signal coexists with data traffic on the same wavelength band. In contrast, out-band sensing operates over two distinct wavelength ranges, which are specified by the ITU-T G.dfos recommendation: 1511-1517 nm, which is compatible with optical supervisory channel, and wavelengths above 1635 nm. The DFOS signal typically operates at a repetition rate of 2Khz, supporting a maximum fiber reach up to 50 km, while preventing interferences between successive and backscattered signals. Interference is defined relative to the increase of the DWDM optical Signal-to-Noise Ratio (OSNR) in the presence of a DFOS signal. The ITU-T is still discussing OSNR issue and the DWDM channel sensitivity at the optical interfaces (Sb1, Sb2, Rb1, and Rb2), between optical MUX/DEMUX and Network Elements (NE), in the presence of a DFOS probe. A DFOS probe can either co-propagate with DWDM traffic in a bidirectional single-fiber span or counter-propagate in a dual-fiber unidirectional transmission system. The six tier-1 network operators (Verizon, NTT, AT&T, British Telecom, China Telecom, and Orange), conducted experimental tests and numerical simulation to understand the level of interference [43]. For the in-band approach, the results showed negligible Cross-Phase Modulation (XPM) and phase slip in counter-propagating scenario. This is because the interaction time between DFOS and DWDM is short. In the contrary, in-band co-propagating scenario showed strong impact on the DWDM signal's OSNR due to XPM. However, these coexistence limitations are mainly associated with conventional pulsed probing schemes. Recent work by J. Wang has shown that alternative interrogation approaches, such as pulse-compression techniques and optimized probing formats, can significantly improve compatibility with in-band DWDM systems [44]. Further investigations is carried out for the out-band scenarios. Despite having higher spatial resolution and sensitivity comparing to feed-forward method, Backscattered DFOS systems are incompatible with inline optical amplifiers that are commonly found every 80 kilometers in live traffic-carrying optical networks, and this is because the optical isolator inside each amplifier block the backscattered signal, limiting the application sensing range. Although the optical amplifiers could be intentionally removed along dedicated dark fibers, which would lead to rampant signal attenuation, necessitating multiple DFOS devices to cover sufficiently large sensing area. In metro networks, the ITU-T G.dfos recommendation scope is intended to involve both, the backscattered and feed-forward sensing systems, however, in its first version only the backscattered type will be included. Backscattered DFOS systems can also operates over Passive Optical Networks (PONs), which remain the prevalent technology for access networks. In a typical PON architecture, the optical infrastructure follows a point-to-multipoint tree topology consisting of an Optical Line Terminal (OLT), an Optical Distribution Network (ODN), and multiple Optical Network Units (ONU)s located at the subscribers' locations. Optical splitters within an ODN typically use splitting ratios ranging from 1:16 to 1:128. These splitters impose two major challenges for backscattered DFOS systems. First, the DFOS signal have to pass the power splitter twice, resulting in very high insertion loss. A double-pass loss is over 36 dB for a 1:64 splitting ratio, thus an extremely sensing DFOS receiver is needed. Second, it becomes challenging to determine on which distribution fiber the disturbance has happened without additional mechanisms. Although, on-going research explores new built-in splitters with fiber-bragg grating or other mechanisms to differentiate splitter ports, however, it is not practical to replace the splitters already deployed in PON. Recent research efforts have proposed advanced signal processing and ML techniques to solve branch ambiguity [45].

2.2.2 Feed-Forward Type Sensing

Feed-forward methods usually leverage the variations in the polarization state/phase embedded within data signals.

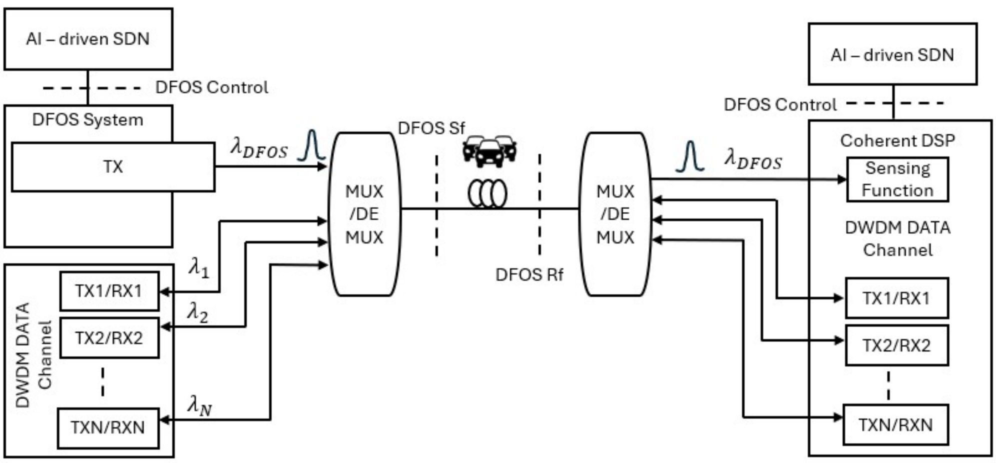

Fig. 2.3 In-Band System Architecture for Feed-Forward Sensing

Unlike backscattered systems, feed-forward methods are compatible with in-service networks without requiring additional equipment to be integrated in the network as demonstrated in Fig. 2.3, enabling sensing over wide geographical area and, importantly, at a significant lower cost compared to backscattering-based techniques. Thanks to the coherent technologies that can pick-up related information. Most recently, in March 2025, the ITU-T initiated a technical report TR.fsc for further investigation, aims to consolidate in feed-forward systems and asses their maturity in terms of spatial resolution and DFOS sensitivity in order to determine the path for future standardization. DFOS-Sf and DFOS-Rf are reference points for several key optical parameters to be discussed. Despite the ongoing experimental tests and research efforts to enhance spatial resolution in feed-forward systems, the coordinated operation between Integrated Sensing and Communication (ISAAC) and DFOS systems could also make significant contribution to this objective. ISAAC has been recognized in the mobile network industry to sense surrounding environments. The International Telecommunication Union's Radiocommunication Sector (ITU-R) is leading the guiding vision for the past and future generation of International Mobile Telecommunications (IMT). In the IMT-2030 vision report, approved in November 2023, the ITU-R outline the 6G network framework, highlighting ISAAC as a key feature capable of sensing and characterizing remote objects or environmental conditions [46]. The next phase of IMT-2030 vision report, until 2027, will focus on the evaluation criteria for potential radio interfaces. An ISAAC-DFOS system can greatly enhance the Operations, Administration, and Maintenance (OAM) of mobile network operators. For spatial resolution enhancement, as demonstrated in Fig. 2.4, an ISAAC radio unit performs sensing to identify objects and its proximity to the deployed fiber. A DFOS system first process the received data to determine the risk level of any external event impacting the cable, where AI models are leveraged. In case of an event, the DFOS communicates with an orchestrator. The orchestrator will then coordinates between the management system and multiple wireless cores to facilitate communication. The radio unit performs sensing and notify field engineers to prevent harmful event, or inform the management system through the wireless core and the orchestrator to perform further sensing activities.

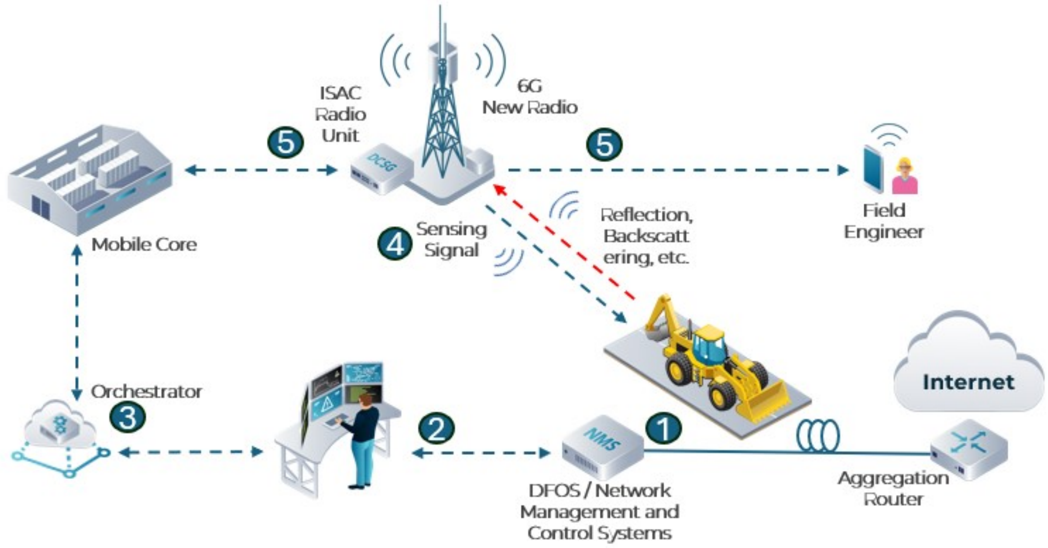

Fig. 2.4 Conceptual Diagram of ISAAC-DFOS Sensing System

As in metro networks, the feed-forward sensing systems are compatible with PON systems, particularly with 50G-PON, as it represents the first PON architecture that adopt DSP technology. The opportunity arises then to embed the sensing function in the DSP-based receiver [47]. However, the current IM-DD-based PON systems don't have the ability to track SoP of light evolution. In [48], Veen et al. proposed a low complexity polarization-based sensing and ODN monitoring in IM-DD-based PON. Building on this, the author introduces a Polarization Sensing Element (PSE) that enable polarization tracking without requiring DSP-based coherent receivers. The PSE consists of a low-loss tap (<0.5 dB) followed by a Polarization Beam Splitter (PBS) to extract the two orthogonal polarization components. To extract the variation in SoP stokes parameters, these orthogonal components can be monitored by a low-bandwidth detector, enabling the conversion of conventional IM-DD ONU receivers into polarization-aware devices capable of detecting environmental perturbations. Feed-forward based sensing systems are highly desirable in the long run, particularly in areas lacking dark fibers, and in PONs after realizing their big factor in expanding network capabilities to new sensing and monitoring application for tomorrow's smart cities concept.

2.2.3 Backward Type Polarization Sensing

Recent demonstration of optical fiber sensing can be classified as either phase-based or Feed-Forward based sensing and localization. DAS [49], Interferometric Techniques [50, 51], Brillouin Optical-Time Domain Analysis (BOTDA) [52] and Raman Optical-Time Domain Reflectometry (ROTDR) [53] are considered among the Phase-based sensing modalities. By leveraging Brillouin light scattering, BOTDA enables linear measurement of strain and temperature impacting the fiber, whereas ROTDR is primarily used for temperature monitoring. However, both techniques are limited by their sensing range, low temporal resolution, and high system complexity, making them unsuitable for large-scale sensing. On the other hand [50], Wang et al. proposed a laser interferometry-based sensing technique to monitor the traffic flow of both heavy and light vehicles. In contrast, the microwave-frequency interferometric approach, proposed in [51], measures the phase of a microwave-modulated optical carrier, relaxing the need for an ultra-stable, low-phase-noise laser, though it still requires high hardware cost and complexity for optical mixing and modulation, specially across wide coverage areas. Coherent Rayleigh back-scatter-based DAS senses both the phase and amplitude. DAS has proven its robustness in pipeline surveillance and leakage localization[38], perimeter protection[39], and seismic monitoring in terrestrial areas [41], its use in submarine environment has also proven reliable for sensing whales, storms, ships, earthquakes [40], ocean currents [54], and volcanic events [55]. The successful development of phase-based sensing for localization applications, together with its accurate spatial resolution, makes it an attractive approach despite its higher implementation cost, system complexity and limited sensing range. Recent research efforts have introduced additional sensing dimension based on the analysis of backscattered SoP to enable localization of external events. In this part, we present the theoretical derivations on how external events can be localized by analyzing the backscattered polarization state evolution [56]. By considering a fiber cable under static conditions, with length L_s, the cable can be segmented into N successive small fiber sections, each contributing to the localization system in correspondence to its spatial resolution. The shorter the segment, the higher the spatial resolution, enabling more precise localization. Let a perturbation occur at the m-th section of the cable. The back-scattered signal is the summation of the back-scattered light contributions all along the sensing fiber as demonstrated in Fig. 2.5.

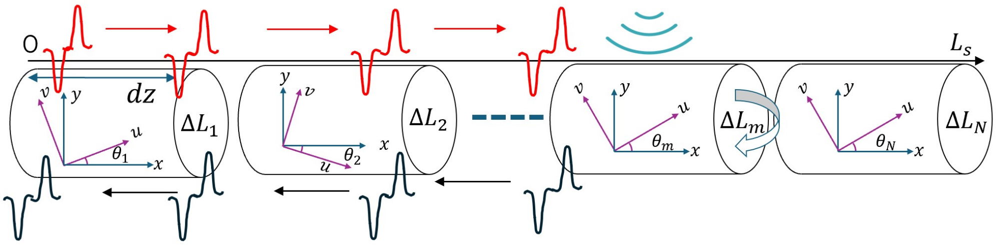

Fig. 2.5 Back-Scattered Polarization-Based Approach

Each segment is associated by a 2 × 2 Jones Matrix, denoted by H, to cover the polarization state dimension. The light propagation in an optical fiber is reciprocal, meaning that $\mathbf{U}_{\text{backward}} = \mathbf{U}^T_{\text{forward}}$. As in Fig. 2.6, we assume $\mathbf{U}_{\text{m}}$ to be the forward matrix, while considering perfect mirror reflection along the cable.

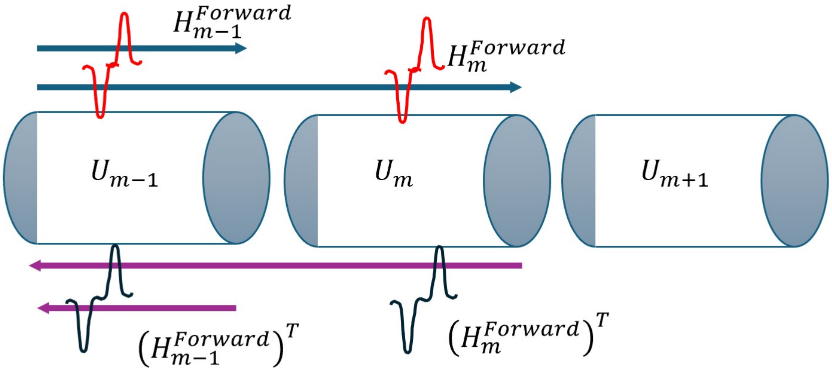

Fig. 2.6 Back-Scattered Polarization-Based Approach- Zoomed to segment m

The polarization matrix H can then be represented by:

$$\mathbf{H}_{\text{m}} = (\mathbf{H}^F_{\text{m}})^T \mathbf{H}^F_{\text{m}} \tag{2.11}$$

Where,

$$\mathbf{H}^F_{\text{m}} = \mathbf{U}_{\text{m}} \mathbf{H}^F_{\text{m-1}} \tag{2.12}$$

and,

$$\mathbf{H}_{\text{m-1}} = (\mathbf{H}^F_{\text{m-1}})^T \mathbf{H}^F_{\text{m-1}} \tag{2.13}$$

Therefore, the H matrix can be then derived to be:

$$\mathbf{H}_{\text{m}} = (\mathbf{U}_{\text{m}} \mathbf{H}^F_{\text{m-1}})^T (\mathbf{U}_{\text{m}} \mathbf{H}^F_{\text{m-1}}) \tag{2.14}$$

$$\mathbf{H}_{\text{m}} = (\mathbf{H}^F_{\text{m-1}})^T \mathbf{U}^T_{\text{m}} \mathbf{U}_{\text{m}} \mathbf{H}^F_{\text{m-1}} \tag{2.15}$$

Here the identity $(\mathbf{AB})^T = \mathbf{B}^T \mathbf{A}^T$ has been used. H is an orthogonal matrix that describes the cumulative birefringence effects of the complete round trip to and from the m-th section. The local birefringence matrix is not possible to calculate, however, it is still possible to retrieve perturbation information by performing the following derivation[56]:

$$\mathbf{H}^{-1}_{\text{m-1}} \mathbf{H}_{\text{m}} = [(\mathbf{H}^F_{\text{m-1}})^T (\mathbf{H}^F_{\text{m-1}})]^{-1} [(\mathbf{H}^F_{\text{m-1}})^T \mathbf{U}^T_{\text{m}} \mathbf{U}_{\text{m}} \mathbf{H}^F_{\text{m-1}}] \tag{2.16}$$

$$\mathbf{H}^{-1}_{\text{m-1}} \mathbf{H}_{\text{m}} = (\mathbf{H}^F_{\text{m-1}})^{-1} (\mathbf{H}^{FT}_{\text{m-1}})^{-1} [(\mathbf{H}^F_{\text{m-1}})^T \mathbf{U}^T_{\text{m}} \mathbf{U}_{\text{m}} \mathbf{H}^F_{\text{m-1}}] \tag{2.17}$$

Here the identity $(\mathbf{AB})^{-1} = \mathbf{B}^{-1} \mathbf{A}^{-1}$ has been used. Since all these matrices are unitary matrices, their product will be:

$$\mathbf{H}^{-1}_{\text{m-1}} \mathbf{H}_{\text{m}} = (\mathbf{H}^F_{\text{m-1}})^{-1} \mathbf{U}^T_{\text{m}} \mathbf{U}_{\text{m}} (\mathbf{H}^F_{\text{m-1}}) \tag{2.18}$$

Since, $(\mathbf{H}^{FT}_{\text{m-1}})^{-1} (\mathbf{H}^F_{\text{m-1}})^T = I$; Identity Matrix. Eq. (2.17) is in the form of $\mathbf{B} = \mathbf{A}^{-1} \mathbf{V} \mathbf{A}$. Therefore, $\mathbf{B}$ and $\mathbf{V}$ have the same eigenvalues. Plotting the eigenvalue of $\mathbf{U}^T_{\text{m}} \mathbf{U}_{\text{m}}$ over space allow the precise localization on the m-th section by observing the eigenvalue peak. Details upon which model the fiber is segmented into small sections will be presented in the following chapter.

2.3 Artificial Intelligence in Optical Networks

AI covers a wide field of techniques ranging from search and optimization methods to ML and statistical modeling. In particular, ML is a valuable tool when it comes to modeling a complex phenomenon. In optical networking, ML is increasingly integrated into the network control and management, enabling models to learn relations among training data, including QOT estimation or prediction, amplifier control, traffic prediction and resource allocation (routing and spectrum assignment). The so-called deep learning arises when ML algorithms become deep and complex [57]. Deep learning, a data-driven methodology, allows a computational model composed of multiple processing layers to learn patterns and extract meaningful abstractions from given data [58]. Since the 1980s, Deep learning has been known by the so-called Artificial Neural Networks (ANNs), which were designed to mimic how learning happens in the human brain. The success of ANN design was largely driven by a simple feed-forward neural network model called Multi-Layer Perceptron (MLP), which consists of multiple fully connected layers. A fully connected MLP with L layers includes an input layer, an output layer, and $L-2$ hidden layers. Each neuron in a given layer is connected to all neurons in the subsequent layer, without inter-layer connections between neurons in the same layer. The input data is processed layer by layer, using neurons' weights and biases through linear transformation and non-linear activation functions such as sigmoid, hyperbolic tangents or rectified linear units. By computing the gradients of a cost function that measures the difference between the network output and the desirable target, the MLP adjusts its learnable parameters to minimize error value. However, to efficiently minimize this error, a back-propagation computation was proposed by David Rumelhart, Geoffrey Hinton, and Ronald Williams in their landmark 1986 paper [59]. The back-propagating algorithm determine how much each learning parameter contributed to the overall error. Over the past decade, it has become feasible to design and train much deeper neural networks capable of recognizing complex patterns, such as Convolutional Neural Network (CNN), Recurrent Neural Network (RNN) and Generative Adversarial Network (GAN) or Variational Autoencoder (VAE). RNNs are particularly attractive for modeling time series data due to their capability to capture temporal dependencies from sequential data such as time-series of QOT metrics, phase evolution, and SoP trajectories [60]. However, their effectiveness for learning long-term patterns is often hindered by the vanishing gradient problem, which limits their ability to capture long-range correlations that are crucial in fiber-based sensing and network monitoring scenarios. To address this limitation, Long Short - Term Memory (LSTM) networks were developed, incorporating a memory cell and gating mechanism that mitigate the vanishing gradient issue [61]. The LSTM unit relies on three gates: the input gate, output gate, and forget gate, enabling the control of information flow [62]. Specifically, the input and output gates manage the activation signals entering and leaving the cell, while the forget gate resets the cell memory when certain information is no longer needed. Let $\mathbf{x}_t$ represent the input time-series data at time t. The values of the input gate (i_t), output gate (o_t), and forget gate (f_t) are computed as follows:

$$\begin{aligned} i_t &= \sigma(W_i[\mathbf{h}_{t-1}, \mathbf{x}_t] + b_i), \\ o_t &= \sigma(W_o[\mathbf{h}_{t-1}, \mathbf{x}_t] + b_o), \\ f_t &= \sigma(W_f[\mathbf{h}_{t-1}, \mathbf{x}_t] + b_f), \end{aligned} \tag{2.19}$$

where W_i, W_o, and W_f are the weight matrices for the input, output, and forget gates, respectively, and b_i, b_o, and b_f are their respective bias terms. Here, $\mathbf{h}_{t-1}$ denotes the hidden state from the previous time step, and $\sigma(\cdot)$ is the sigmoid activation function. The hidden state $\mathbf{h}_t$ and cell state $\mathbf{c}_t$ at time t are then updated as:

$$\mathbf{c}_t = i_t \odot \tilde{\mathbf{c}}_t + f_t \odot \mathbf{c}_{t-1} \tag{2.20}$$

$$\mathbf{h}_t = o_t \odot \tanh(\mathbf{c}_t) \tag{2.21}$$

where $\odot$ denotes the element-wise (Hadamard) product, and $\tanh(\cdot)$ is the hyperbolic tangent function. The candidate cell state $\tilde{\mathbf{c}}_t$ is given by:

$$\tilde{\mathbf{c}}_t = \tanh(W_c[\mathbf{h}_{t-1}, \mathbf{x}_t] + b_c)\,, \tag{2.22}$$

with W_c and b_c being the weight matrix and bias for the cell state update. Given the inherently time-varying nature of the telemetry and sensing signals considered in this work, LSTM emerges as the most suitable neural network architecture for this thesis, and will therefore be adopted as the primary neural network model for learning and exploiting the spatio-temporal behavior of optical networks used as sensors. In this thesis, Gated Recurrent Neural Network (GRU) is introduced as a simplified alternative to the LSTM network [63], aimed at reducing the architectural complexity and minimizing the number of parameters involved. Unlike LSTM, the GRU uses only two gates: the update gate and the reset gate. The update gate combines the roles of the input and forget gates found in LSTM, allowing control over how much of the previous memory should be retained in the new state. Meanwhile, the reset gate functions similarly to LSTM's forget gate, determining which parts of past information can be discarded when they are no longer needed. The update gate u_t and the reset gate r_t in the GRU are defined as follows:

$$u_t = \sigma(W_u[\mathbf{h}_{t-1}, \mathbf{x}_t] + b_u) \tag{2.23}$$

$$r_t = \sigma(W_r[\mathbf{h}_{t-1}, \mathbf{x}_t] + b_r) \tag{2.24}$$

Here, W_u and W_r represent the weight parameters for the update and reset gates, respectively. The parameters b_u and b_r denote the corresponding bias terms. The term $\mathbf{h}_t$ refers to the hidden state vector or output state vector. At time step t, the hidden state $\mathbf{h}_t$ is expressed as follows:

$$\mathbf{h}_t = u_t \odot \tilde{\mathbf{h}}_t + (1 - u_t) \odot \mathbf{h}_{t-1} \tag{2.25}$$

where the candidate hidden state $\tilde{\mathbf{h}}_t$ is given by:

$$\tilde{\mathbf{h}}_t = \tanh(W_h[\mathbf{h}_{t-1}, \mathbf{x}_t] + b_h) \tag{2.26}$$

In these equations, W_h and b_h represent the weight and bias parameters, respectively. In this thesis, the choice of ML architectures is guided by their suitability for capturing dependencies in sequential signals.

Chapter 3

Environmental Surveillance

In an ideal optical fiber, which is typically circular in shape, the silica glass of which it is made is isotropic. Under the weakly guiding approximation, such an optical fiber supports the propagation of a fundamental mode with two degenerate and orthogonal polarization states. Accordingly, the theoretical polarization properties of an optical pulse can be represented by a superposition of these two states. In reality, optical fibers are often birefringent due to construction imperfections that disrupt the fiber's cylindrical symmetry, consequently, lifting the polarization degeneracy. However, considering a sufficiently short fiber segment, the perturbation or the internal birefringence stemming from construction imperfections can be assumed spatially uniform, allowing the local birefringence to be treated as a constant [64]. Seismic waves are another form of external perturbation that induce strain and stress related birefringence in optical fibers, thereby altering the light's SoP. To isolate and characterize the impact of such external disturbances on the fiber's polarization response, it is crucial to first account for the contribution of internal behavior. To this end, the Waveplate model is adopted, in which the fiber cable is simulated as a concatenation of numerous small segments referred to as "plates" to ensure a uniform internal perturbed medium across each section [65]. Hence, the effect on light's polarization is well defined and can be quantitatively described by 2π divided by the polarization beat length L_B, which is the amount of internal birefringence defined as the propagation length over which the optical path length of the two polarization eigenmodes differs by exactly one wavelength. Consequently, any deviations from this established internal behavior can be attributed to external events, as they would introduce unexpected changes in the SoP of light. Without considering any external effect, when linearly polarized light is injected at 45-degrees angle with respect to the linear polarization eigenmodes, the light acquires after one quarter of L_B a phase shift of $\frac{\pi}{2}$ transforming the linear input polarization into a circular one, and after one half of L_B a phase shift of π.

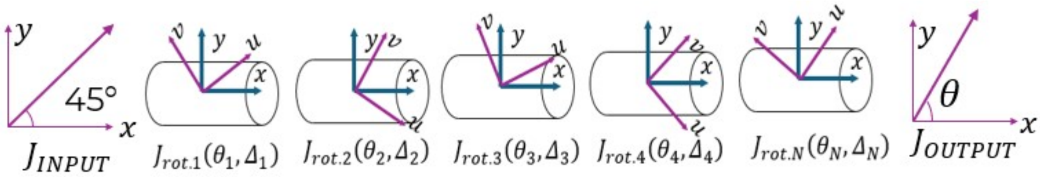

Fig. 3.1 Schematic Representation of Fiber Sections

Earthquake-induced strain is incorporated as phase shifts between the orthogonal polarization components as shown in Fig. 3.1, where Δ_k represents the phase retardation induced in the k-th fiber segment, and the output SoP jones vector is characterized by:

$$J_{\text{out}} = \prod_{k=1}^{N} J_k(\theta_k, \Delta_k)\, J_{\text{in}}. \tag{3.1}$$

In a more detailed approach, these plates by nature have random orientations, which can not be controlled, adding complexity to the analysis of external effects. Basically, each plate is assigned with two random angles, Ellipse of polarization, defined in the interval $[-\pi/2, \pi/2]$, or the major axis angle, and the Eccentricity of the ellipse, defined in the interval $[-\pi/4, \pi/4]$. For simplicity purposes, in our model we consider only the major axis angle θ. In a frequency interval in which the first order approximation for the state of polarization is valid, any fiber section or Waveplate is characterized by Jones Matrix $M(\omega)$:

$$M(\omega) = e^{j\beta(\omega)}U(\omega) = e^{j\beta(\omega)} \begin{pmatrix} u_1 & u_2 \\ -u_2^* & u_1^* \end{pmatrix} = e^{j\beta(\omega)} R_{\text{out}}^{-1} M_d R_{\text{in}} \tag{3.2}$$

where $\beta(\omega)$ represents a global phase term not essential for SoP calculation and u_1 and u_2 are complex coefficients defining the unitary transformation of the Jones matrix.

$$M_d = \mathrm{DIAG}\left(e^{j\omega\Delta\tau/2}, e^{-j\omega\Delta\tau/2}\right) \tag{3.3}$$

ω represents the difference between the generic frequency of the optical signal and the central frequency ω_0, and $\Delta\tau$ is the Differential Group Delay (DGD) of the fiber and could be described as the contribution of uniform internal birefringent medium summed with the external effect.

$$\Delta\tau = 2\pi\frac{dz}{L_b}\left(1 + \frac{\Delta L_i}{dz}\right) \tag{3.4}$$

d_{z} is considered as the spatial resolution or the fiber section length, L_{B} is the beat length, and $\Delta L_i/dz$ is the elongation (expansion or compression) of the fiber section induced by external stress. R_{in} and R_{out} are:

$$R_{\mathrm{in}} = \begin{pmatrix} \cos\theta & -\sin\theta \\ \sin\theta & \cos\theta \end{pmatrix} \tag{3.5}$$

$$R_{\mathrm{out}} = \begin{pmatrix} \cos\theta & -\sin\theta \\ \sin\theta & \cos\theta \end{pmatrix} \tag{3.6}$$

The matrix $U(\omega)$ of the cascade of two waveplates, described by U_1 and U_2, is

$$U = (U_2, U_1) = (R^{-1}_{\mathrm{out2}}(M_{d2})(R_{\mathrm{in2}}))(R^{-1}_{\mathrm{out1}}(M_{d1})(R_{\mathrm{in1}})). \tag{3.7}$$

The more segmented the fiber into waveplates the better, to ensure small sections and consider uniform internal birefringence at each section. Consequently, the polarization at the output of the fiber, equivalent to Eq. 3.1, is calculated as:

$$J_{\mathrm{out}} = U \times J_{\mathrm{in}} \tag{3.8}$$

The proposed model is sufficient to describe the polarization evolution induced by external perturbation as this perturbation affect the local fiber birefringence, leading to variations in the phase difference between orthogonal polarization components. Despite the random orientations in θ of each plate, causing varying polarization evolution, the data should always contain invariant information linked to a specific external event, even it can differentiate between earthquakes with different magnitude or seismic characteristics. This is valid when the external effect induces a sufficiently strong and structured response compared to the variability introduced by random birefringence. Consequently, this invariant parameter enables the capability of this model to distinguish between several events and at the same time. By leveraging ML techniques and Monte Carlo analysis over different random birefringence orientations realizations for a specific event, the AI model is trained and learned on this pattern of polarization change to detect and characterize the event, where in this work it is the Primary earthquake waves arrival. This is where the ML model becomes valuable. Instead of analyzing the changes in the three stokes presented for each SoP evolution (S_1, S_2, S_3) and to reduce computational time, we propose to calculate for each SOP evolution from their stokes representations, the State of Polarization Angular Speed (SOPAS) [66], thus, analyzing one variable per file instead of three. The discrete SOPAS, denoted by $\Omega[k]$, and the sampling period T_s, are given by the following relationship:

$$\Omega[k] = \left| \arccos\left(\frac{\mathbf{S}_k \cdot \mathbf{S}_{k-1}}{\|\mathbf{S}_k\| \, \|\mathbf{S}_{k-1}\|} \right) \right| \frac{1}{T_s} \tag{3.9}$$

where $(\mathbf{S}_k, \mathbf{S}_{k-1})$ is the dot product between the Stokes vectors at time k and at time $k-1$.

3.1 DAS-based Earthquake Stokes Simulator

There's a lot of interest in using fiber sensing for early disaster warning as in the case of earthquakes. DAS systems are very accurate as distributed seismic sensor, but costly and with a limited range. A DAS system is capable to measure the small fiber elongation due to a seismic wave crossing the DAS fiber. Fig. 3.2 demonstrates 4 seconds of DAS data-induced by an earthquake recorded in Iceland in 2015 [67]. This data is coupled along a 10 km of fiber cable at 200 Hz sampling frequency, each vertical trace represents the fiber elongation during the considered timespan at a fixed fiber point while the horizontal trace is associated to space sampling or fiber segments, thereby calculating the aforementioned $\Delta L_i/dz$. Traces are acquired every 4 meters with a 10 km fiber length, resulting in 2500 sections. Typically, the earthquake Surface wave is anticipated by a weaker P-wave as depicted in Fig. 3.2. The time between the surface wave and the P-wave depends on the proximity to the earthquake epicenter, thereby varying from 1 or 2 seconds to tens of seconds time difference. Hence, a reliable earthquake sensing implementation in data networks would greatly expand the capability to raise timely warning signals, however, earthquake countermeasures will rely heavily on the urban distance to the center. The more time between the latter two waves the more earthquake countermeasure urban can initiate.

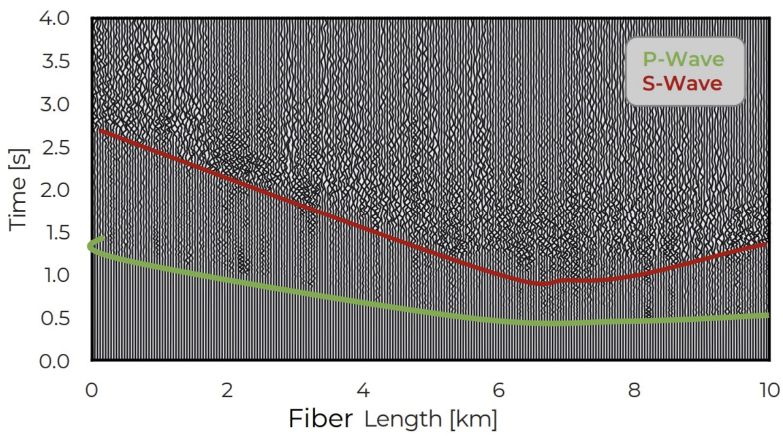

Fig. 3.2 DAS measured earthquake seismogram.

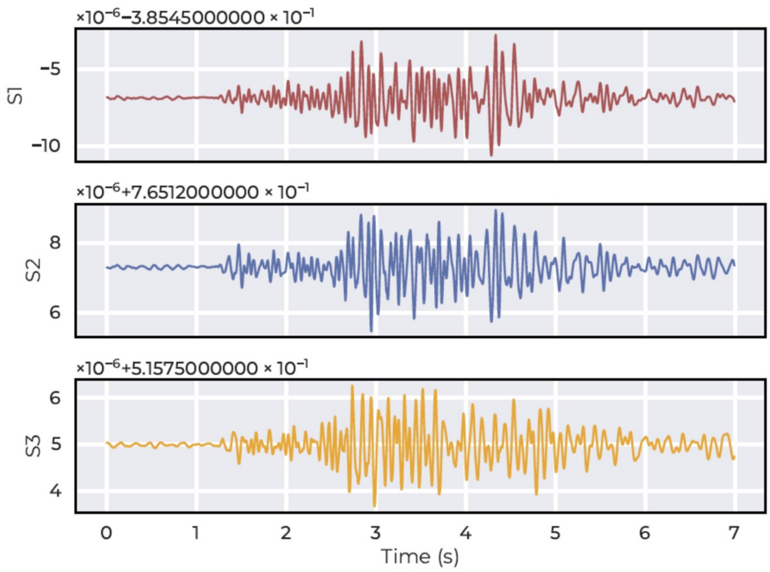

Fig. 3.3 Stokes parameters evolution simulated from DAS measurement.

Fig. 3.2 shows strain-induced perturbations along the fiber, expressed in nano-strain (nε), recorded by a DAS interrogator. These values were integrated in the Waveplate model to extract numerous set of polarization evolution over the simulated fiber. By injecting an input SoP, a 45 degrees linearly polarized light, and assigning random orientations angles, the model can then extract the SoP evolution starting from a 45 degree polarized light to the output SoP demonstrated in Fig. 3.3. Large simulated dataset can be extracted by assigning random set of major axis angles in each simulation for all the plates, resulting in large polarization evolution data for the same external event. The reason behind low SoP values is the weak impact of the recorded earthquake. Fig. 3.4 demonstrates the normalized output Stokes vectors for a subset of 4 realizations. Normalized stokes are used to remove the influence of signal power variation and isolate the SoP evolution.

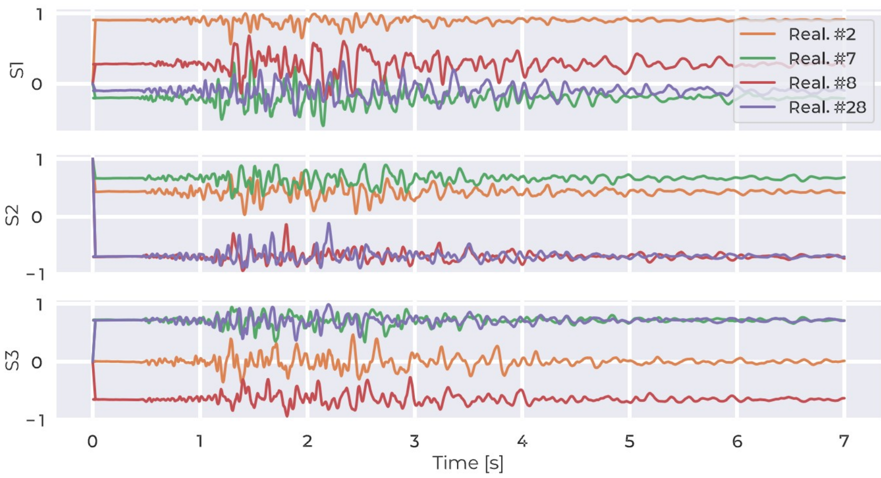

Fig. 3.4 Stokes vector: Four realization, where in each realization the Waveplate Model assign different set of random plates' angles.

Also, these stokes evolution could be represented in a poincare sphere as depicted in Fig. 3.5. We have performed a Montecarlo simulation campaign with 30 different random realizations of the birefringence orientation, keeping fixed the input SoP. We notice that different θ orientation sequences yield different Stokes, but still hold similar evolution of Fig. 3.2. The SoP change rate can be described by the sum of each squared Stokes vector variation:

$$\Delta SOP = \sqrt{dS_1^2 + dS_2^2 + dS_3^2} \tag{3.10}$$

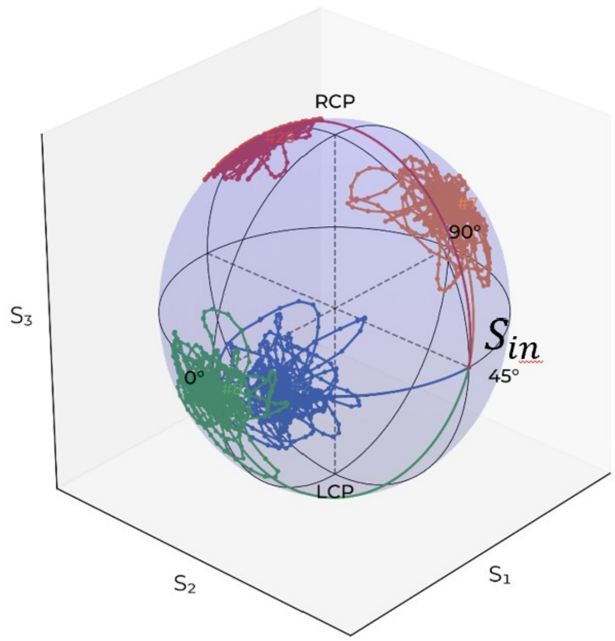

Fig. 3.5 Poincare Sphere Representation for the Four Evolution

The SoP change rate can be then considered as a reference signal, since it aggregates the Stokes peak variations observed alternatively in S_1, S_2, S_3.

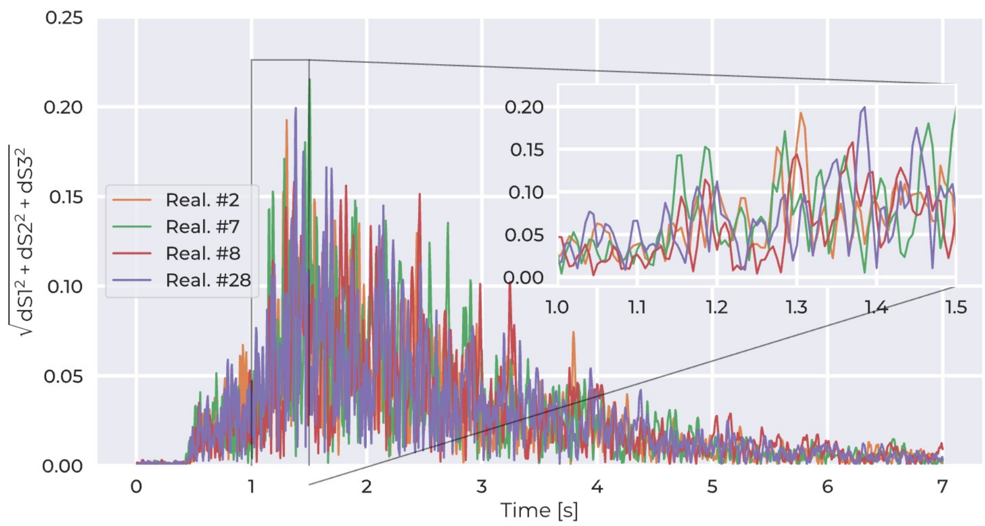

Fig. 3.6 SOP change rate time evolution for 4x simulated birefringence orientation random realizations.

These variations depend on the coupling between the fiber strain birefringence effect and the orientation realization. Fig. 3.6 demonstrates ΔSoP, where its clear that seismic wave information is preserved as all realizations shares almost the same peaks. Hence, one could measure the cross-correlation between different realizations' SoP change rate to test if the information about fiber strain is preserved. If yes, all the cross-correlations should yield maximum similarity at zero lag. This has been done for all the 30 realizations' combinations and it always confirmed the hypothesis. A subset of them is plotted in Fig. 3.7, clearly showing maximum similarity always at zero lag, although with a limited peak intensity.

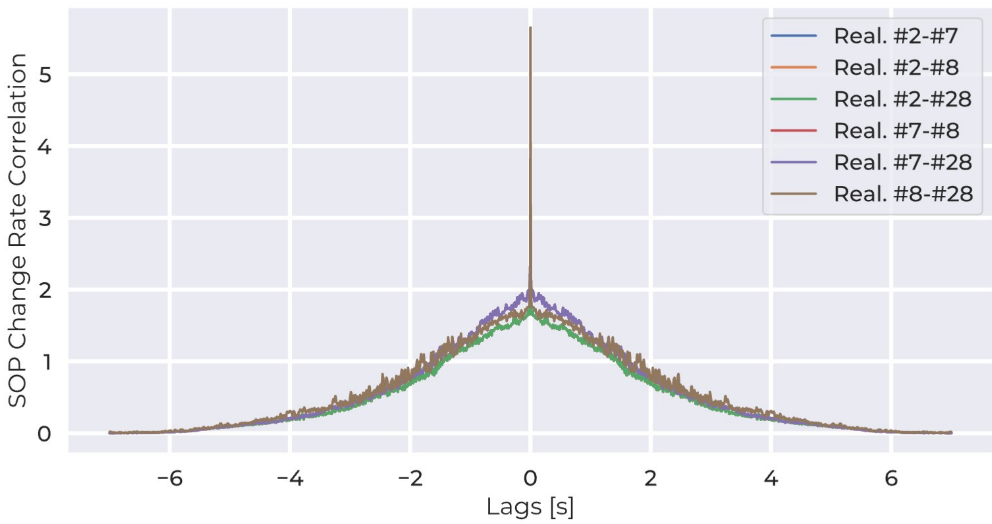

Fig. 3.7 SOP change rate cross-correlation of the 4x realizations' possible combinations.

At this development stage, the circular birefringence is neglected. The obtained SoP evolution can then be replicated in a laboratory-based environment using a polarization scrambler and a sensing device to monitor polarization alterations. This is useful for ML training, enabling external events detection. The replicated dataset can then be propagated through a deployed metropolitan fiber segment to test the detection in presence of other sources that may affect the polarization such as, propagation challenges or surrounding noise. We present this part just to show how DAS data recorded for any event can be incorporated into the Waveplate model, as in next parts DAS data-induced by a car passage is integrated into the model.

3.2 Interconnected Mesh Networks

On September 18, 2023 at 03:10:14 UTC and near Marradi - Florence, Italy, an earthquake with magnitude M4.9 struck the region. According to the Italian National Institute of Geophysics and Volcanology (INGV) [68], the earthquake epicenter depth was 8.4 Km with Longitude[E] equal to 11.587 an Latitude[N] to 44.058. To mimic the dynamics of its seismic waves, We employ SYNGINE tool to produce the displacement waveforms that closely resemble the seismic conditions seen during real impact [69]. SYNGINE is an open-source service which provides access to customized synthetic seismogram for selected Earth and Mars models [70]. It leverages locally saved, pre-computed Green's functions TB scale databases which correspond to different one dimensional reference earth models. The requested tailored seismogram is calculated using Instaseis, a python library built for storing wave-field databases with a fast extraction algorithm. By using Instaseis and obspy, one can emulate synthetic seismic events recorded by several seismic stations with varying distances from the epicenter. This is done by defining the seismic station-epicenter distance, earthquake magnitude and epicenter location, and defining the Earth model compatible with the earthquake region.

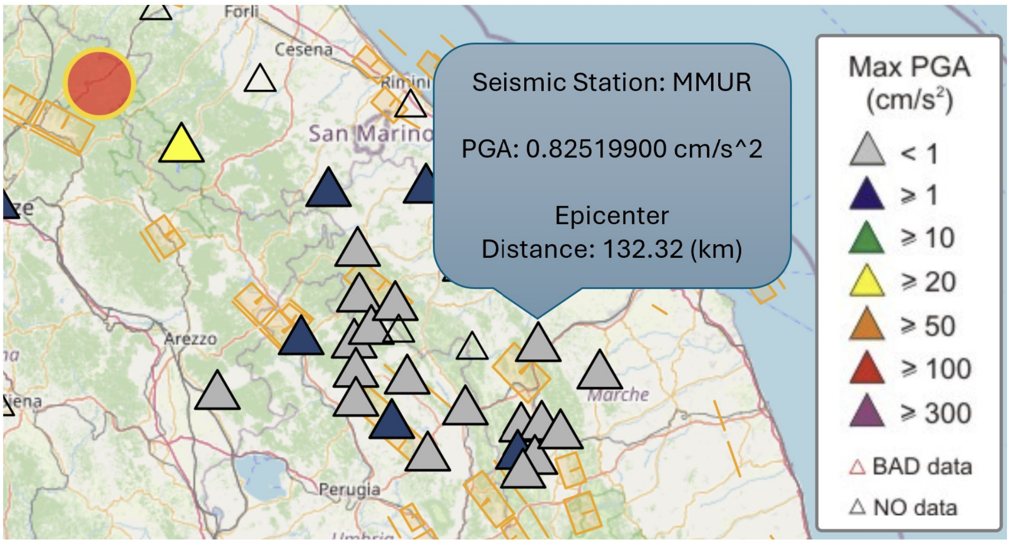

Fig. 3.8 Marradi Earthquake: Longitude[E] 11.587 & Latitude[N] 44.058 & Depth 8.4Km

After replicating the earthquake dynamics according to its data provided in INGV, We translate the extracted ground displacement values into nano-strain values along a 10 km fiber cable. To emulate distributed sensing, the strain signal is coupled along the fiber cable while considering an exponential attenuation to account for propagation effect. The cable is placed at the exact geographical coordinate of the Monte Murano MMUR seismic station with 43.4418 latitude, 12.9973 longitude, and 132.32 km far from the epicenter as demonstrated in Fig. 3.8. The fiber cable placed instead of MMUR is 10 km length segmented into 2500 waveplates, 4 meters of spatial resolution, 15 meters beat length and 20 meters of correlation length. The correlation length or the perturbation length is the average distance along the cable to maintain the fiber's polarization-altering properties before de-correlating. The Waveplate model generate a random angle between $-\pi/2$ and $\pi/2$ at each plate, where interpolation between these angles occurs at each correlation length (20 meters), this ensures that birefringence varies smoothly within each correlation length rather than randomly at every segment. The conversion between the displacement values (nm) extracted from SYNGINE and nano-strain values coupled along the fiber is done using the conventional iDAS conversion technique described in [71]. In this standard conversion, a reference gauge length of 10 m is assumed, where each 116 nm of displacement is equivalent to 11.6 nano-strain. This conversion factor is applied to calculate the aforementioned across our 4-meter spatial resolution grid to calculate the longitudinal impact $\Delta L_i/dz$. It is worth mentioning that in our model, we did not consider the transverse strain.

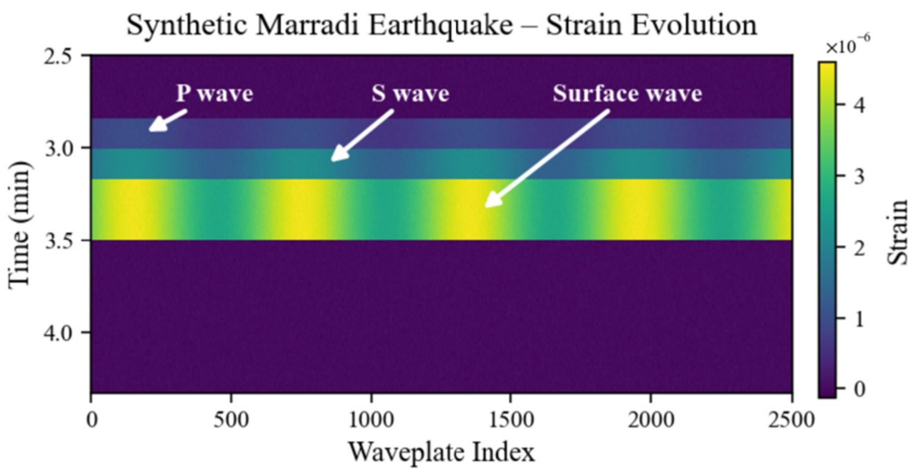

Fig. 3.9 Comparison between SYNGINE synthetic strain evolution.

The obtained strain (nε unit) curve is presented in Fig. 3.9. It clearly shows around 10 seconds lag between the P-wave and S-wave (171 to 180 seconds), around 10 seconds between S-wave and Surface wave (181 to 190 seconds), while the Surface wave last almost 20 seconds (191 to 210 seconds). The MMUR East recordings exhibits the same relative timing between seismic waves as demonstrated in Fig. 3.10. However, the absolute arrival times of all waves differ, as expected, because the SYNGINE tool is based on a one dimensional earth model, whereas the real Earth's crust is more accurately represented by three dimensional structural models, thereby affecting seismic wave propagation times. By injecting a 45 degrees linearly polarized light into the Waveplate model, a large set SoP evolutions is obtained, enabling SOPAS calculations.

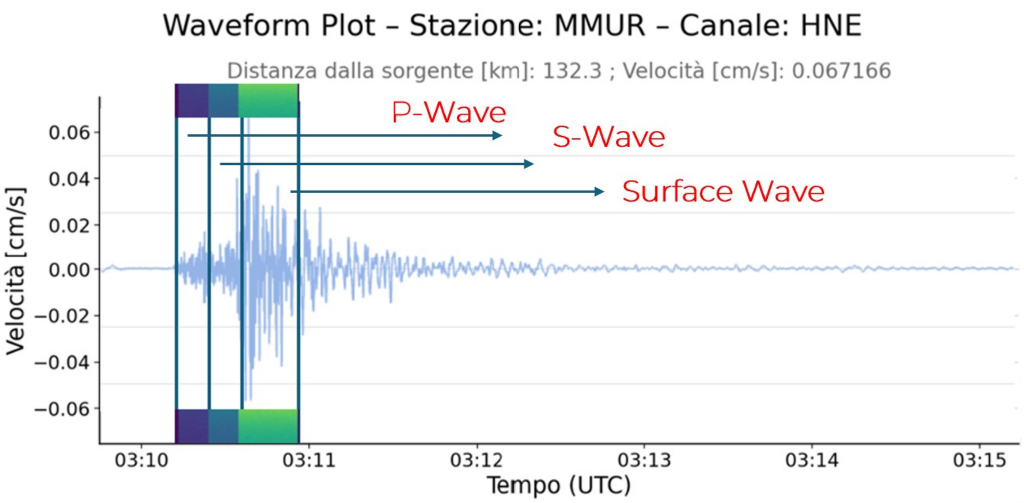

Fig. 3.10 The recorded seismic waveform at station MMUR (East), demonstrating consistent seismic phase timing but shifted arrival times due to differences between 1D and 3D Earth models.

We propose to train a Bi-GRU with an attention mechanism model on obtained SOPAS time-series dataset with single feature defined as the norm of SOPAS variation in time. The 80% of the dataset is used for training, 20% for validation and 20% for testing purpose. In order to simulate realistic environmental conditions and assess the robustness of the model, a Gaussian noise was added to the original signal, with a standard deviation equal to 20% of that of the original signal, as in a terrestrial scenario the SoP measurements may be impaired by polarization noise coming from other anthropic activities. The proposed model has one input layer with 50 neurons, Bi-GRU layer with 128 neurons in each direction, attention layer, GRU layer with 32 neurons and an output layer with 4 neurons for classification of No Earthquake, P-wave, S-wave and Surface wave. Bi-GRU layer employed tanh activation function whereas attention layer, GRU layer and output layer use softmax activation function for the prediction. The model is trained over 1000 epochs using an Adaptive Learning Rate Optimizer (ADAM) and a categorical cross-entropy loss function defined as the measure of difference between the predicted class probabilities and the true class labels. As mentioned earlier, Bi-GRU is the variant of RNN, which can process the data in the form of sequences in both forward and backward directions. Given an input sequence $X = (x_1, x_2, ..., x_T)$ of length $T = 20$, the forward and backward hidden states are computed and then passed to the attention layer. The attention layer compute the context vector to learn to focus on the most useful information in the input sequences. The learned context vector is then passed to the final dense layer for generating class probabilities. We consider the F1 score (balanced performance), recall (detection coverage), precision (prediction quality) and accuracy (overall correctness) metrics to verify the effectiveness of our model. Fig. 3.11 shows the precision, recall,F1 score and accuracy of our model on validation dataset during the training against number of epochs.

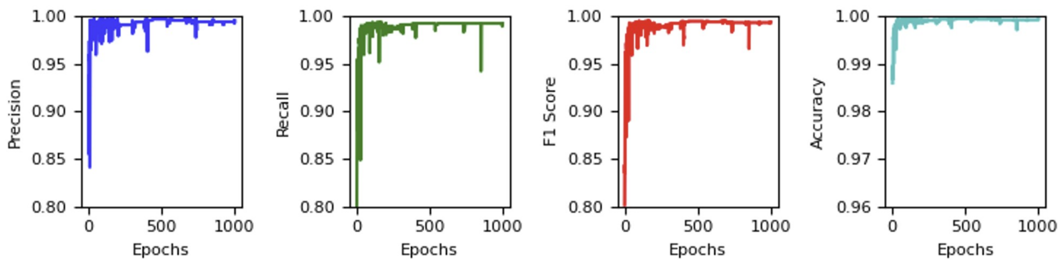

Fig. 3.11 Precision, Recall, F1 score, and Accuracy during training on validation dataset

It is evident from the results that all the metrics show a consistent and promising performance, reaching nearly 98% accuracy in detecting different classes of seismic activity. The model demonstrated the ability to detect P-waves in one second detection time window, enabling early warning time of approximately 9 seconds for nearby locations (Florence) and up to 22 seconds for cities farther away (Arezzo). P-wave detection accuracy on the test data reached about 97%, enabling theoretical early earthquake warning system designed to detect the arrival of the P-wave [69]. Up until this point, the very first milestone of this thesis is accomplished. Now instead of replicating the earthquake dynamics using SYNGINE, we overcome the one dimensional Earth's crust representation and extracted, directly through INGV, real ground displacement data from seven local earthquakes recorded in the Modena region. The earthquakes magnitudes chosen are M4, M4.3, M4.5, M4.7, M5.1, M5.3 and M5.8 [72][73]. The objective is to integrate strain values caused by these displacements into fiber cables configured exactly as mentioned earlier with similar length, spatial resolution, beat length and correlation length. The same linearly polarized light is injected into the model to conduct 50 simulations with random orientations each for each earthquake. The evolution of the SoP files and subsequently the SOPAS values, result in a total of 350 simulations used for training and validating an ML algorithm learning from all earthquakes. A Temporal Fusion Attention Network (TFAN) based on neural network architecture is utilized for ML modeling, in which we combine the Temporal Convolution Network (TCN) [74], LSTM, and attention mechanism. The term "temporal" in the model's name indicates the focus on temporal data, capturing patterns and dependencies over time. "Fusion" represents features from both TCN and LSTM layers. As for "Attention", it highlights the utilization of attention mechanisms to dynamically weigh the importance of different steps.

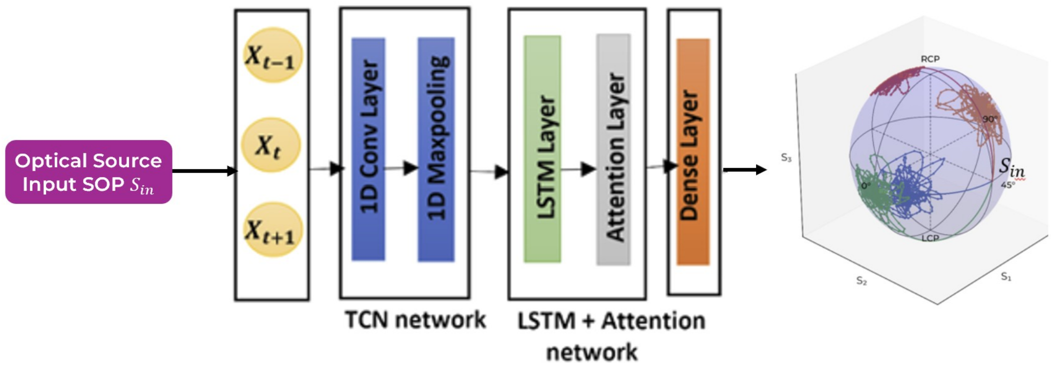

Fig. 3.12 ML Model Architecture

As shown in Fig. 3.12, the model architecture is structured to process time series data, followed by TCN layer designed to capture temporal patterns. An LSTM layer is incorporated for long term dependencies, with attention mechanism to focus on significant time steps. The output layer facilitates multi-class classification with softmax activation.

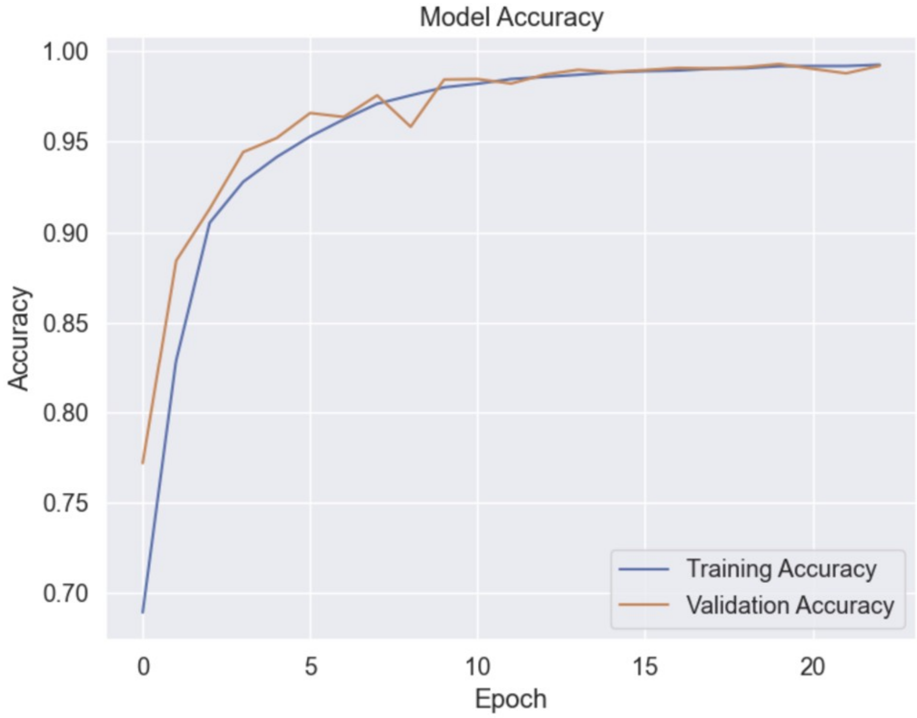

Fig. 3.13 ML Model Resulting Accuracy

ML model training involves categorical cross-entropy loss, Adam optimization, and early stopping to mitigate over-fitting. Almost 60% of the SOPAS data used for training, 20% for validation and 20% for testing. In Fig. 3.13, we show the model training and validation accuracy. The graph displays the accuracy over a sequence of epochs. The blue line represents the training accuracy, which increases rapidly, indicating effective initial training. Meanwhile, the orange line signifies the validation accuracy, assessing the model's performance on new unseen data. The close alignment of these curves indicates that the model has been well-generalized with minimal risk of over-fitting. As epochs progress, both curves reach noticeable accuracy rates, implying that further training is unlikely to yield significant improvements. The model shows promising predictive precision, with training and validation accuracy exceeding 95%. For testing the model, we used the M4.3 earthquake struck in the region of Modena on the 23rd of may, 2012. The objective is to leverage three interconnected terrestrial optical mesh networks in the region as a smart sensing grid driven by the aforementioned trained TFAN-based ML model, where we extracted the real ground motion data recorded by three seismic station (T0821 - 23.14 km far from the epicenter, MNTV - 47.88 km far from the epicenter and MNTV - 61.45 km far from the epicenter) as demonstrated in Fig. 3.15.

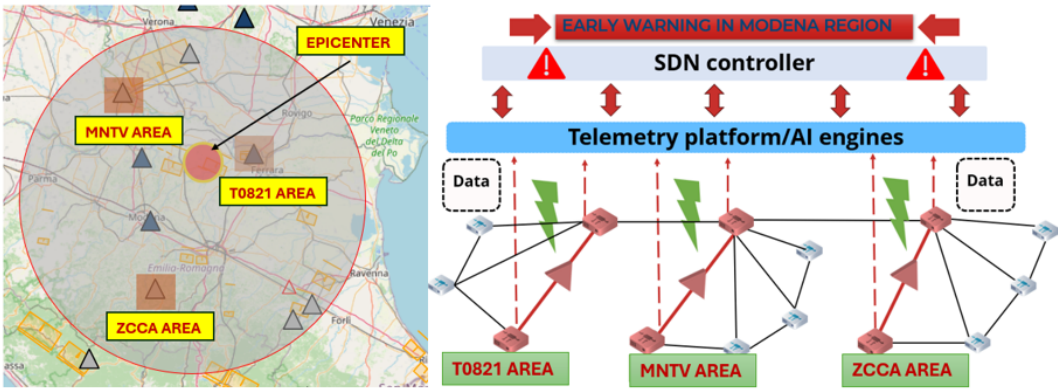

Fig. 3.14 M4.3 Earthquake Origin Time: 2012-05-23 21:41:18 (UTC) | Region: MODENA and corresponding Interconnected Sensing Grid in the Modena Region

Displacement values were then converted into strain values coupled along three sensing fibers positioned to correspond with seismic stations' geographical coordinates in the three distinct areas. Network equipments in each network will continuously send information to the network controller overseeing all mesh networks. We aim to confirm the event from three sensing areas, localize the epicenter and determine the epicenter to station/fiber-substitute distance, by applying triangulation method that we detail later, thereby generating early warnings to urban areas according to the closest area to the epicenter and moving further away.

3.2.1 TFAN Model Testing

According to the Central Italian Apennines (CIA) Velocity model [75], the time window between the P-wave and the arrival of Surface wave increases by the increase of distance from the epicenter, similarly for the P-wave arrival time.

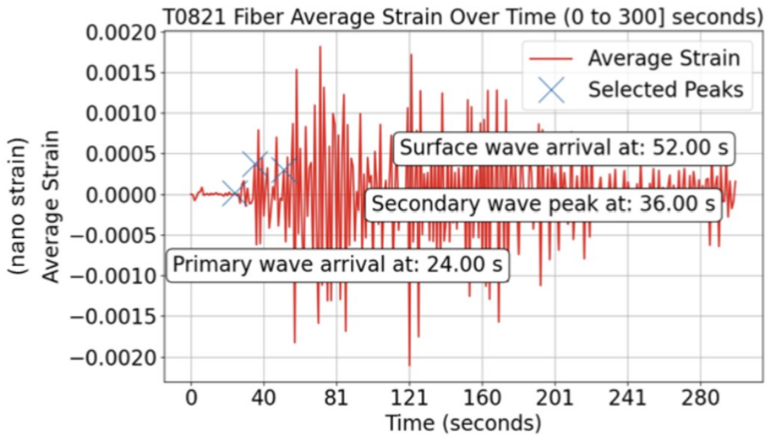

Fig. 3.15 Strain Evolution over T0821 Fiber

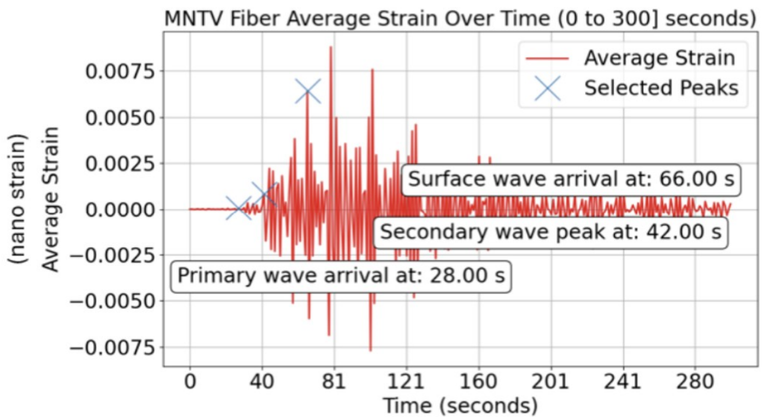

Fig. 3.16 Strain Evolution over MNTV Fiber

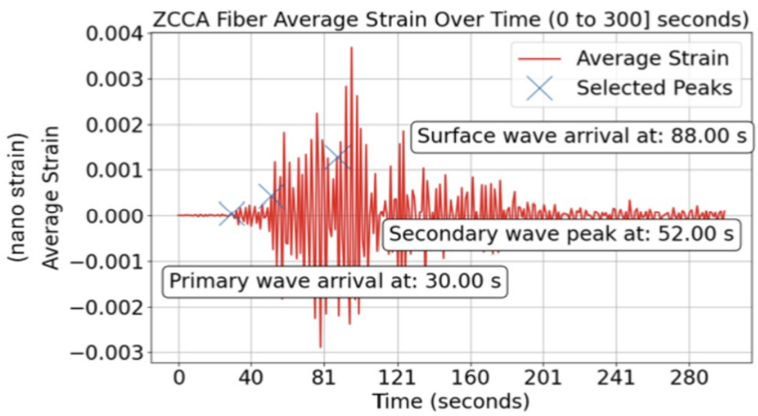

Fig. 3.17 Strain Evolution over ZCCA Fiber

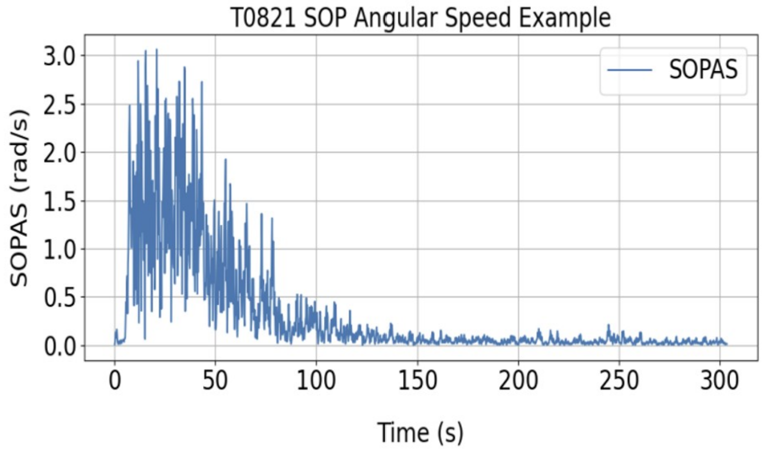

Fig. 3.18 SOPAS Evolution over T0821 Fiber

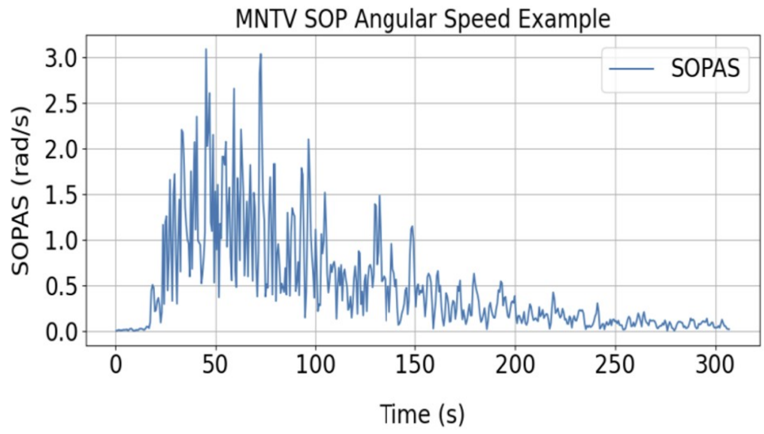

Fig. 3.19 SOPAS Evolution over MNTV Fiber

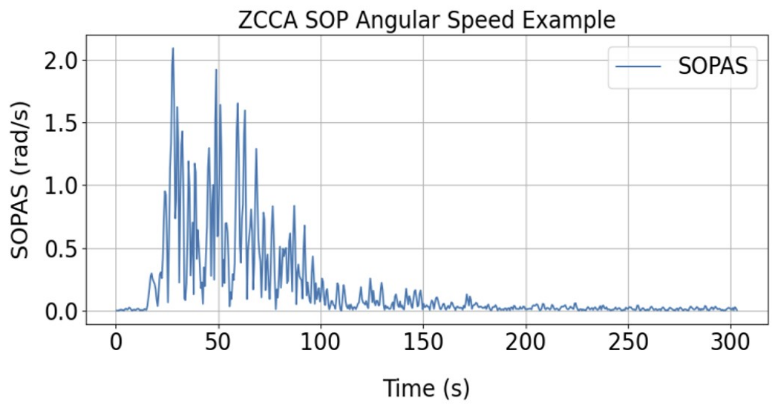

Fig. 3.20 SOPAS Evolution over ZCCA Fiber

The earthquake struck at 21:41:18 UTC, where the P-wave arrives at T0821 after 24 seconds, 28 seconds at MNTV and 30 seconds at ZCCA as shown in Fig. 3.15, Fig. 3.16, and Fig. 3.17 respectively. INGV recorded signals were used as ground truth data. An example of one SOPAS simulation for each sensing fiber substituting each seismic station is shown in Fig. 3.18, Fig. 3.19, Fig. 3.20 respectively. SOPAS datasets extracted from all fibers is utilized to test the trained ML model. We detail in this part the ML findings. We present in Fig. 3.21, Fig. 3.22, Fig. 3.23 the Confusion matrices for each fiber substitute respectively. The confusion matrix shows a table to visualize the performance of a classification model, or seismic event classification system. Each matrix is a measure of accuracy for predicting four categories: NO EQ (No Earthquake), P-wave(Primary wave), S-wave (Secondary wave) and Surface wave. For T0821 fiber substitute demonstrated in Fig. 3.21, show that the system accurately detects 'No EQ' most of the time with 1048 correct detections, 19 wrong detected as P-wave, 0 as S-wave and 4 as Surface wave. For P-wave, it correctly identified 538 instances, missing only one as 'No EQ' and one as S-wave. Following this analysis into all matrices, 538 correct P-wave detection out of 540 events for T0821 fiber substitute, 358 out of 360 detection for MNTV fiber substitute demonstrated in Fig. 3.22, and 1758 out 1760 for ZCCA fiber substitute demonstrated in Fig. 3.23.

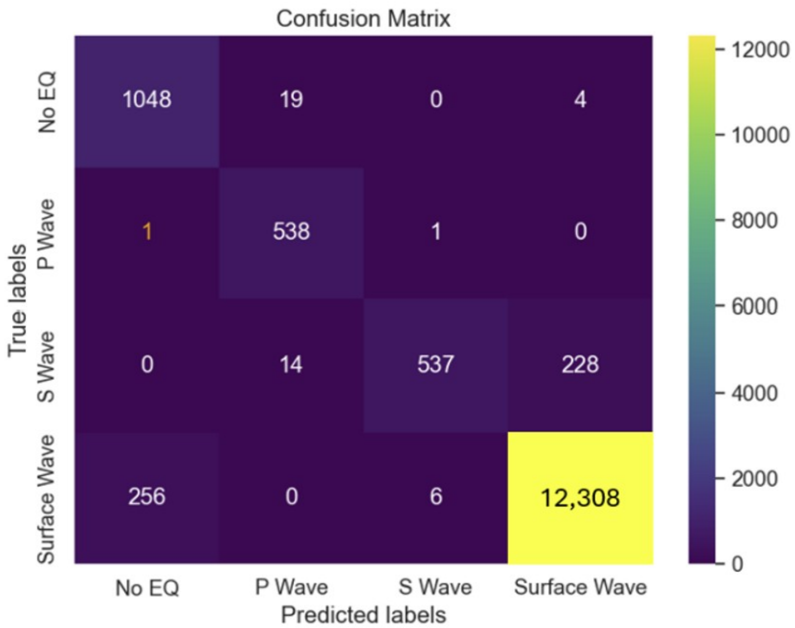

Fig. 3.21 Confusion matrix over T0821 fiber

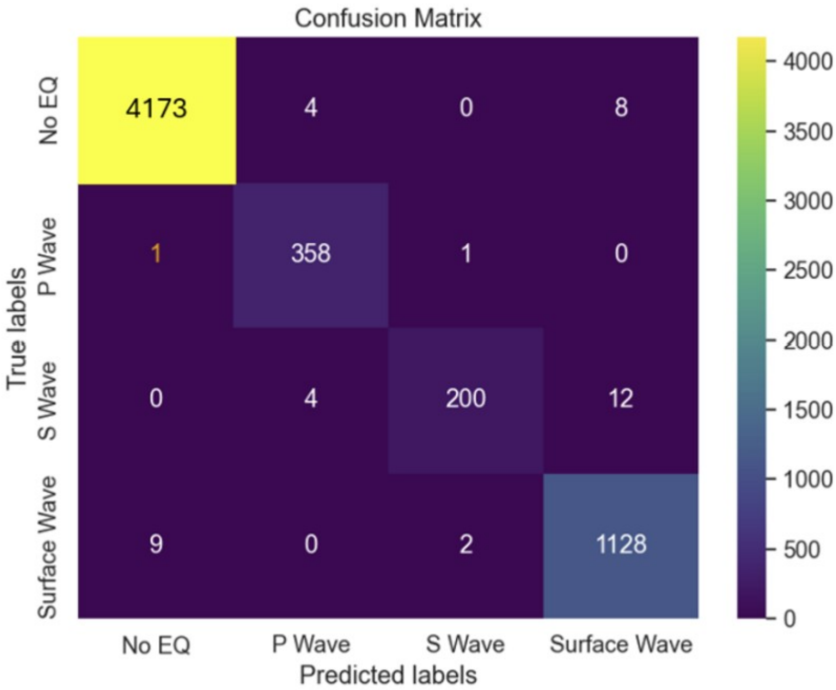

Fig. 3.22 Confusion matrix over MNTV fiber

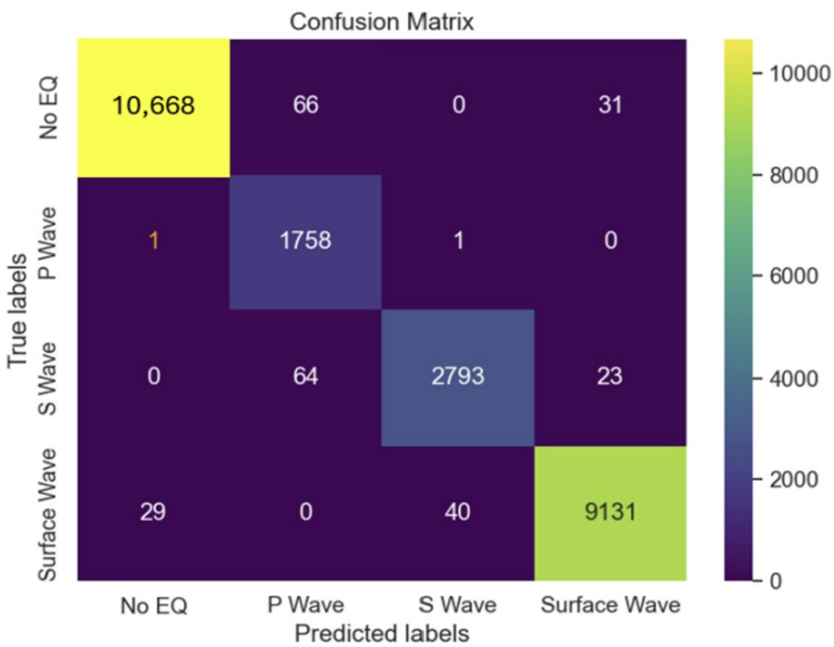

Fig. 3.23 Confusion matrix over ZCCA fiber

Consequently, the system modeling shows low false positive rates and high level of efficiency with 98% of accuracy rate in detecting P-waves, an essential component in early earthquake detection and seismic analysis. The results of ML fitting over SOPAS data that demonstrate one-second of ML detection time over all fiber upon direct P-waves arrivals, which means that if the P-wave starts at t = 0, the detection will occur at t = 1. By substituting this one second from the P-wave arrival time at each fiber, and accounting to the time between the Surface wave and P-wave one each, the time available for the T0821 area to take countermeasures is 21 seconds, 35 seconds for the MNTV area and 57 seconds for the ZCCA area.

3.2.2 Triangulation Method

This method employed by the network controller to pinpoint the earthquake's epicenter and determine the station/Fiber distance from the epicenter to generate early warning according to the nearest area from the epicenter and progress to those further away. The simulator uses measurements of seismic wave arrival times at different stations and their geographical coordinates to estimate the most probable epicenter location, by minimizing the differences between expected and observed arrival times. The simulator defines the speed at which the seismic wave propagate through the Earth's crust, and specify the coordinates and the exact time the wave was detected at each station. The simulator then transforms the wave arrival at each station into seconds relative to the first recorded arrival, to employ a residual function after, that calculate the discrepancies between measured and theoretical expected arrival times. This is done by measuring the distance of each station from a hypothetical epicenter, converting these distances to expected times based on the seismic wave velocity, and then summing the squared differences to create an objective function for optimization. The simulator assume an initial epicenter positioned at the centroid of the triangle formed by the three stations. A minimization function is then utilized to minimize the calculated residual sum.

Table 3.1 Comparison of epicenter locations and distances from seismic stations

	Epicenter Location		**Station to Epicenter Distance (km)**		
Source	**Longitude**	**Latitude**	**MNTV**	**ZCCA**	**T0821**
INGV Recording	11.2510	44.8680	47.88	61.45	23.14
Triangulation Simulator	11.2846	44.8705	49.59	63.08	20.48

Table 3.1 presents a comparative analysis between the actual seismic data recorded by INGV and the theoretical detection from the Triangulation Simulator. The simulator shows almost identical measurements for both epicenter latitude and longitude. Furthermore, the distances from seismic stations (T0821, MNTV and ZCCA) to the estimated epicenter location show small discrepancies, and this is due to the fact of minor error in picking up the peaks from the graphs, and could also be from displacement to strain conversion that affect determining the arrival times of P-waves at each station. Although, The triangulation method show efficiency in its estimation. Consequently, T0821 area is the first to be notified by the network controller for the upcoming seismic event with 21 seconds time-lag for emergency response before the Surface wave struck, followed by MNTV area with 35 seconds time lag and then ZCCA with 57 seconds. To conclude, this part shows the efficiency of using interconnected fiber optic mesh networks as a smart sensing and localization grid, leveraging machine learning for early earthquake detection. By integrating real displacement data from seven earthquake events of varying magnitudes recorded by the INGV in Modena region, Italy. In the next part of this chapter, we will integrate a car passage strain, recorded by a DAS interrogator, along with the aformentioned M4.3 earthquake strain, train the ML on car passage-induced SoP data and then try to distinguish the P-wave despite the noisy environment.

3.2.3 Additive Gaussian Noise

In order to mimic realistic environmental conditions and assess the robustness of TFAN model, additive Gaussian noise is added to the resulting SOPAS data as demonstrated in Fig. 3.24.

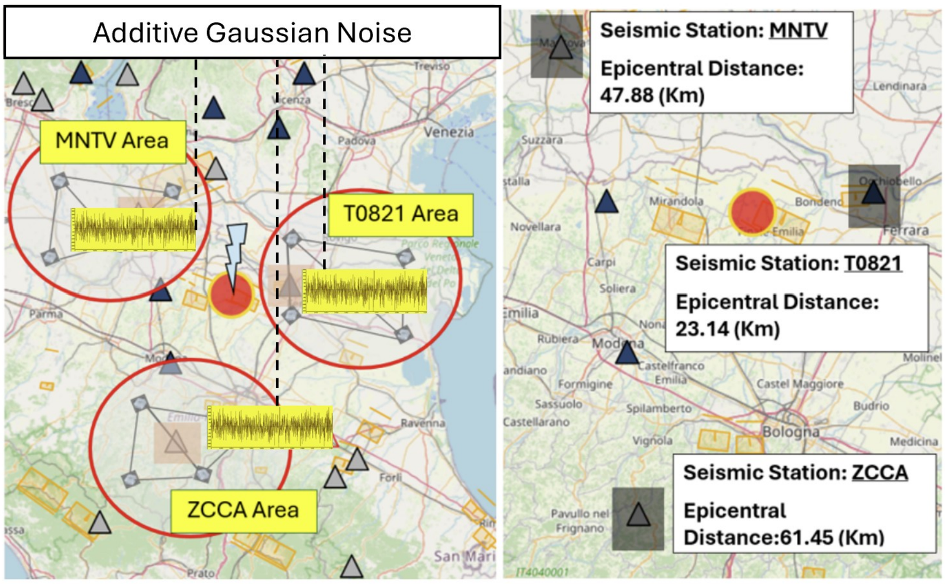

Fig. 3.24 Additive Gaussian Noise is Added to the SOPAS-Induced by Seismic data recorded by the Three Seismic Stations.

The main idea of our approach is to add Gaussian noise to the original SOPAS values induced by seismic data recorded over the aforementioned T0821, MNTV and ZCCA seismic stations. We computed signals' standard deviations and used the desired signal-to-noise-ratio (SNR) of 0.1 (linear scale) to determine the corresponding noise level, emulating a highly noisy sensing environment. Subsequently, this noise was integrated over all data to generate a more reliable dataset that mimics the variability present in real-world case scenarios. The TFAN model is tested again to asses it's accuracy demonstrated in Fig. 3.25 and loss demonstrated in Fig. 3.26. Referring to Fig. 3.25, the model training and validation accuracy curves increase rapidly and stabilize around 95%, indicating that the model learns quickly and generalizes well. As for the model loss, both curves stabilize near zero, indicating effective learning and minimal over-fitting.

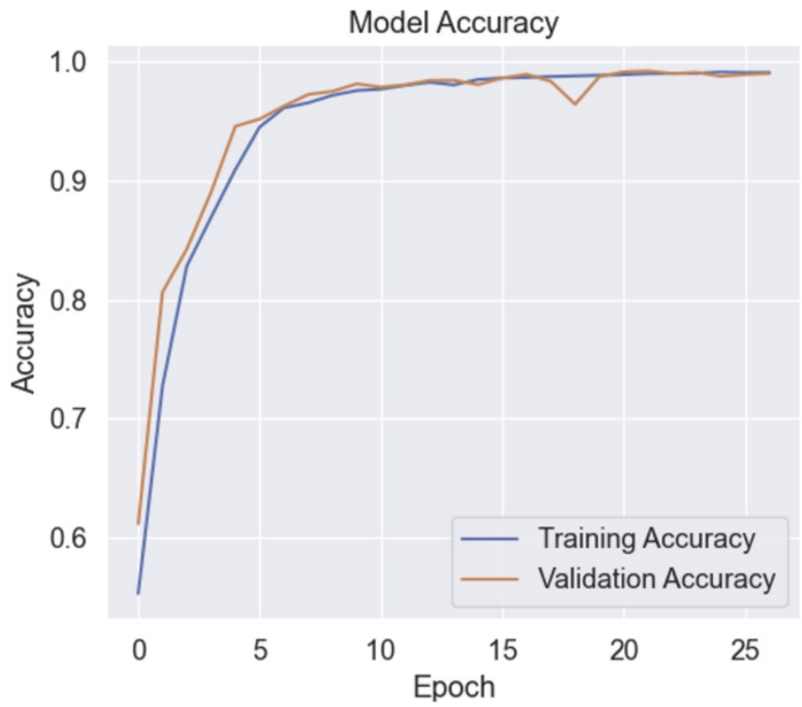

Fig. 3.25 ML Model Accuracy in the presence of Additive Gaussian Noise.

Fig. 3.26 ML Model Loss in the presence of Additive Gaussian Noise.

The confusion matrix of the TFAN model demonstrated in Fig. 3.27, shows detection precision of the model.

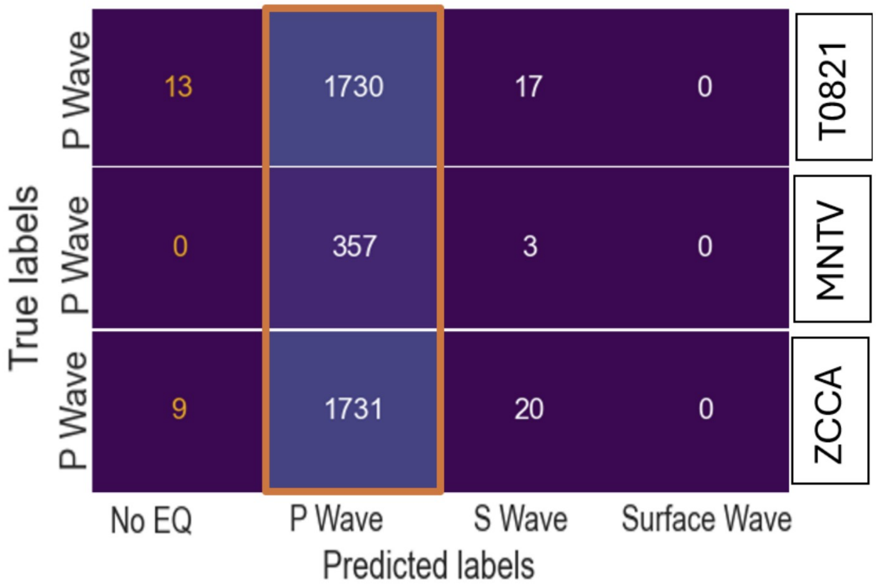

Fig. 3.27 Confusion Matric of TFAN Model, Tested in the Presence of Additive Gaussian Noise.

In this matrix, we highlight the detection of the P-wave in each of three SOPAS sets-induced by the seismic activities recorded in each of the three stations. For instance, for T0281/Fiber, 1730 correct detection out of 1760. The model shows 98% overall accuracy for earthquake primary wave detection and one second detection time. This indicates that refining our model against noise level comparing to what we presented earlier, leads to the same results, where the optical network controller overseeing all interconnected networks can still inform all municipalities about an upcoming seismic event after the third confirmation from ZCCA fiber and is able to detect primary waves in noisy environment. Consequently, and similarly to the aforementioned, the T0821 area is the first to be notified with a 21 seconds time lag for an emergency response before the surface wave strikes, followed by the MNTV area with a 35 seconds time lag and then the ZCCA area with a 57 seconds time lag. Up to this point, we investigated the use of interconnected fiber optic mesh networks as a sensing-localization grid for accurate ML-based earthquake early warning approach in a noisy environment. Data were extrapolated from real earthquakes of different magnitudes recorded by INGV in the region of Modena, Italy.

3.3 Noisy Earthquake and Model Classification

Like any other stress affecting the fiber buried underground, car vehicles pressing down on the road may affect the physical configuration of the light wave propagating along the cable due to the subsurface deformation induced from the weight applied. This deformation leads to a strain measurable amplitude. When the car is moving, the changes in the strain field as the car passes by are recorded as a strain rate. The deformation at a point in the subsurface is described by Flamant-Boussinesq approximation [76]:

$$u_x(x, y, z) = \frac{F\,x}{4\pi G\,r^2}\left(\frac{z}{r} + \frac{2\nu - 1}{1 + \frac{z}{r}}\right) \tag{3.11}$$

The particle displacement in the x-direction, denoted as u_x, is defined parallel to the road and the fiber at a point (x, y, z) relative to a point load located at the origin, with y being the distance perpendicular to the road/fiber and z the depth beneath the surface. The distance from the origin is given by $r = \sqrt{x^2 + y^2 + z^2}$. The point load applies a total force F into an infinite half-space characterized by a uniform shear modulus G and Poisson's ratio ν. The particle velocity $\dot{u}_x$ is obtained by differentiating u_x with respect to time, and noting that $\dot{x}$ is the velocity of the car traveling in the x-direction. There are two types of deformations induced by a car passage, the quasi-static deformation that is controlled by the distance between the fiber and the road, and the dynamic deformation that is determined by the interactions between the car tires and the road. Dynamic deformation generate surface waves that travel away at seismic speed and are better to be integrated over earthquake strain as the quasi-static deformation is a very simple impulse response. The DAS systems is not measuring particle motions, but rather the average longitudinal strain rate between two sensing points. Using Frequency Domain Integration (FDI) technique, we convert the strain rate of a car passage to strain. FDI technique consists of dividing the data by $-2j\pi n$ in the frequency domain, where n is the frequency index, and then transformed back into the time domain.

$$\text{Strain}(t) = \mathcal{F}^{-1}\left\{\frac{\mathcal{F}\{\text{Strain Rate}(t)\}}{-2j\pi n}\right\} \tag{3.12}$$

In contrast, for earthquake signals, we integrate the conventional i-DAS conversion in order to convert earthquake ground displacement values to strain-time matrix, and multiplying by 1×10^9 to obtain the strain. Fig. 3.28 refers to strain rate recorded by DAS in the dynamic frequency band (5-20 Hz) over almost 4 seconds of time period [77].

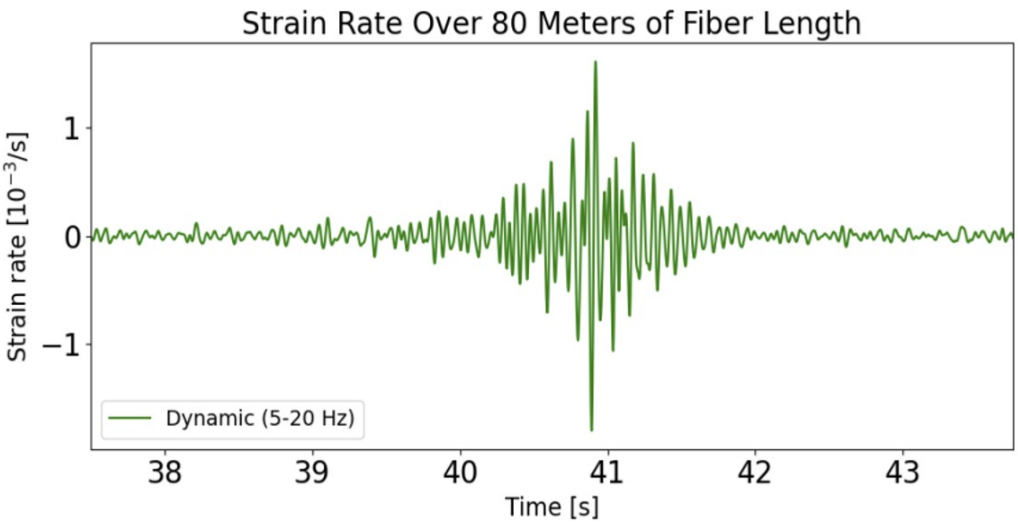

Fig. 3.28 Strain Rate Induced by a Car Passage - The Strain is induced by the dynamic deformation of the vehicles' weight. Strain rate was recorded by DAS over 80 meters fiber length.

We then extracted the samples corresponding to the strain induced by the car passage over a one-second interval, specifically from 40.5 to 41.5 seconds. These samples were then added to the strain values induced by the M4.3 earthquake and demonstrated in Fig. 3.29.

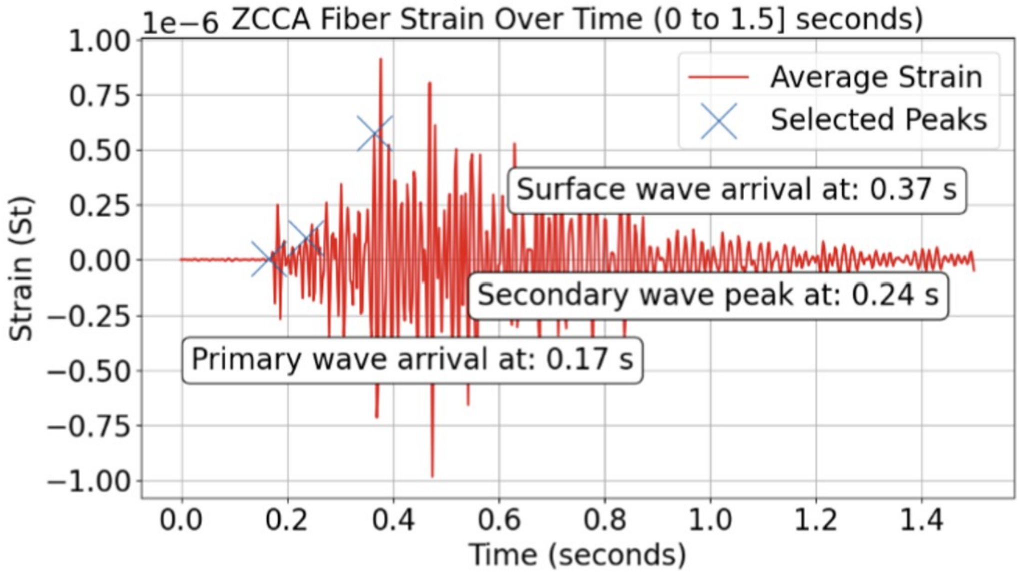

Fig. 3.29 Strain Induced by Earthquake Ground Displacement Values Recorded by INGV over 80 meters Fiber Length - Slicing time interval 0 to 1.5 out of 0 to 4 seconds for better visualization

To add the two strains, fiber cables should have the same characteristics. In the previous part, we collected data from the ZCCA seismic station located in Zocca municipality in Modena, which is tens of kilometers far from the Modena earthquake epicenter. Then, we integrated the strain induced along a 10 km fiber positioned at the exact geographical coordinates as the aforementioned stations. However, the extracted DAS data from [77] used an 80 meter fiber cable, therefore we selected an equivalent section length from ZCCA fiber. This ensures the same spatial resolution (3.2 meters) and the same sampling rate (400 Hz) are maintained. Selecting a small section of the fiber, compared to the original 10 km length, will affect the time lag between the surface and primary wave arrivals. However, our focus in this part is not on early warning generation but instead to detect the primary wave in a noisy environment, and to demonstrate our model's capability to distinguish between various environmental events. We integrate each of the two strains separately in the Waveplate model in order to visualize a sample of the SOPAS induced by each strain at the output of the fiber as shown in Fig. 3.30.

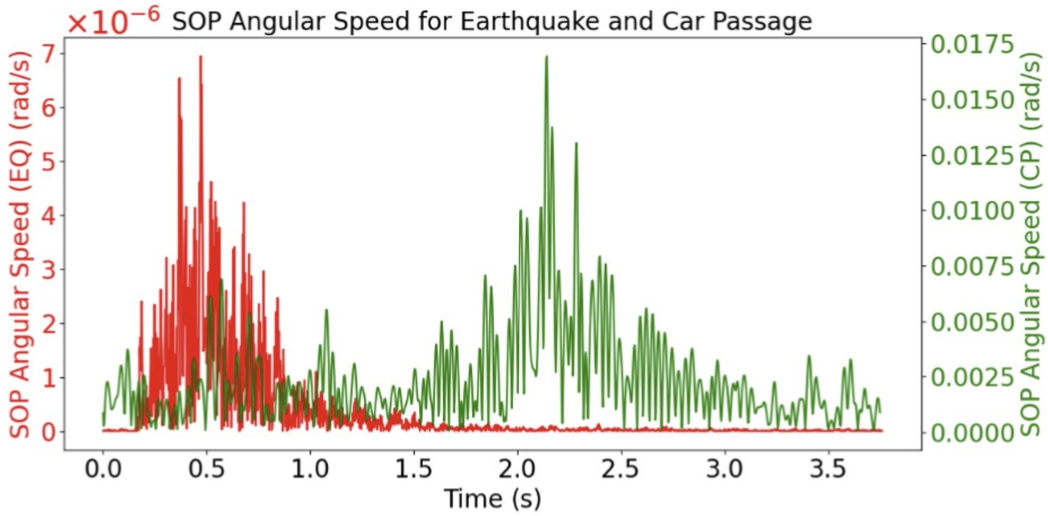

Fig. 3.30 Red - SOPAS induced by Earthquake Strain; Green - SOPAS induced by Car Passage Strain.

Fig. 3.30 shows an ascending pattern in the red curve (SOPAS induced by the earthquake), and this is because the magnitude increases from the primary wave to the surface wave. The green curve (SOPAS induced by the car passage) shows almost a peak at around 2 seconds. To distinguish between the strains and look up for the resulting SOPAS, we add up the one second time window [40.5s - 41.5s], which is equivalent to [1.5s - 2.5s] of the car passage strain, into the earthquake strain starting from 0.2 seconds. Referring to to the right of Fig. 3.28, we have chosen 0.2 seconds to have A = [0.17s - 0.2s], a time interval holding information about primary wave with no car passage and B = [0.2s - 0.24s], a time interval holding noisy information about the primary wave disturbed by a car passage. The one second integrated strain of car passage will end at 1.2 seconds, while the earthquake wave dissipates at almost 1 second. This introduces another class with time interval C = [1s - 1.2s], where only car passage strain is present without any overlapping seismic wave. This additive approach will facilitates the detection of the primary wave in a noisy environment, allowing to distinguish between both events. For that purpose, we ran numerous simulations for SOPAS-induced additive strain. One example of the latter is demonstrated in Fig. 3.31.

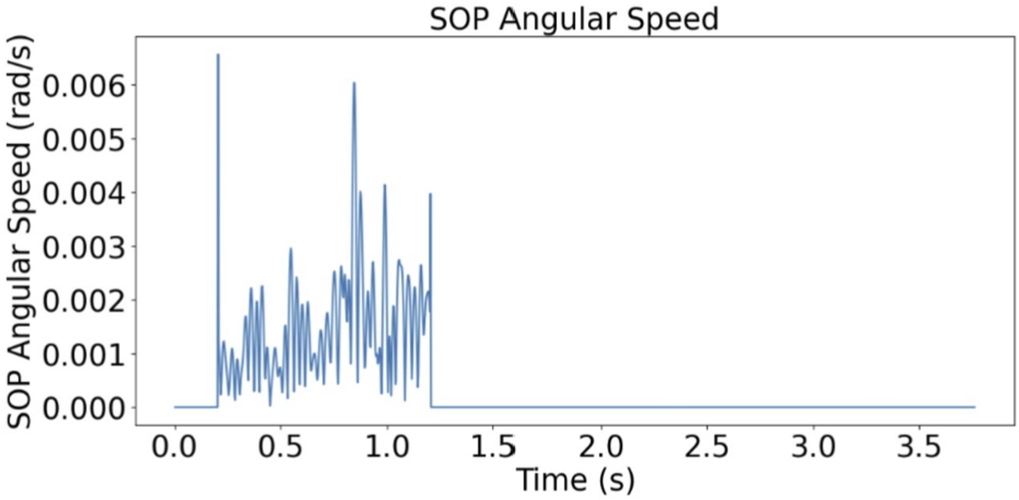

Fig. 3.31 SOPAS Induced by Additive Strain - Car passage strain over the strain induced by the earthquake

This large set of SOPAS data is divided into percentages for training and validation, with the remainder used for testing, before being utilized in an ML model for detection purposes of all events. The proposed ML model leverages a deep learning architecture designed to capture temporal dependencies and important features within sequential data for a multi-class classification task. The model begins with an input layer to collect sequences of time steps length corresponding to the number of features in input data (SOPAS). This input is analyzed by four LSTM layers. The first LSTM layer consists of 64 units that returns back the full sequence of outputs to allow subsequent layers to further process temporal dependency information. The second LSTM layer increases the units to 128, improving the model's ability to identify complex patterns in the data, while still returning back the full sequence of outputs. The third and fourth LSTM layers consist of 64 units each, utilized for refining the sequence representations [72]. Moreover, the model integrates an attention mechanism. This mechanism compute a weighted sum of the LSTM outputs through a dot product operation, highlighting the most informative parts of the sequence. The result is then passed to a fully connected layer of 6 units and softmax activation, which outputs the probability of each class: Primary Wave and Car Passage (P wave-CP), Secondary Wave and Car Passage (S wave-CP), Surface Wave and Car Passage (Surface Wave-CP), Primary Wave and No Car Passage (P wave-NoCP) and No Earthquake but Car Passage (No

EQ-CP). Early detection of earthquake in a noisy environment correspond to (P wave-CP), while distinguishing between both events corresponds to two classes (No EQ-CP to identify car passage event and P wave-NoCP to identify the arrival of earthquake primary wave). The model is compiled with the Adam optimizer and sparse categorical cross-entropy loss. This compilation makes it suitable for integer labeling for the multi-class classification tasks (0 as No Earthquake, 1 as Primary wave, 2 as Secondary Wave, 3 as Surface Wave, 4 as Car Passage and 5 as No Car Passage). Thus, combining two classes of events will hold two integer labels (for example, P wave-CP is equivalent to 14). To enhance generalization and prevent over-fitting, early stopping is implemented to monitor the validation loss and stop training if no improvement is observed over three consecutive epochs, while also to restore the best weights observed during training. This architecture efficiently combines the effectiveness of LSTM networks along with attention mechanisms, making it well-suited for complex sequential data tasks. The model is trained for 100 epochs. Almost 60% of the SOPAS data is used for training, 20% for validation and 20% for testing. Exploiting the Waveplate model, we ran 300 simulations induced by the additive strain.

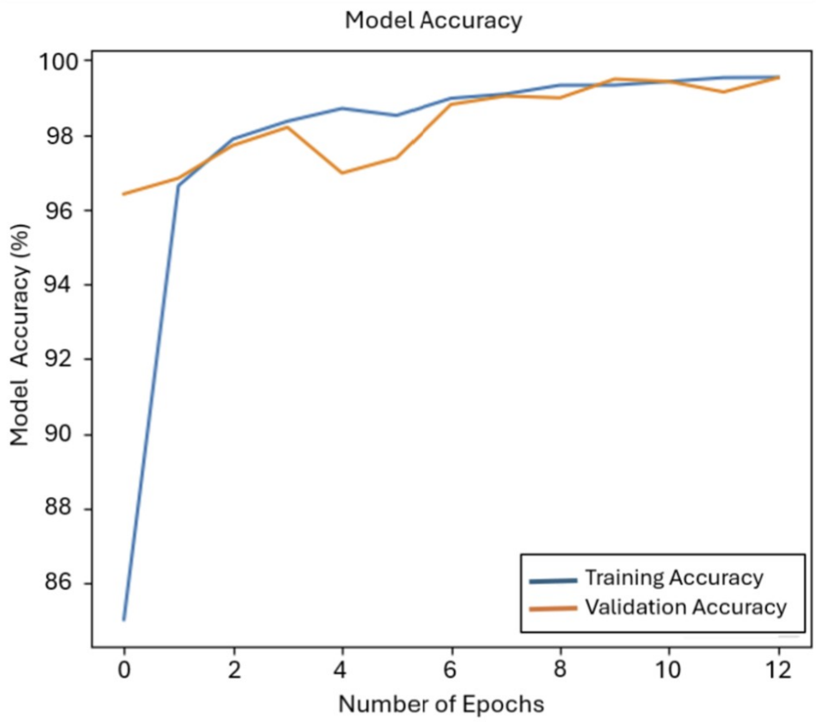

Fig. 3.32 ML Model Training and Validation Accuracy (Left).

Fig. 3.32 shows the model training and validation accuracy, and displays the accuracy of the ML model over a sequence of epochs. The model's training accuracy curve shown in blue increases rapidly, indicating effective initial training. The validation accuracy curve shown in orange evaluates the model's ability to predict new unseen data. The proximity of the two curves indicates that the model has been generalized well with a minimal risk of over-fitting. As the number of epochs increases, both curves reach noticeable accuracy rates, implying that additional training is unlikely to yield significant improvements. The model shows a promising level of predictive precision for both training and validation accuracy dataset exceeding 95% of accuracy rates. While for the model training and validation loss shown right of Fig. 3.33, both curves stabilize near zero, indicating effective learning and minimal over-fitting.

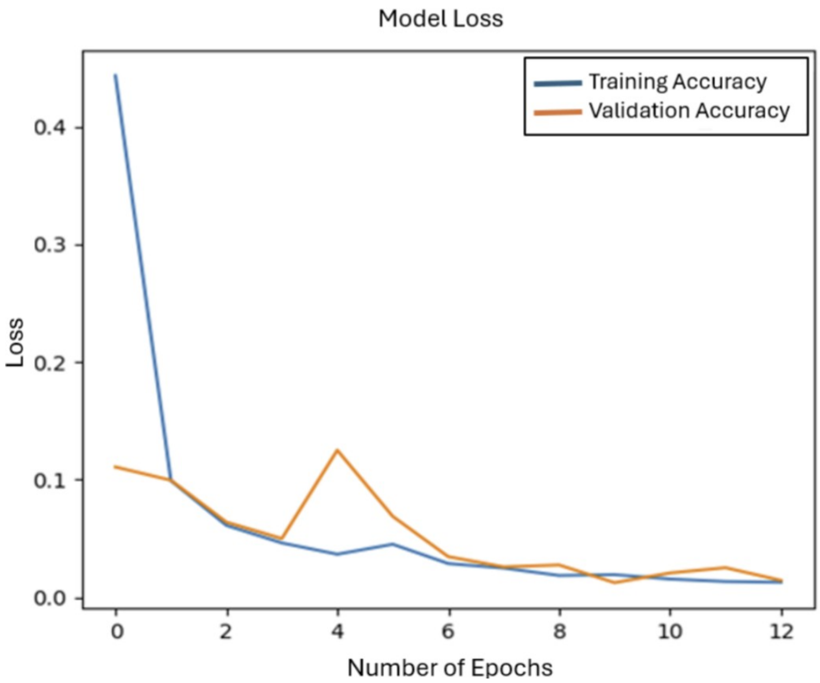

Fig. 3.33 ML Model Training and Validation Loss.

Due to the early stopping employed, the model stopped at 12 epochs for both model's accuracy and loss. ML testing results for classes' classification is presented by the confusion matrix shown in Fig. 3.34.

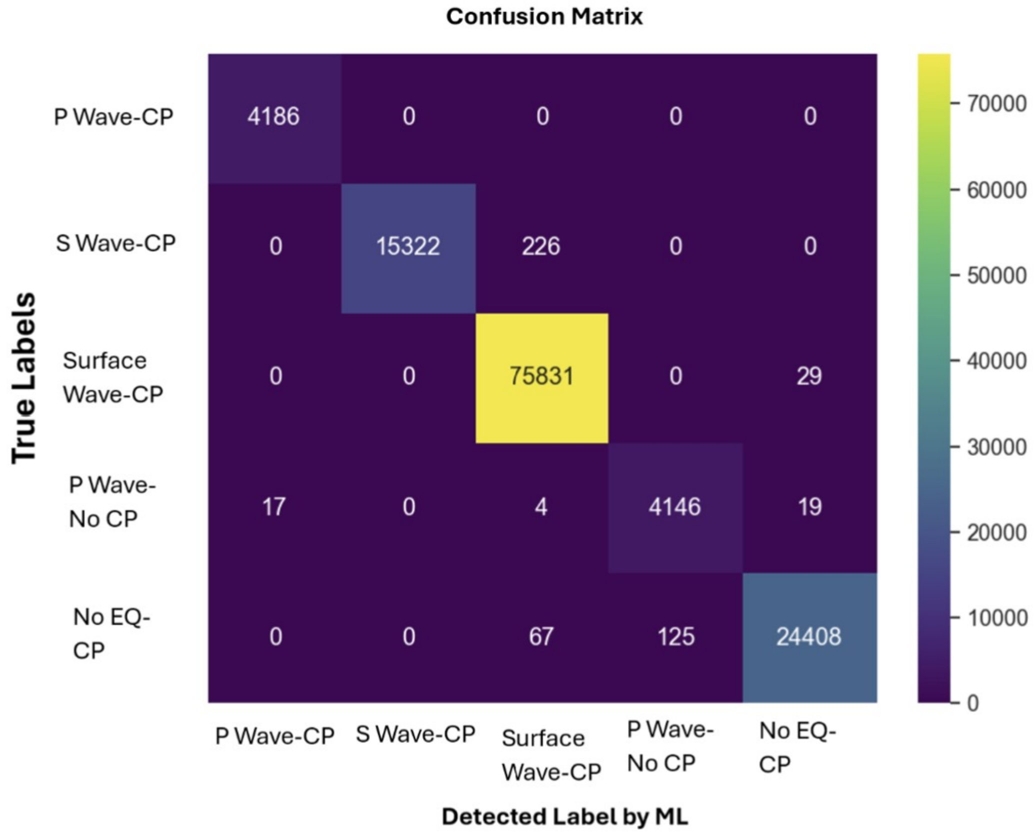

Fig. 3.34 Confusion Matrix.

For P wave-CP class, the model shows 4186 out of 4186 correct detection. For P Wave-NoCP, the model shows 4146 correct detection, 17 wrong detected as Pwave-CP, 4 wrong detected as Surface Wave-CP and 19 wrong detected as No EQ-CP. Similarly with the same concept for No EQ-CP. The model shows 99% of accuracy rate in distinguishing between both events (P Wave-NoCP and No EQ-CP) and in detecting the primary wave in a noisy environment (Pwave-CP), giving the opportunity for an early warning before the destructive surface wave struck. Furthermore, Fig. 3.35 shows the performance of our model in detecting all events. The blue lines represent SOPAS data samples generated after incorporating the additive strain of car passage and seismic activity, while the red dashed lines show the model's detection for all events The red dashed lines align with the SOPAS data's fluctuations, indicating where the model has identify each class of events. This visual representation is consistent with the findings from the confusion matrix. This chapter presents an accurate early earthquake detection mimicing real-world conditions. The promising results of our ML approach indicate the potential to exploit the entire existing traffic-carrying optical networks for the simultaneous sensing of various environmental events.

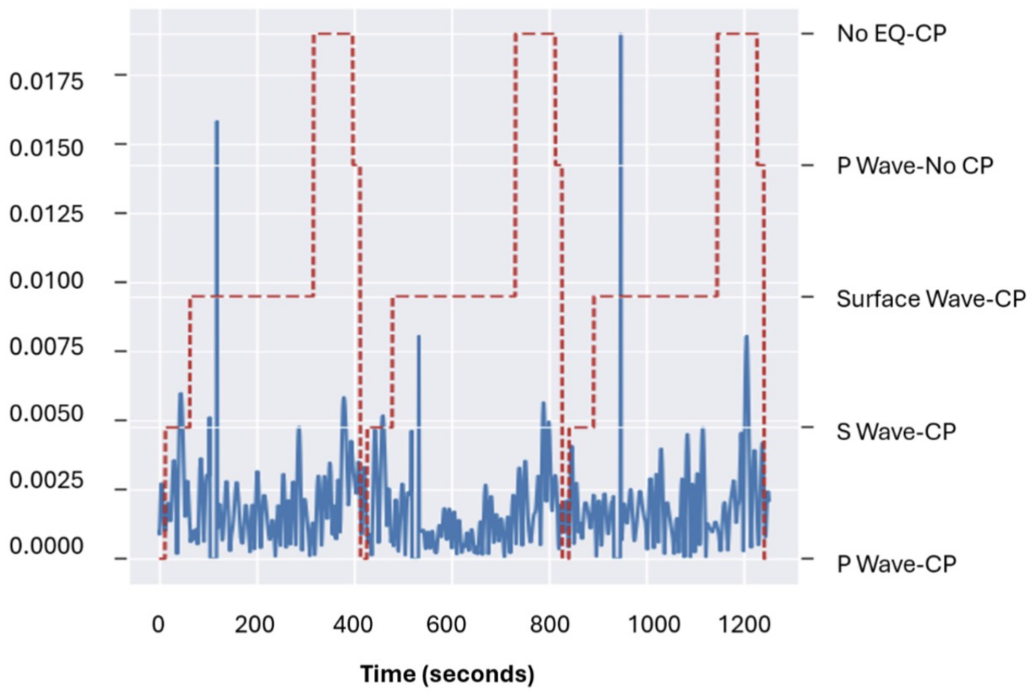

Fig. 3.35 ML Model's Detection on SOPAS Data Sample

3.4 Experimentally Driven Insights

In this part, we extends the concept from simulation to experimental and in-field validation over an operational network, aiming to further assess the ML model's performance on propagated light, under real network conditions, after emulating the polarization stokes evolution induced by the same M4.3 earthquake in a controlled laboratory environment. This study integrates, for the first time, a low-cost, easy deployable sensing card that is directly interfacing with WDM transceiver, capable of capturing polarization data while storing only a few kilobits per event. This enables validation of the ML model's ability to still detect the P-wave arrival from the captured emulated polarization evolution despite propagation challenges, establishing a pathway toward large-scale integration of intelligent fiber-sensing infrastructures. In a lab-based experiment, we replicate the dynamics of the M4.3 Modena earthquake by emulating the SoP evolution data induced by the earthquake's ground displacement values, simulated by the Waveplate model. This setup involves using a WDM card equipped with an IM-DD SFP+ transceiver module generating a 10 Gbps optical signal carrying data, and a commercial Reconfigurable Optical Add-Drop Multiplexer (ROADM) with and embedded Erbium-Doped Fiber Amplifier (EDFA) and Dense WDM (DWDM) filter used as pre-amplifier. The experiment also utilizes an optical scrambler and a polarimeter. The optical scrambler consists of seven waveplates, each with a random polarization axis orientation.

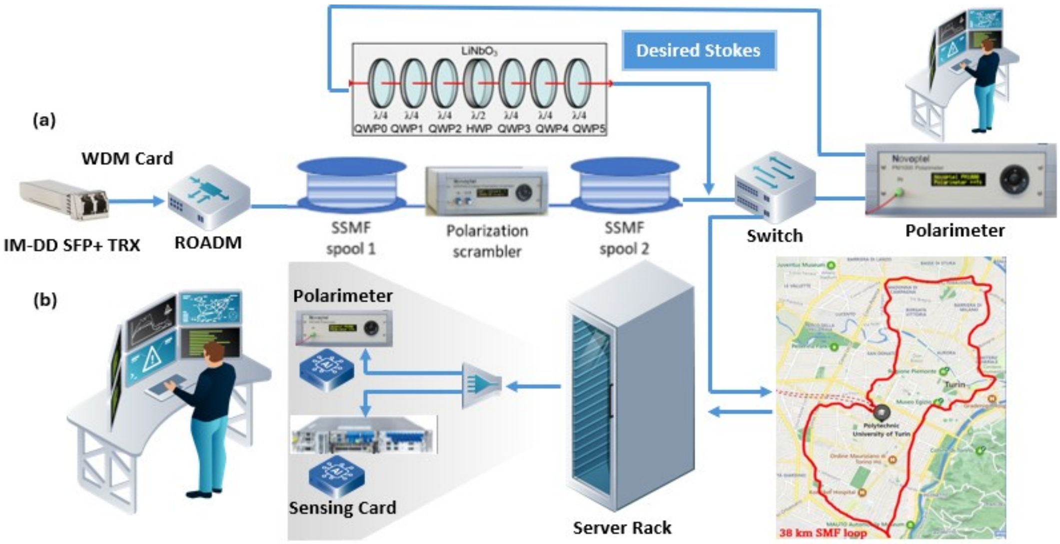

Fig. 3.36 Laboratory and field testing setup for SOP emulation and network validation.(a) Controlled laboratory configuration used to emulate the dynamics of the M4.3 Modena earthquake. The system comprises a WDM card equipped with an IM-DD SFP+ transceiver generating a 10 Gbps optical signal, an optical polarization scrambler composed of seven waveplates with voltage-controlled orientations, and a polarimeter providing feedback for Stokes parameter alignment. (b) Field deployment of the setup through a 38 km fiber ring. At the receiver side, a 10/90 optical splitter drops a small portion of the received optical power (–20 dBm) for monitoring by a polarimeter and a sensing card compatible with WDM systems, enabling polarization tracking to assess real network conditions.

These orientations are adjusted according to the voltages applied to each plate to match the desired SoP, which is initially provided to the scrambler. The scrambled signal is then captured by a polarimeter that quantifies the deviation between the measured and desired stokes through a feedback loop. The optical scrambler then iteratively updates the plates' orientations by applying a minimization algorithm to gradually align the output stokes with the target. This configuration is referred to as the Back-to-Back configuration (B2B) demonstrated in (a) of Fig. 3.36. After replicating the earthquake dynamics, we propagated the targeted stokes through a 38 km single-mode fiber loop deployed in Turin, Italy. At the receiver side, a small portion of the received optical power (-20dbm) is dropped by means of a 10/90 optical splitter and collected by a polarimeter to monitor stokes parameters alterations, and a sensing card compatible with existing WDM networks. Unlike the polarimeter output, the card's output consists of measuring the power differences along polarization components over time.

3.4.1 Polarimeter Based Detection

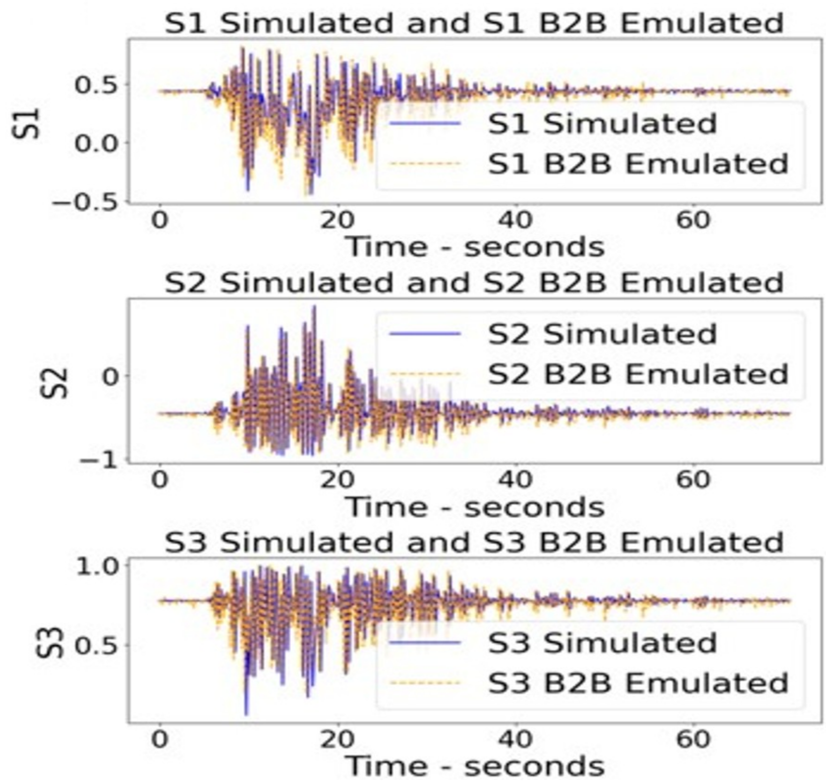

Fig. 3.37 Comparison between simulated and B2B Stokes parameter evolutions. Simulated (blue) and B2B emulated (orange) Stokes components show near-identical temporal profiles.

The B2B emulated stokes (Orange traces) are nearly superimposed the simulated stokes (blue traces) generated previously by the Waveplate framework, indicating excellent temporal and amplitude agreement as shown in Fig. 3.37. This validates that the emulation process is accurate confirming the optical scrambler's capability of reproducing the dynamic SoP variations induced by the Modena M4.3 earthquake's ground displacement values. Minor deviations are attributed to experimental noise, but despite this error, the two signals still exhibit a strong correlation and alignment.

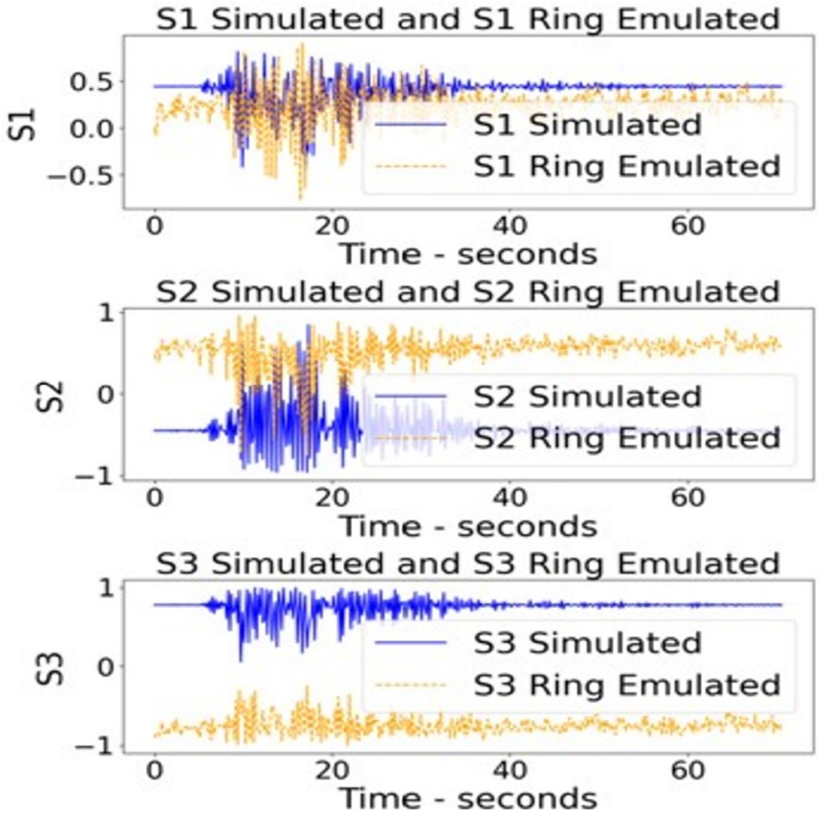

Fig. 3.38 Comparison between simulated and B2B Stokes parameter evolutions. After 38 km ring propagation, the emulated signals preserve the main polarization dynamics despite fiber-induced distortions.

In contrast, after propagating the B2B signal through the 38 km SMF loop, the orange traces (propagated B2B) show broader fluctuations and distortion compared to the simulated ones as demonstarated in Fig. 3.38. This is due to fiber birefringence, polarization-mode dispersion, and amplified spontaneous emission noise. To check if the overall waveform shape and phase transitions remain consistent with the simulated traces and that the signal still hold the polarization signatures despite propagation challenges and impairments, we plot the SOPAS for both. The SOPAS metric proves that the temporal alignment and relative amplitude trends between the simulated and B2B propagated remain preserved, especially during the P-wave time window Fig. 3.39. This confirm that despite optical propagation the polarization dynamics still hold the earthquake's ground displacement information.

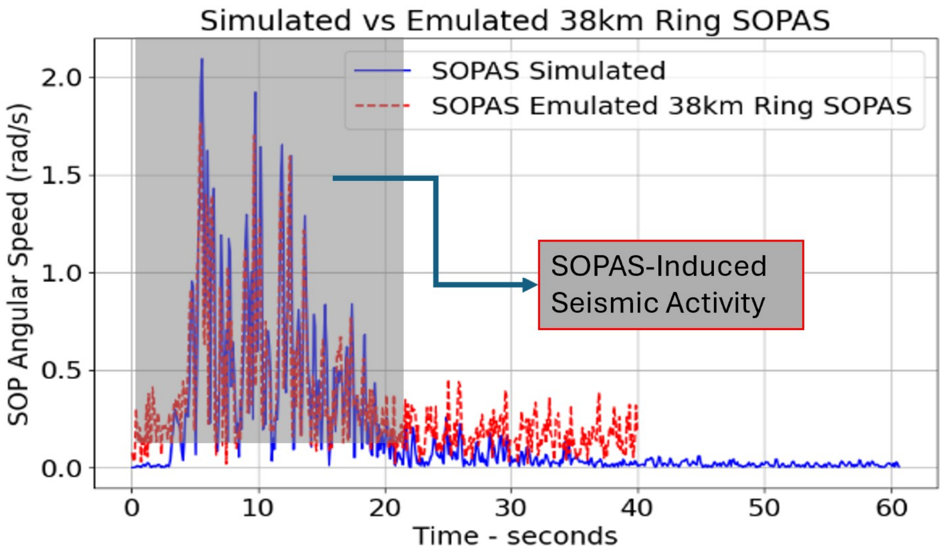

Fig. 3.39 Simulated and B2B propagated SOPAS evolution Comparison.

The ML framework proposed to this work involves using LSTM on B2B emulated data. Furthermore, it involves utilizing LSTM and GRU models separately on propagated emulated stokes captured by the polarimeter, enabling a comparative evaluation of their individual detection accuracy performance. Both models are trained using the adaptive learning rate optimization technique (Adam), which adjusts the learning rate for each parameter based on approximations of the first and second moments of the gradients. Training is done using the sparse categorical cross-entropy loss function, specified as follows:

$$\text{Sparse Categorical Crossentropy}\left(y_{\text{true}}, y_{\text{pred}}\right) = -\frac{1}{N}\sum_{i=1}^{N}\log\left(y_{\text{pred}}^{(i)}\left[y_{\text{true}}^{(i)}\right]\right), \tag{3.13}$$

where:

- N is the total number of samples in the dataset.
- $y_{\text{true}}^{(i)}$ represents the true label for the i^{th} sample, expressed as an integer index corresponding to the correct class.
- $y_{\text{pred}}^{(i)}$ is the predicted probability distribution over all classes for the i^{th} sample.
- The term $\log\left(y_{\text{pred}}^{(i)}[y_{\text{true}}^{(i)}]\right)$ computes the logarithm of the predicted probability assigned to the true class for each sample, contributing to the overall loss.

Initially, we configure the number of epochs to 100 with a batch size of 32 and implement early stopping to further reduce the risk of overfitting.

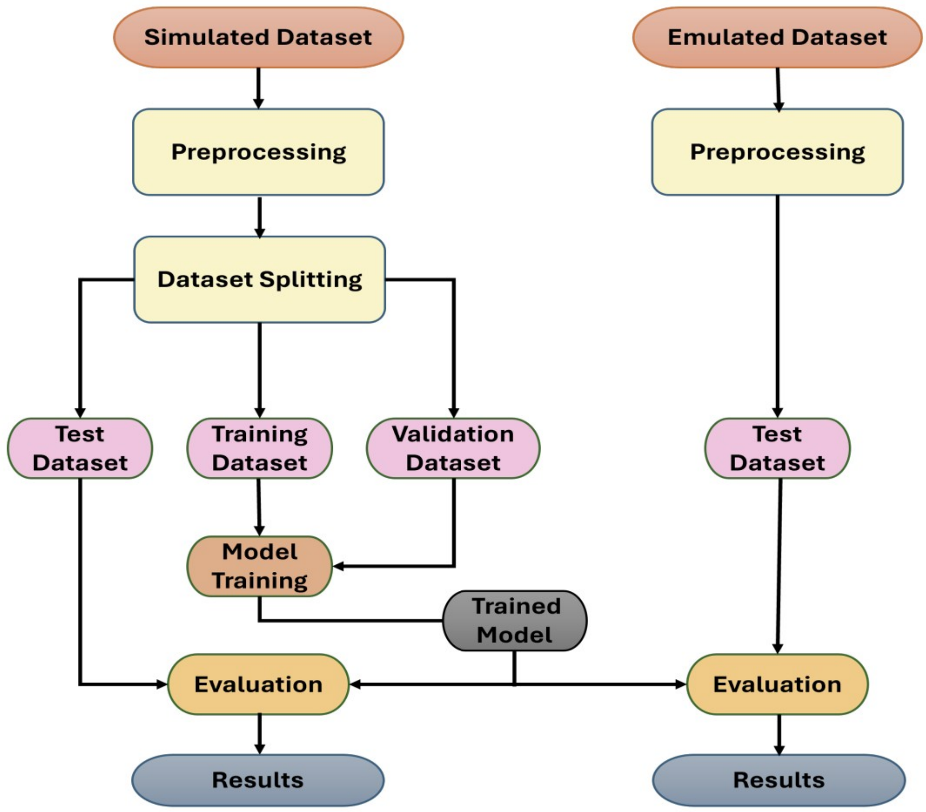

Fig. 3.40 Flow Diagram for ML Models Training, Validation and Testing.

Both models are trained on a simulated dataset comprising 210,000 samples, using a learning rate of 0.0001. For the training process, 60% of this dataset is allocated for model training, while 20% is reserved for validation and the remaining 20% for testing. The flow chart of our ML models' training, validation and testing is depicted in Fig. 3.40. After evaluating the models on the 20% testing portion of the simulated dataset, we then assess their performance on an additional emulated dataset of 19,950 samples collected from our Polarimeter-detection laboratory setup. To evaluate the performance of our proposed models, we utilize accuracy, precision, recall, and F1 score metrics for four classes: No Earthquake, P-Wave, S-Wave, and Surface Waves. The LSTM model achieved a recall of 98.94%, meaning that it correctly identified 98.94% of all actual P-waves in the dataset. There were some instances where the model missed P-waves, misclassify them as No EQ or other classes, which led to a slight decrease in recall. The GRU model achieved a recall of 99.04%, which is higher than the LSTM model's recall. This indicates that the GRU model performs better at detecting true P-waves, even in cases of complex overlapping seismic events. The detailed evaluation of precision, recall, and F1-score for both models is provided in Table 3.2.

Table 3.2 Performance comparison of LSTM and GRU approaches on the emulated dataset

Model	**Parameters count**	**Training time (hours)**	**Prediction time (seconds)**	**Accuracy**	**Precision**	**Recall**	**F1 Score**
LSTM	198,404	6.7	109	98.93%	98.25%	98.94%	98.58%
GRU	149,828	3.1	88	99.17%	98.55%	99.04%	98.79%

The LSTM model were first applied to the B2B emulated dataset, enabling the assessment of the model's performance on the aforementioned set in comparison to the simulated one. The confusion matrices in Fig. 3.41 illustrate the model's high accuracy in detecting different seismic waves. For the simulated data, 2143 correct P-wave detections out of 2156, with 5 wrongly detected as "No Earthquake" and 8 wrongly detected as Secondary wave or "S-wave".

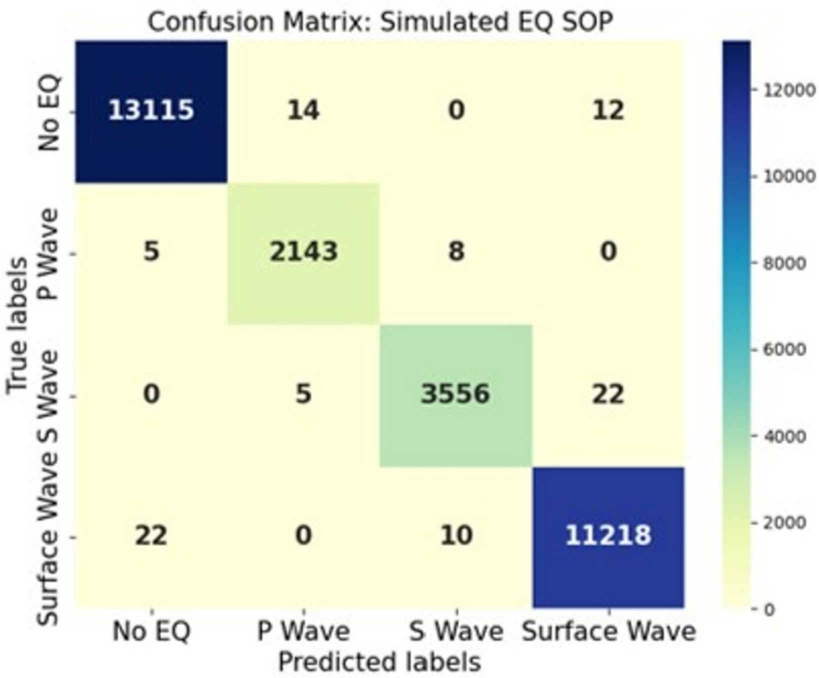

Fig. 3.41 Confusion Matrix for Simulated Data

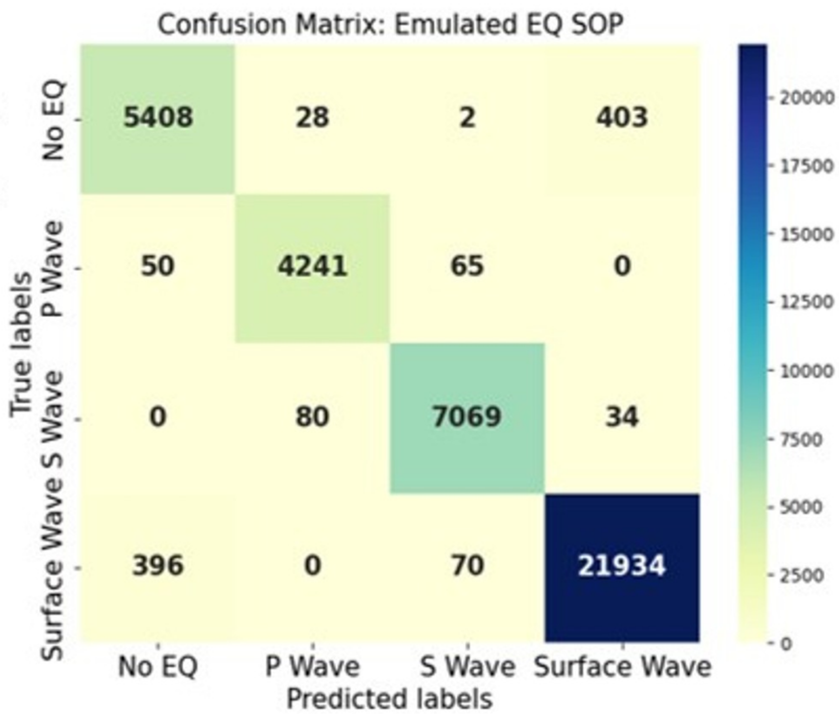

Fig. 3.42 Confusion Matrix for Emulated Data

In contrast for the emulated data in Fig. 3.42, 4241 correct P-wave detections were achieved for the emulated data out of 4356. Similarly, for other wave detections. These results demonstrate 99% of accuracy rate in detecting different waves for the simulated dataset, while the model achieved 97% for the emulated data.

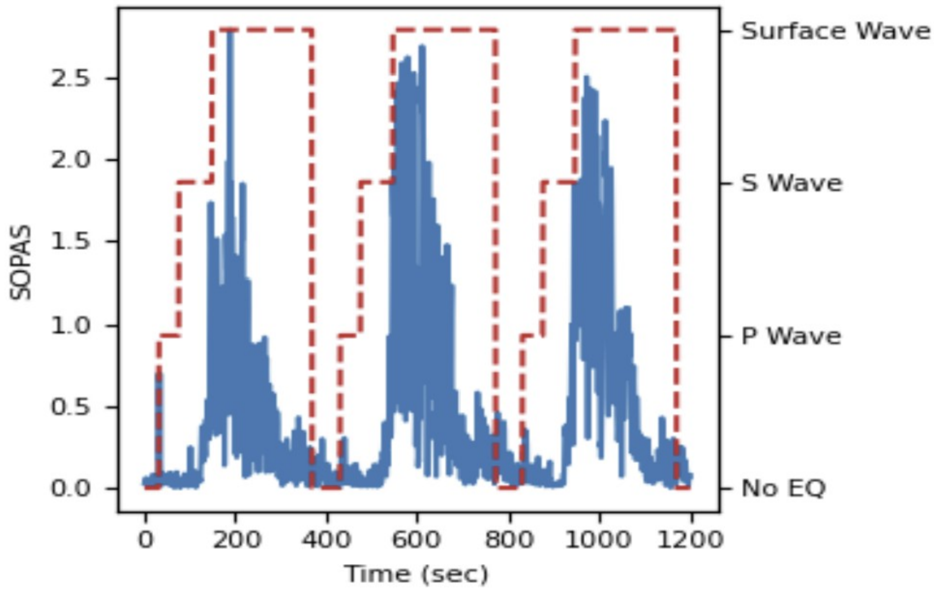

Fig. 3.43 LSTM Predictions on Emulated Dataset

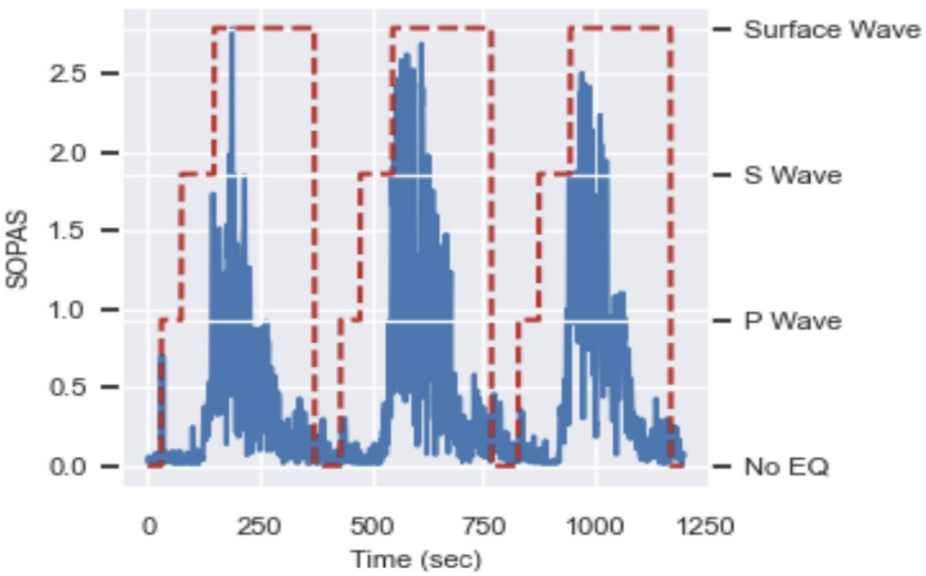

Fig. 3.44 GRU Predictions on Emulated Dataset

Furthermore, the machine learning detection time remains consistent at one second for both datasets, ensuring real-time applicability of the approach. To go further, we intended to compare between LSTM and GRU models on the propagated emulated B2B stokes. In Fig. 3.43 and Fig. 3.44, we demonstrate the prediction graphs for LSTM and GRU models respectively, where blue lines represent the SoP signal and the red dashed lines represent the model's predictions for earthquake waves. LSTM provides reasonably good predictions. Furthermore, the confusion matrices of both models presented in Fig. 3.45 and Fig. 3.46, reveals that the LSTM model's accuracy is 98.93%, with correct classification of 22,047 Surface Waves and 7,012 S Waves.

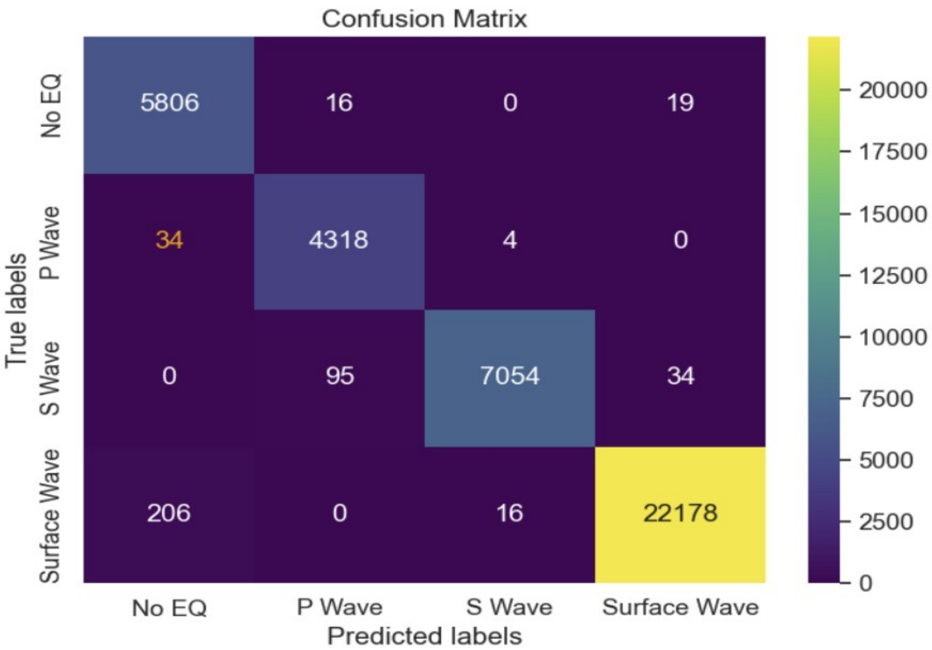

Fig. 3.45 LSTM Confusion Matrix on Emulated Dataset

However, it misclassified some P-Waves as No EQ, which slightly affected its recall for this particular class. The LSTM model's accuracy of 98.93%, with the correct classification of 22,047 Surface Waves and 7,012 S Waves.

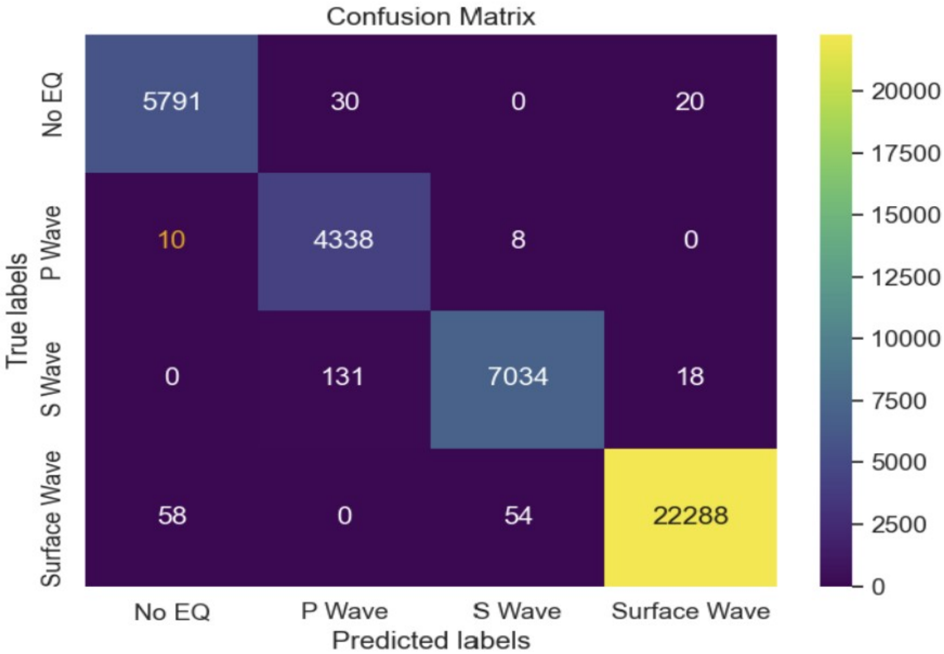

Fig. 3.46 GRU Confusion Matrix on Emulated Dataset

In the contrary, GRU model's prediction graph and confusion matrix demonstrate very good performance. The P-wave class is a critical seismic wave, and its accurate detection and higher recall are essential for timely earthquake detection. The LSTM model achieved a recall of 98.94%, meaning that it correctly identified 98.94% of all actual P-waves in the dataset. There were some instances where the model missed P-waves, misclassify them as No EQ or other classes, which led to a slight decrease in the recall. The GRU model achieved a recall of 99.04%, which is higher than the LSTM model's recall. This indicates that the GRU model performs better at detecting true P-waves, even in cases of complex overlapping seismic events. The GRU confusion matrix demonstrates its superior performance, achieving an accuracy of 99.17%. The GRU correctly classified 22,178 Surface Waves and 7,054 S Waves, with fewer false positives and false negatives than the LSTM. The detailed evaluation of precision, recall, and F1-score for both models is provided in Table 3.2. The computational efficiency of the models is assessed based on the number of parameters, training time, and prediction time (Table 3.2). The GRU model, with 149,828 parameters, required significantly less time for training (3.1 hours) and prediction (88 seconds). Its lower parameter count and faster processing times, combined with its higher performance, make it a more efficient choice for earthquake monitoring. While the LSTM model delivered commendable results, its slightly higher misclassification rate and increased computational demands make it less optimal for real-time earthquake detection. In contrast, the GRU model provides a more efficient and reliable solution for seismic event classification, demonstrating its ability to accurately detect and classify seismic activity with minimal resource usage.

3.4.2 Sensing Card Based Detection

Beyond the deployment in the first setup, SM-OPTICS - the company that co-funded this work - is developed and still developing a sensing card to co-exist with traffic-carrying WDM networks without interfering with communications services. The architecture consists of several key building blocks to enable real-time environmental sensing and event detection. The system involves a powerful microprocessor for algorithm execution, a generator producing the monitored signal, a data sampling system, a database for data storage, a dedicated hardware accelerator for quick and massive data mining, a communication channel for intra-node communication, a communication channel between the Network Management System (NMS) and network elements for sensor coordination, and a north bound interface to interconnect the NMS with external applications. These components collectively create a robust framework for real-time sensing and data processing in optical networks. This system architecture reflects the envisioned future integration within optical networks.

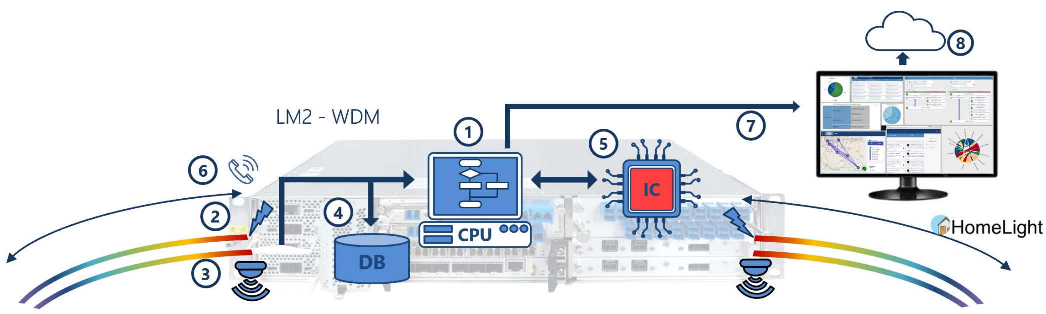

Fig. 3.47 Network architecture demonstrating the card's integration in a WDM system, including signal acquisition, processing, and data transmission to the NMS platform

Fig. 3.47 demonstrates the functional architecture of the sensing system, highlighting the data flow between the card, units and the NMS interfaces. The sensing card, which is a central component of this system, is designed to be installed in optical nodes at the edges of optical links. These optical nodes, equipped with these cards, monitor in real-time the SoP time evolution of a received polarized traffic signal. The sensing cards operate in pass-through mode, allowing the main traffic signal to continue along its optical path without significant interruption or modification, while splitting a small percentage of the signal for measurement. Each card separates the optical signal into two orthogonal polarization components and measures the power levels along the polarization axes at each time instance using two photodiodes. Additionally, each card uses another photodiode to measure the total input power logarithmically as a reference. The acquired data is temporarily stored and periodically transmitted from all cards as demonstrated in Fig. 3.48, to an external server for post-processing. Processed data will be available via the NMS. Post-processing, based on edge computing, detects and classifies different seismic patterns using a pre-trained ML algorithm. In case of seismic activity, multiple nodes enable epicenter localization and correlated measurements to minimize false positive alarms. The sensing infrastructure is managed by the NMS or a domain controller within an SDN architecture, facilitating remote monitoring, configuration, and alarm notification [78].

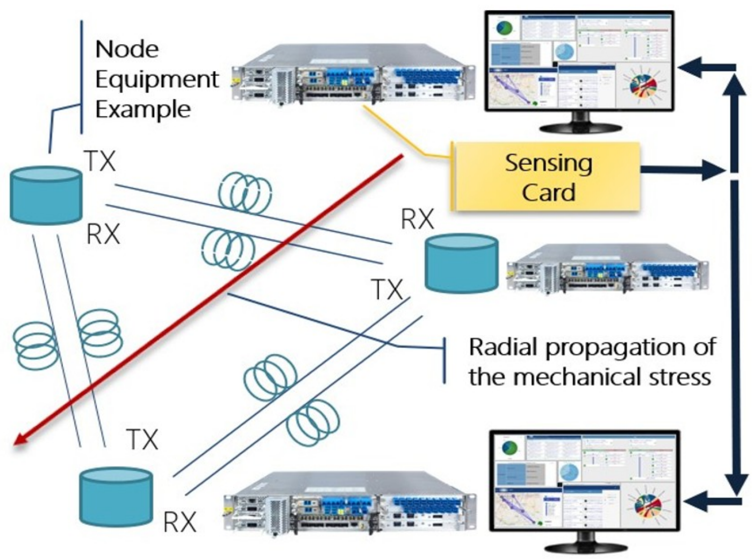

Fig. 3.48 Sensing Card Integration.

Back to the first setup, unlike the polarimeter which provides SoP stokes parameters, the card's output consisted of measuring the power difference levels along polarization components over time. For ML based application and comparison, the card output must aligns with the waveform used to pre-train the model, as power difference levels is not the same as the polarization stokes. For this reason, we derive over time the output power differences from the output captured by the card to get the rate of change. Fig. 3.49 demonstrates an example of comparison between a propagated SOPAS time evolution, recorded by a polarimeter, and the rate of change of power difference over time, captured by the card, highlighting their perfect alignment and high correlation despite propagation challenges. This alignment ensures that the ML model, pre-trained on SOPAS data, can seamlessly adapt to identify alterations in the power difference captured by the sensing card.

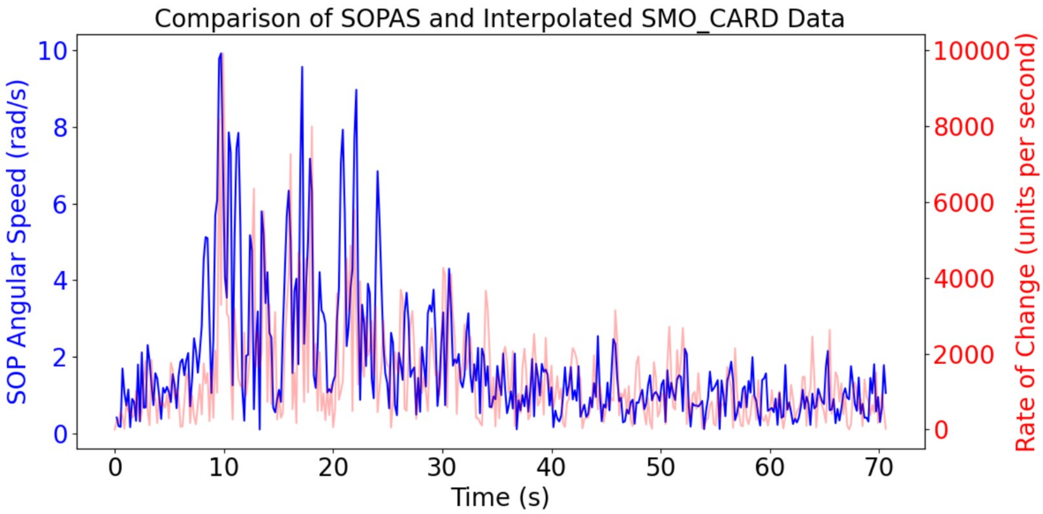

Fig. 3.49 Comparison of SOPAS and Card Rate of Change Data.

Furthermore, it maintains its ability to accurately detect the primary wave, enabling reliable early earthquake detection even when transitioning from SOPAS-based input to power difference data and from computer-based simulations to laboratory-based setup. The ML framework employ the pre-trained and tested LSTM model presented earlier on the simulated data extracted from the Waveplate model. However, here we employ transfer learning on top of the model, utilizing the pre-training on the simulated SOPAS and fine-tuning it on a smaller emulated - propagated B2B SOPAS and SOPAS propagated B2B dataset derived from the card's output dataset. This approach allows the model to adapt to real-world conditions with minimal additional training. Fine-tuning enables the model to adjust to the specific characteristics of the propagated dataset while retaining the knowledge acquired from the larger previous dataset. This transfer learning methodology enhances the model's performance and significantly reduces the reliance on extensive labeled data for training. The transfer learning-approach achieves 98% accuracy, 98% precision, 98% recall and also 98% F1 score in detecting P-wave on the SOPAS propagated B2B dataset. The confusion matrix for SOPAS propagated B2B dataset derived from the card's output is illustrated in Fig. 3.50 demonstrating the model's strong performance in accurately identifying different wave types. Among 1617 primary wave events, the model successfully detected 1578, with only minor errors: 19 instances were mistakenly classified as No Earthquake, and 20 were incorrectly identified as Secondary Waves.

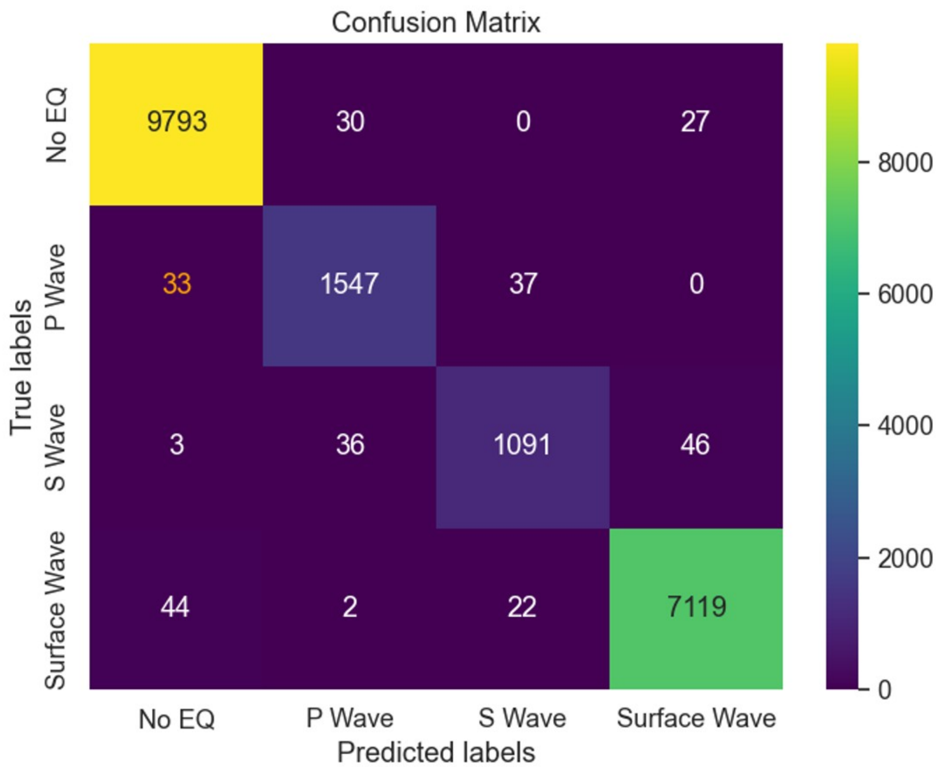

Fig. 3.50 Confusion Matrix for Power Propagated Dataset

Our proposed model achieves 96% accuracy, 96% precision, 96% recall and also 96% F1 score in detecting P-wave on the power difference measurements of the propagated B2B dataset.

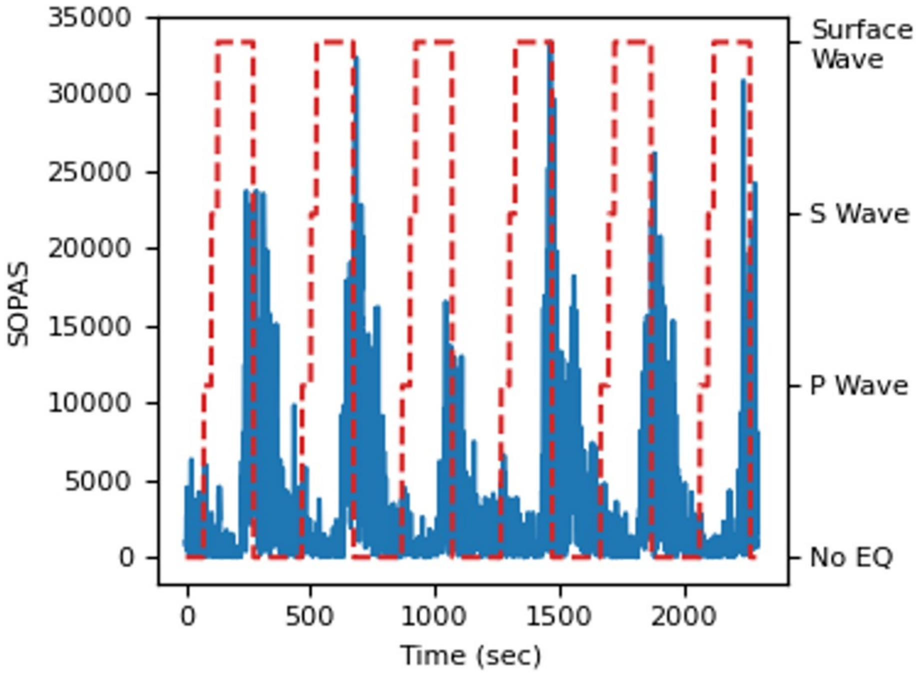

Fig. 3.51 Predictions on Power propagated dataset

Fig. 3.51 further demonstrates the model's ability to detect and classify different seismic waves and show the performance of our model in detecting all events. The blue lines represent the rate of change of power difference measurements, while the red dashed lines indicate the model's classification output for all events, i.e., P-wave, S-wave, Surface Wave, and No EQ. This visual representation is consistent with the findings from the confusion matrix. These results highlight the effectiveness of our transfer learning-based approach, which achieves exceptional performance on the B2B propagated dataset and demonstrates robust adaptability when integrated with the sensing card that captures power difference fluctuations despite propagation challenges.

3.4.3 Car Vehicles and IM-DD Optical channels

The contribution of this part is to experimentally provide a proof of concept of the sensing technique envisioned to be employed in a terrestrial network architecture [79]. In this experiment we prosecute the aforementioned activities, adding the localization capability of external perturbations by leveraging SoP monitoring of an IM-DD optical channel and demonstrating that this technique can be implemented with commercial IM-DD transceivers which simultaneously carry data. Indeed, a couple of IM-DD transceivers and polarimeters or a polarization beam splitter connected by a bidirectional fiber pair is the minimum setup needed to perform detection and localization. The bidirectional setup implemented for the experimental validation of the environmental activity localization is depicted in Fig. 3.52.

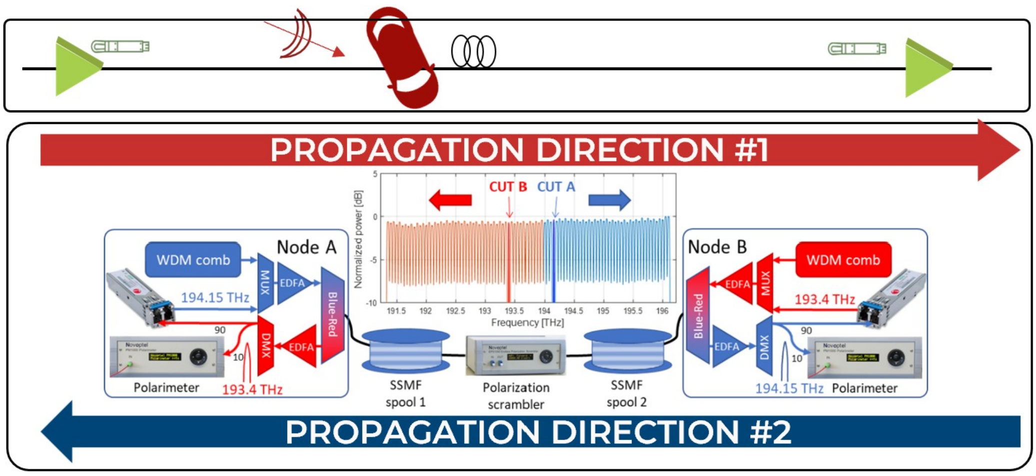

Fig. 3.52 Experimental setup. On both ends an IMDD TRX and a polarimeter are present, being the opposite flows separated with blue/red filters. SSMF: standard single-mode fiber; DMX: demultiplexer; EDFA: erbium-doped fiber amplifier; Blue-Red: multiplexer/demultiplexer.

Each node is composed by a commercial WDM card equipped with an IM-DD SFP+ TRX module generating an intensity modulated optical signal at 10 Gbps carrying data, and a commercial Reconfigurable Add Drop Multiplexer (ROADM) with an embedded Erbuim Dopped Fiber Amplifier (EDFA) and dense DWDM filter used as pre-amplifier and 10 Gbps drop node, respectively. A blue/red filter is placed in front of each node, in order to separate the two bidirectional signals. A small portion of the received optical power (-20 dBm) is dropped by means of a 10/90 optical splitter and collected by a commercial polarimeter (Novoptel PM1000) to monitor the Stokes parameters variations. The bidirectional link is composed of two standard single mode fiber spools with a polarization scrambler (Novoptel EPS1000) between them. This scrambler is programmed to emulate fast Stokes parameters variations, similar to the one caused by the local birefringence modulation induced by vibration/pressure that can be produced by the passage of the front and rear car's axle across high sensitivity points like the mini/micro trenches for fiber cable installation on the roadway as demonstrated in Fig. 3.53 and observed in [80]. The birefringence change induces variations of the Stokes parameters of the IM-DD signals, which can be identified as a peak. The emulated peak propagates towards both nodes, therefore the two polarimeters shall be synchronized in time, in order to share the same time reference during peak detection.

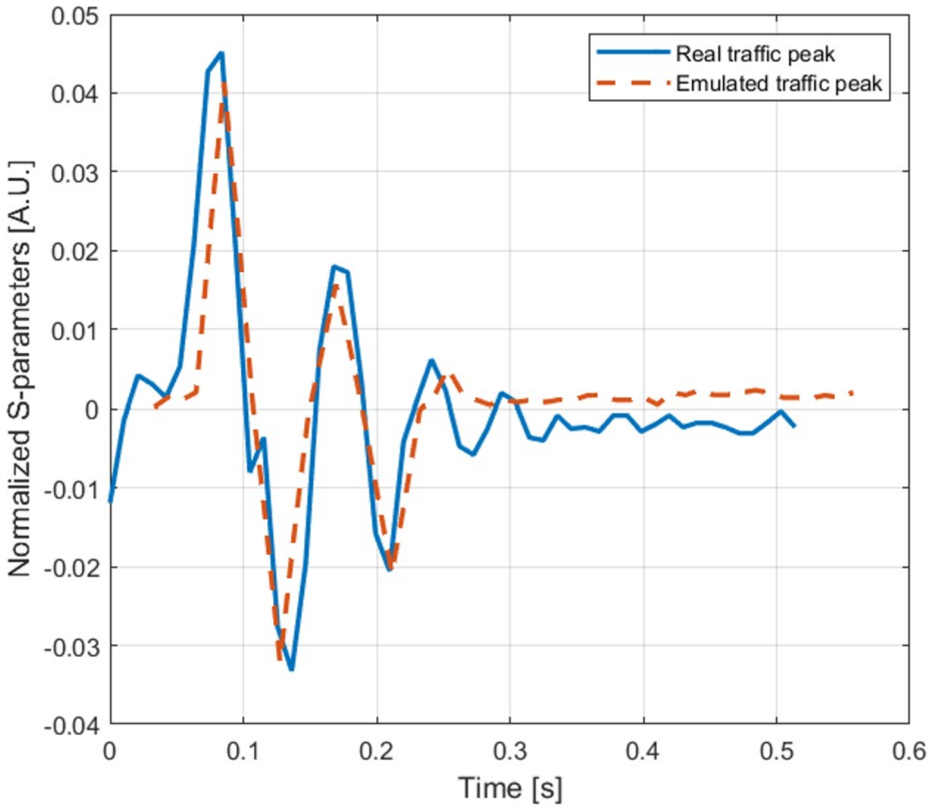

Fig. 3.53 Comparison between Stokes parameters variation over time generated by the real traffic and the laboratory polarization scrambler.

The difference between the two polarimeters timestamps corresponding to the peak detection is then evaluated and translated in spatial difference. The polarimeters sampling rate is set as a trade-off between the maximum number of samples that can be stored and the time resolution that can be achieved; for this experiment, 3.1 MSample/s is used, resulting in a time resolution of about 320 ns, corresponding to a spatial resolution of about 64 m as demonstrated in Fig. 3.54.

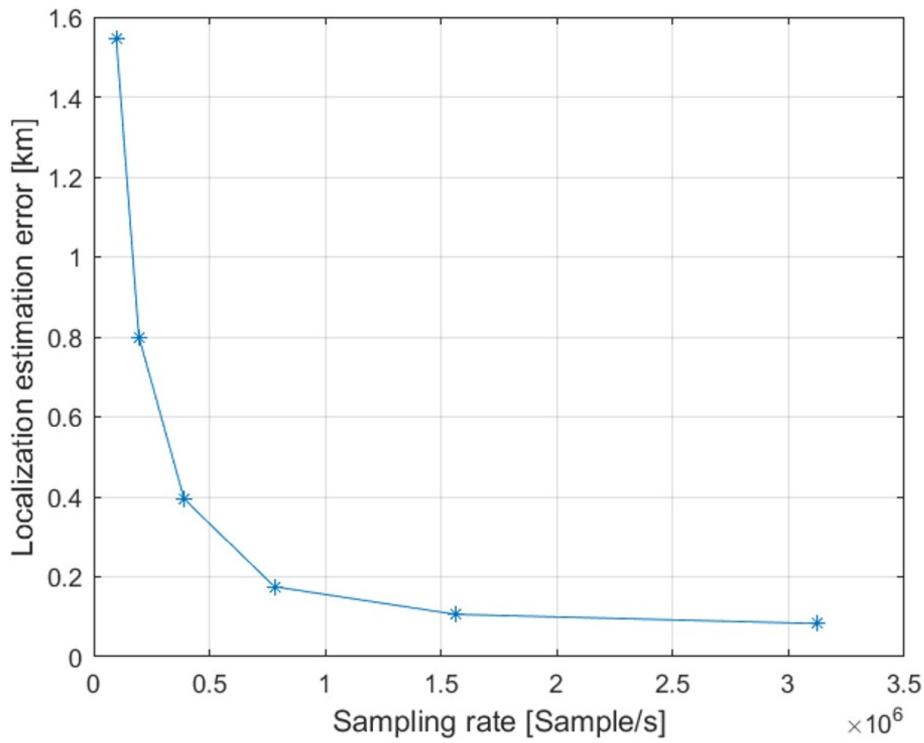

Fig. 3.54 Localization estimation error as a function of the polarimeter's sampling rate.

In order to validate the peak localization method, we used different fiber spools. While the first fiber spool length was kept constant, we varied the second spool length to emulate a mechanical stress happening at seven different positions in the overall fiber length are summarized in Table 3.3. Within each configuration, the event location is fixed and occurs at a consistent time in the recorded traces. A comparison between the Optical Time-Domain Reflectometry (OTDR) and SoP methods measurements show an acceptable accuracy in all the cases. A crucial aspect to take into account is related to the required sampling rate to obtain a certain accuracy, as this impacts the cost and the complexity of the sensing system. We thus focused on the most accurate spool length combination among those presented in Table 3.3, i.e. the 7th with spool 2 of 16.518 km. In this configuration we let the sample rate to vary from 0.1 MSamples/s to 3.1 MSamples/s.

Table 3.3 Experimental results

Test	**Measured with OTDR**		**Localization method**	
	Spool 1(km)	**Spool 2(km)**	**Spool 1(km)**	**Spool 2(km)**
1	20.006	0.957	20.550	0.413
2	20.006	6.045	20.447	5.604
3	20.006	7.002	20.299	6.709
4	20.006	9.515	20.268	9.253
5	20.006	10.437	20.237	10.242
6	20.006	15.560	20.140	15.426
7	20.006	16.518	20.089	16.435

For each sample rate we have calculated the localization estimation error as the difference between the value obtained with the OTDR and the one obtained with the SoPtechnique. The results are reported right of Fig. 3.53, showing that it decreases from around 1.5 km at 0.1 Msamples/s to less than 100 m at 3.1 MSamples/s, although it reaches similar low values at 1.0-1.5 MSamples/s. This result suggests that acceptable estimation errors can be obtained with reasonably low cost/complexity Analog-Digital Converter (ADC) circuits. Moreover, further cost reduction may be gained using a simpler Polarization Beam Splitter-based system to estimate the SoP variation. It is important to note that the generalization of this approach to other configurations may depend on several factors, including measurement noise, hardware constraints, and link directionality.

Chapter 4

In-Field Testing Measurements

This experimental campaign was conducted during a six-month visiting research period at Télécom Paris, Polytechnic Institute of Paris and Orange Innovations in France. The primary goal was to validate polarization-based sensing technology particularly by leveraging the sensing card presented earlier. In-field testing considered to be under realistic conditions, where environmental disturbances and infrastructure constraints are unavoidable. The objective was to detect and characterize seismic-like mechanical impact along an underground dark optical fiber cable deployed in Lannion, France at Orange Innovation's premises. Inaddition to that, we compare the card's response against a reference sensing modal. The setup consists of DAS system, SoP sensing card, an accelerometer, and a load cell.

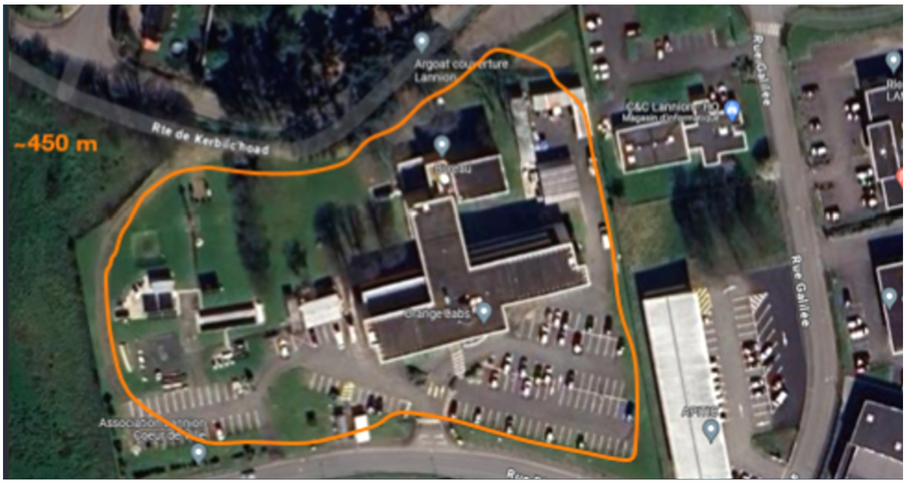

Fig. 4.1 450 meters Underground Deployed Dark Fiber Link

Fig. 4.1 shows the underground 450 meters deployed fiber link, spliced to connect a sensing cabinet on one end and a main fiber cabinet on the other. The spliced connection include approximately 30 meters of aerial and in-cabinet fiber. The setup environment was not fully controlled and was subject to environmental perturbations such as wind, rain, vehicular traffic, and human activities in the vicinity of the fiber infrastructure. Mechanical excitations were generated using a controlled seismic hammer (Load Cell), cable pulling/shaking, and walking in proximity to the fiber cable. The Load cell measurements were simultaneously acquired by the DAS and the SoP systems, while the others only by the SoP. Unavoidable temporal discrepancies were introduced in the joint measurements due to the absence of a common hardware trigger, which control the time synchronization between different acquisition systems. Consequently, we did not succeed to compare between both sensing modalities. It is worth mentioning also that the the wind, heavy rain, and car passage around introduce a high fluctuating behavior when collecting the data on the SoP system, highlighting the challenges to be addressed in terms of the card's sensitivity. The load cell was used to measure directly the timing and the mechanical force exerted by the hammer on the ground, while the accelerometer was leveraged to detect and characterize the strain coupled to the ground and the underground cable, providing information on the temporal occurrence and relative intensity of the induced vibrations within the acquisition window.

4.0.1 Five Meters Steel-Rubber Impact on Grass

The first experiment was conducted to monitor polarization power difference evolution in response to applied seismic hamming mechanical stress in 5 meters proximity to the underground optical fiber path. The impact was generated using steel-to-rubber hammer and applied on a grassy surface. The objective was to emulate a low-frequency, attenuated seismic-like excitation under real world conditions. The accelerometer was placed to touch the deployed cable, measuring strain coupling while the load cell is collecting directly the stress applied to the grass. For future endeavors, one can exploit the presence of the accelerometer and the load cell to develop a full mathematical model, capable of representing the coupling of nanostrain induced by the force in Newton applied in a given distance. This is can be leveraged instead of the i-DAS conventional conversion for a more robust simulations. The first experimental setup is demonstrated in Fig. 4.2.

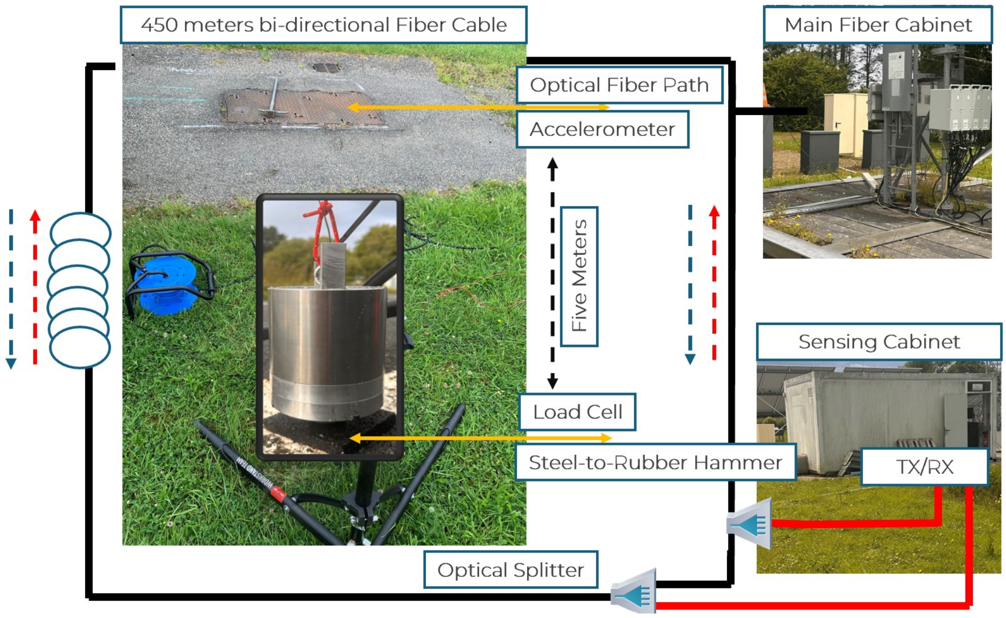

Fig. 4.2 First In-field Test Measurements: The setup involves a sensing card placed inside the sensing cabinet, an in-field load cell, hammer, and an accelerometer.

The in-field measurement involved sending a continuous laser pulse, embedded inside the card to propagate through the deployed cable and split again to collect the temporal evolution.

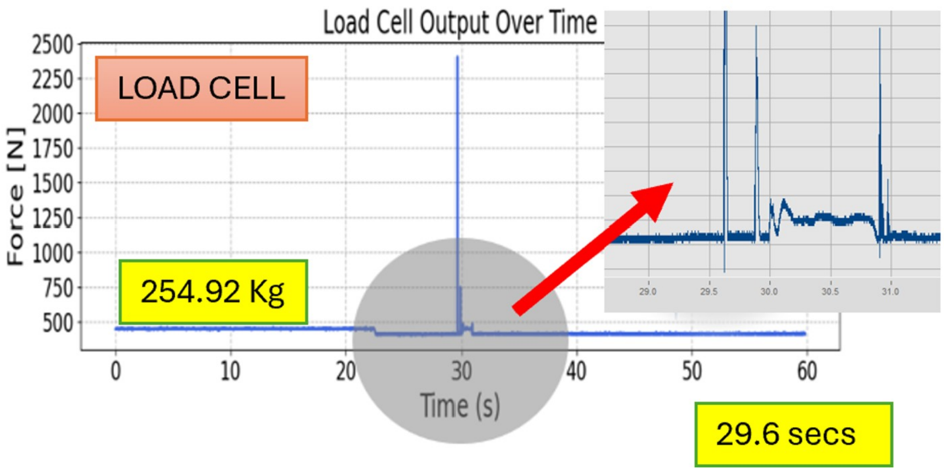

Fig. 4.3 Load Cell Measurements.

The total temporal measurement was during 60 seconds, where the hammer initially scheduled to hit at the 30 seconds. The load cell registered the hammer hit at a force peak of 2445 N, which corresponds to approximately 255 Kilograms, at 29.6 seconds as shown in Fig. 4.3. In contrast, the SoP sensing card response demonstrated in Fig. 4.4, detected a corresponding polarization response peak at approximately 27.6 seconds, resulting in time discrepancy of approximately two seconds.

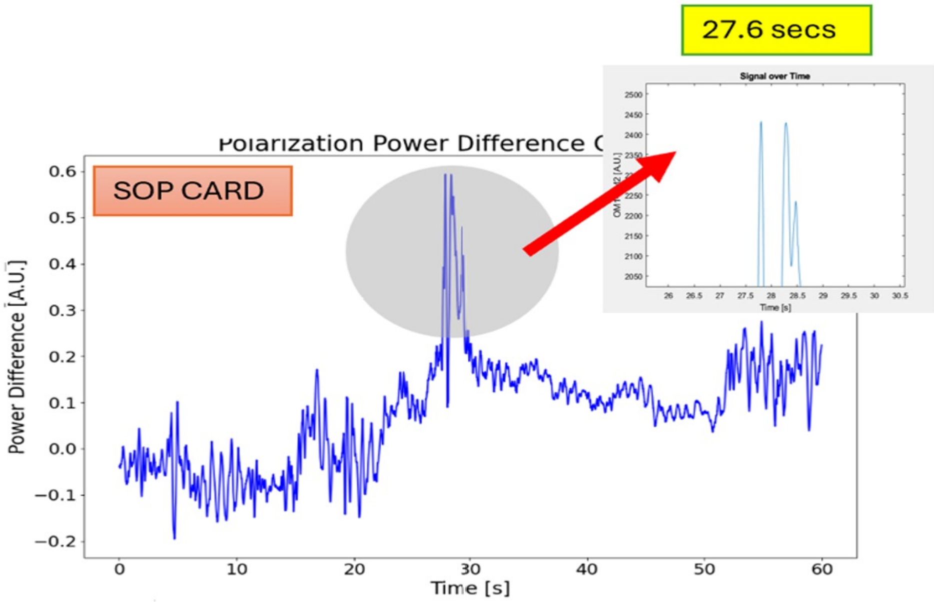

Fig. 4.4 SOP Sensing Card Response.

This misalignment in time was expected, particularly due to the absence of a common trigger system between the load cell and the SoP system. The timing delay could also be introduced by the load cell acquisition software, as it may be recording the folder creation time but not the actual seismic hit. This uncontrolled timing setup prevent an exact temporal alignment between the two measurement systems. Despite this discrepancy, the sensing card still exhibit a clear response to the applied impact, with a 0,6 magnitude in normalized stokes corresponding to the 2445 N. Moreover, the derivative of the normalized signal emphasized the aforementioned as demonstrated in Fig. 4.5, revealing a sharp and well-defined peak at the event time and effectively highlighting the impulsive excitation nature.

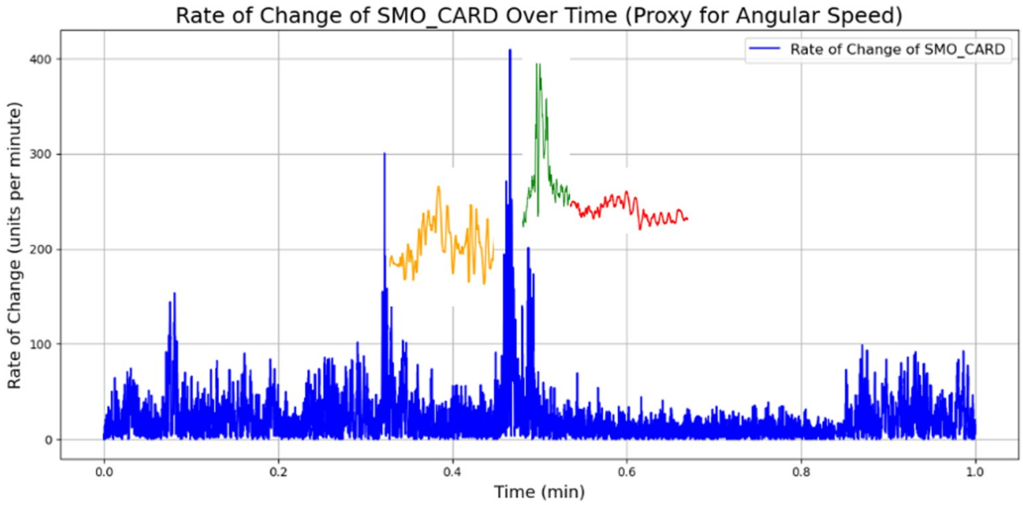

Fig. 4.5 SOP Sensing Card Power Differences derivative.

4.0.2 One Meter Steel-Steel Impact on Concrete

The second experiment was designed to assess the sensing card to assess to shorter distance and lower mechanical forces applied by the impact. It is worth mentioning here that the mechanical-fiber coupling decreases as the impact force decreases, inducing a more challenging scenario in terms of card sensitivity.

Fig. 4.6 Steel-to-Steel Concrete Test: One Meter from the Fiber Path.

Almost exact environmental conditions were surrounding the event, as the first experiment, including the absence of common trigger for time synchronization. In this configuration, the mechanical impact was generated using steel-to-steel seismic hammer applied on concrete surface instead of grassy surface, and located one meter from the optical fiber path as demonstrated in Fig. 4.6. Two hammer hits were applied under almost identical experimental conditions within the same acquisition window. We intended to hit the impact with different forces, where the first impact occurred at around 22 seconds with a peak force of 350 N (35 kilograms) and the seconds hit at around 41 seconds with a peak force of 500 N (50 kilograms). The reference measurements obtained from the load cell is demonstrated Fig. 4.7.

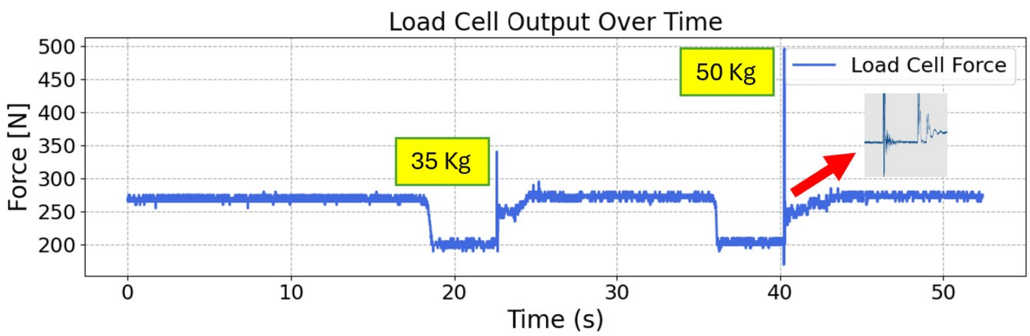

Fig. 4.7 Load Cell Measurements

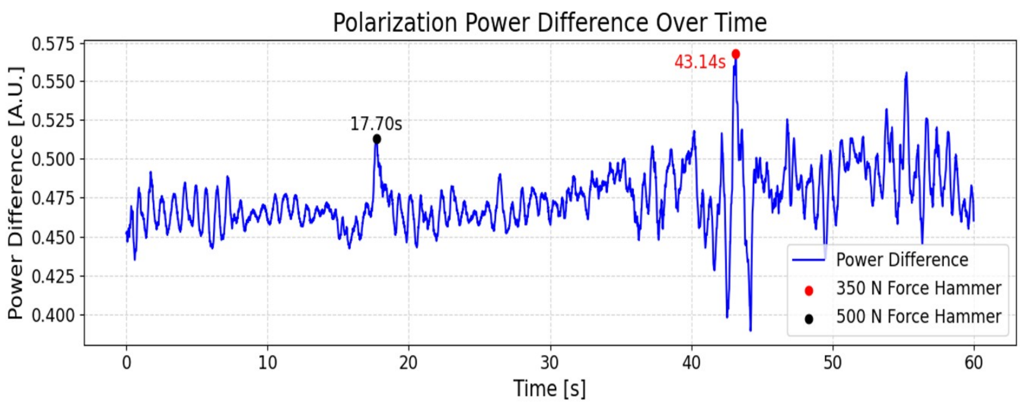

Fig. 4.8 Sensing Card Response

Despite the ambient noise and surrounding environment, the sensing card detected clear response corresponding to the impact at approximately 43 seconds, consistent with a two seconds temporal offset, similar to that obtained in the first experiment. The acquisition window was set to be 60 seconds. The corresponding normalized stokes depicted in Fig. 4.8, exhibited a two other peak values at 17.70 seconds and another one at around 55 seconds. These two peaks may be due to the aerial and in-cabinet part of the setup connection, particularly in the presence of high wind and bad weather conditions. The analysis of the temporal derivative shown in Fig. 4.9, of the power difference captured by the card supports this interpretation, as a clear spike was observed at around 0.7 which corresponds to a similar timing (around 43 seconds) observed at a 60 seconds time axis.

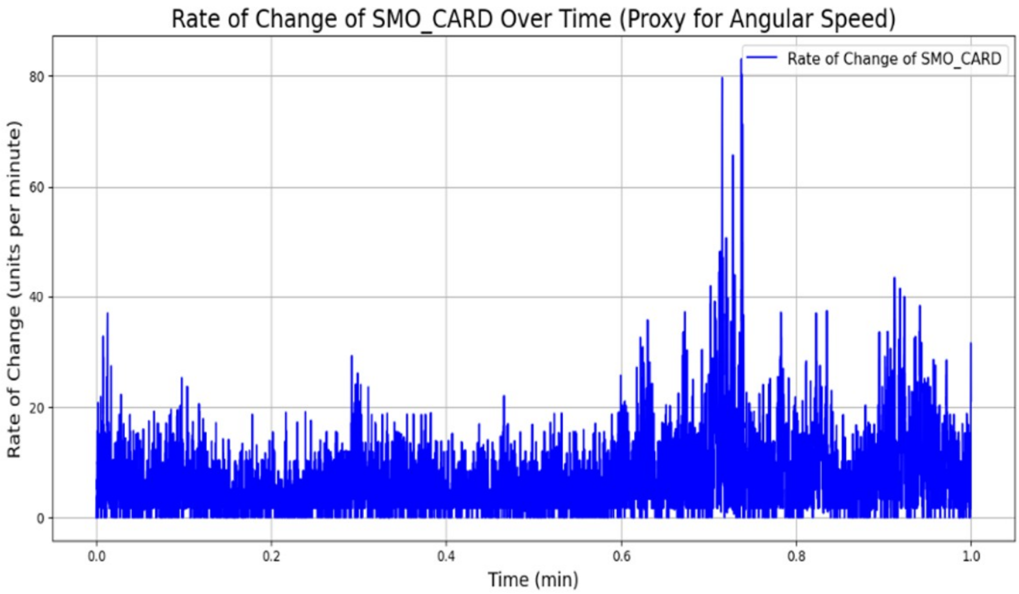

Fig. 4.9 Sensing Card Output Temporal Derivative.

However, the spectral analysis further indicates that the frequency components associated for each event (the one considered to corresponds to 350 N, 500 N, the suspicious third peak, and a time window from 5 to 15 seconds to pick up noise frequency). All frequencies were concentrated in the low-frequency range (0 to 2 Hz) as demonstrated in Fig. 4.10, introducing challenging filtering to pick the right peak for the event.Spectral analysis further indicates that the frequency components associated with the detected event, as well as those associated with noise and spurious peaks, are concentrated in the low-frequency range between 0 and 2 Hz.

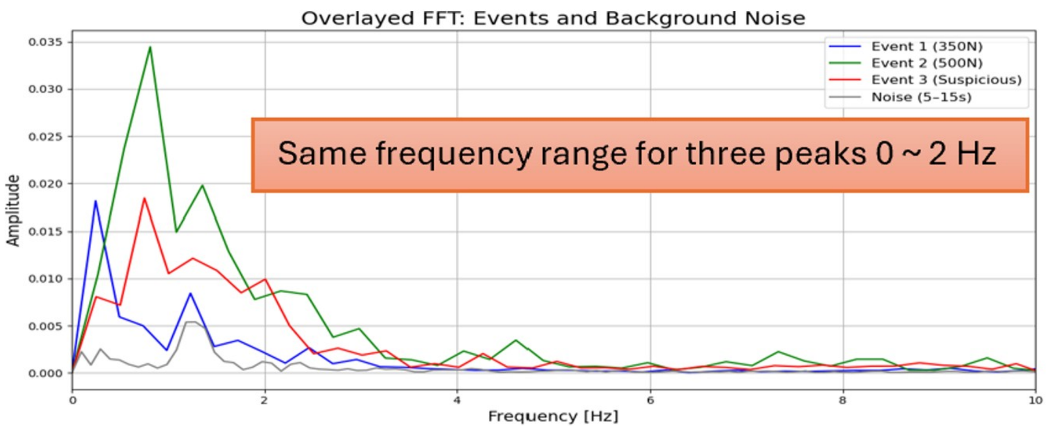

Fig. 4.10 Fourier Transform of the Original Signal to pick up the Dominant Frequencies.

Factors like unstable weather conditions, ambient noise, and the absence of a common trigger contributed in the sensing signal response. In addition, card's sensitivity could be the issue, particularly since this card is still in its first development phase, indicating that low forces impact applied such as, 35 kilograms, can not be detected by the card. Thereby, further testing with a more controlled setup is needed in order to assess the card's performance.

4.0.3 In-Cabinet and Technical Chamber Disturbances

In addition to the mechanical excitation applied by the hammer, we intended to apply a set of controlled operational disturbances corresponding to different types of events and observe the sensing card response. These tests were conducted underground in the technical chamber where the optical fiber path and in proximity to the outdoor cable connecting the sensing cabinet to the main fiber cabinet. The objective of these experiments is to pave to way to exploit this sensing technique in security application, for instance: a theft trying to shake or pull the underground cable passing through the technical chamber. Cable shaking and cable pulling were performed manually by inducing oscillatory movement to the fiber cable, while cable pulling consisted of applying a tensile force along the cable axis. The technical chamber is shown in Fig. 4.11.

Fig. 4.11 Underground Technical Chamber

While the sensing card response to shaking and pulling the fiber segment is depicted in Fig. 4.12 and Fig. 4.13 respectively.

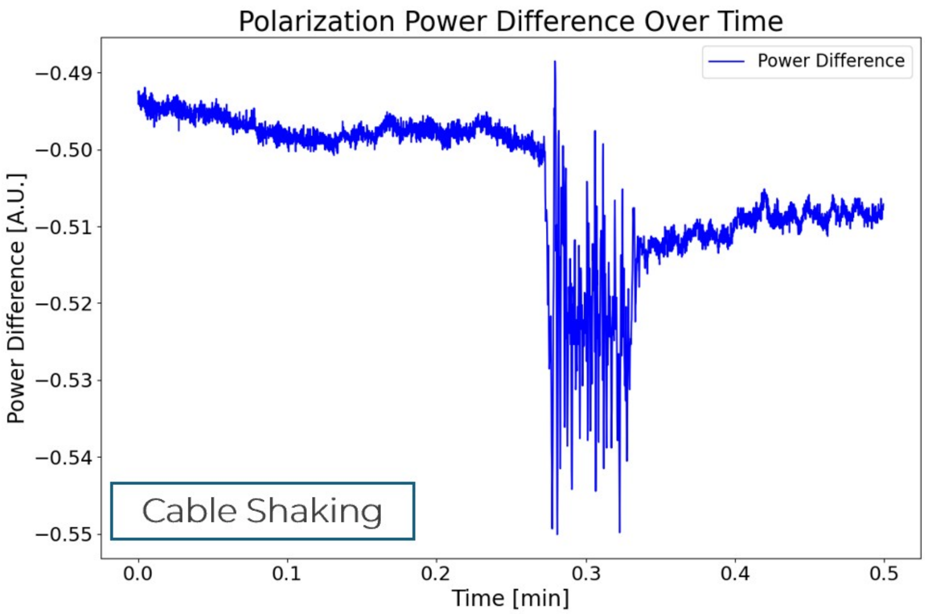

Fig. 4.12 The Sensing Card Response to the Excited Fiber Cable: Fiber Cable Shaking

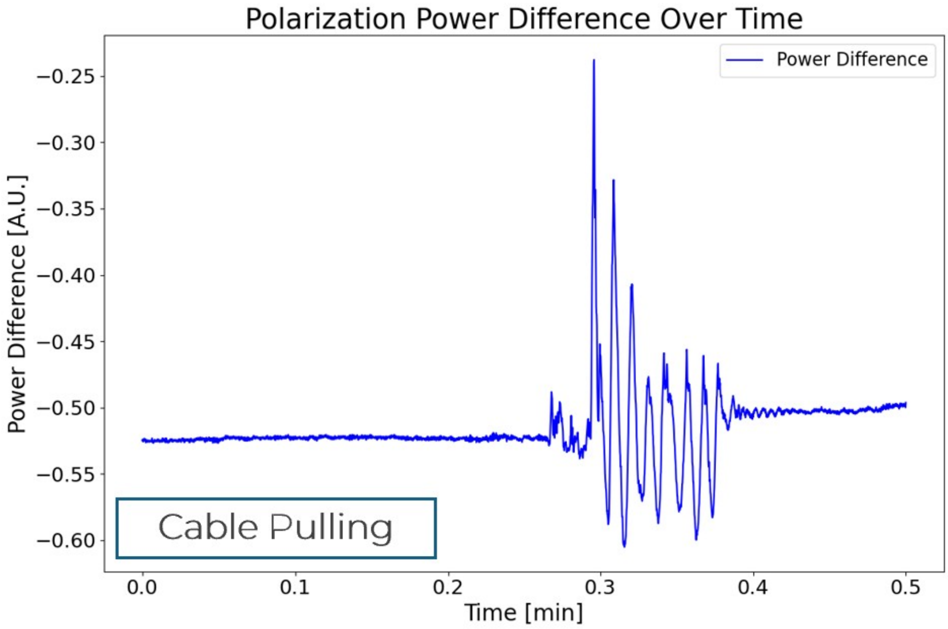

Fig. 4.13 The Sensing Card Response to the Excited Fiber Cable: Fiber Cable Pulling

The sensing card recorded clear polarization power difference fluctuations in response to both shaking and pulling the cable, reflecting the events' continuous mechanical nature.

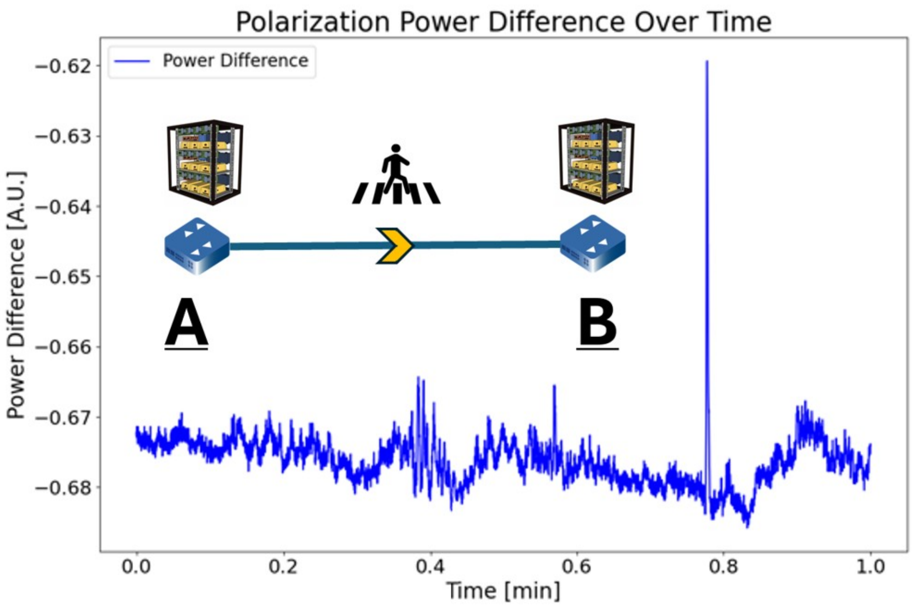

Fig. 4.14 Sensing Card Response to Walking in Proximity to the Fiber Cable

In contrast, walking in proximity to the outdoor cable connecting the sensing cabinet to the main fiber cabinet recorded a clear spike response recorded by the card as demonstrated in Fig. 4.14. These results demonstrate the ability of polarization sensing card in detecting different types of manually applied external events. The main objective of this chapter was to showcase the real utilization of the first version of the developed sensing card, instead of focusing on ML modals. However, pre-trained ML modals can be leveraged in the edge computing or even external AI agents concepts to define, detect, and localize an external events and distinguish it from ambient noise or another external event.

Chapter 5

Future Perpectives and Conclusion

5.0.1 Future Perspectives - Quantum Sensing

Classical optical fiber sensing is limited by the Shot Noise Limit (SNL), where classical sensing can only detect external events occurring above SNL. The photons of the light injected into the fiber cable arrives randomly, which creates the so-called "Shot Noise". By integrating quantum mechanical principles into classical sensing architecture (Interferometric, DAS, or SoP-based), the effective measurement noise can be reduced, thereby enhancing fiber sensitivity. Quantum resources such as (Quantum entanglement, quantum coherence, and squeezed states), allows the quantum-enhanced sensing system to detect disturbances below SNL, such as weak magnetic field [81], gravitational wave [82, 83], and small electric charges [84]. Quantum-enhanced sensing systems achieve the aforementioned by engineering the statistical properties of the probing light injected into the fiber cable instead of modifying the physical sensing mechanism itself. The quantum squeezed states of light enables redistribution of measurement uncertainty, significantly reducing the noise in the observable of interest (phase difference in interferometric techniques, phase or intensity fluctuations in DAS, and polarization in SoP-based mechanisms)[85]. Entangled photons can share correlated fluctuations on both ends, thereby the common noise cancels out, while quantum coherence preserves light properties throughout propagation. In a nutshell, classical sensing can be considered as a noisy room, whereas quantum sensing, the noise is pushed to the corners or cancels out. Optical fibers represent a great medium to implement quantum-enhanced sensing systems on the top, as these systems can serve as a complementary extension to classical fiber sensing infrastructure.

5.0.2 Conclusion

To manage the challenges of swiftly evolving traffic patterns, optical networks are evolving towards dynamically re-configurable, autonomous systems. These systems are managed by a centralized Optical Network Controller, which interacts with Network Elements by means of Application Programming Interfaces. The controller leverages various metrics tracked by each network elements, constituting the streaming telemetry paradigm for network management purposes. This setup facilitates the provision of varied services to the higher network layers. The streaming telemetry paradigm entails continuous data transmission from network elements to the network controller, enabling network management and control. Devices like Re-Configurable Add/Drop Multiplexers and amplifiers include crucial information like power levels and variations in temperature, whereas devices like coherent transceivers capture alterations in phase and polarization of optical signals. External stress affects the latter metrics, allowing environment-aware optical networks that can be leveraged in early warning system and environmental surveillance. These metrics can be monitored by external sensing systems, however, some are complex to implement and suffer from greater limitations than others. Artificial intelligence, in particular ML models based on RNN can help in learning time-series pattern of collected metrics changes to detect and localize external disturbances. The selected architecture is motivated by its ability to capture temporal dependencies in SoP signals. Physics-Informed Neural Networks (PINNs) could also be relevant to solve this problem, and a comprehensive comparison between them is left for future work. In this thesis, We showcase a polarization-based sensing system meant to be employed in existing traffic-carrying optical terrestrial networks. This thesis supports the vision of smart cities, AI initiatives, and environment-aware optical networks that can be re-purposed for early disaster warning, infrastructure protection, human activity monitoring, and security-relevant applications, without the need for additional field sensors.

Acronyms

ADAM Adaptive Learning Rate Optimizer. 36

ADC Analog-Digital Converter. 76

AI Artificial Intelligence. 6–8, 12, 13, 17, 22, 28, 87, 89

ANN Artificial Neural Network. 22

API Application Programming Interface. 7

BOTDA Brillouin Optical-Time Domain Analysis. 19

CD Chromatic Dispersion. 9

CNN Convolutional Neural Network. 22

DAS Distributed Acoustic Sensing. 13, 14, 19, 28, 30, 32, 45, 49, 51, 77, 78, 88

DFOS Distributed Fiber Optics Sensing. 2, 5, 13–17

DGD Differential Group Delay. 27

DSP Digital Signal Processing. 9, 10, 13, 14, 18

DSS Distributed Strain Sensing. 13, 14

DTS Distributed Temperature Sensing. 13, 14

DVS Distributed Vibration Sensing. 13, 14

DWDM Dense Wavelength Division Multiplexing. 14, 15, 73

EDFA Erbuim Dopped Fiber Amplifier. 73

EEWS Earthquake Early Warning System. 4

GAN Generative Adversarial Network. 22

GRU Gated Recurrent Neural Network. 24, 61, 63, 66–68

I In-phase. 9–11

IBN Intent-Based Networking. 6, 8

IEC International Electrotechnical Commission. 14

IM-DD Intensity Modulated - Direct Detected. 5, 6, 8, 9, 13, 14, 18, 58, 73, 74

IMT International Mobile Telecommunications. 17

INGV Italian National Institute of Geophysics and Volcanology. 33, 34, 37, 42, 45, 49

ISAAC Integrated Sensing and Communication. 17

ITU-R International Telecommunication Union's Radiocommunication. 17

ITU-T International Telecommunication Union Telecommunication. 13, 15, 17

LSTM Long Short - Term Memory. 23, 24, 37, 53, 54, 61, 63, 66–68, 70

ML Machine Learning. 6, 7, 16, 22, 24, 28, 32, 37–39, 42, 44, 45, 53, 55, 57, 61, 63, 70, 87, 89

MLP Multi-Layer Perceptron. 22

MUX/DEMUX Multiplexer/Demultiplexer. 15

NE Network Element. 15

NMS Network Management System. 68, 69

OAM Operations, Administration, and Maintenance. 17

ODN Optical Distribution Network. 16, 18

OLT Optical Line Terminal. 16

ONU Optical Network Unit. 16, 18

OOK On-Off-Keying. 9

OSNR Optical Signal-to-Noise Ratio. 15

OTDR Optical Time Domain Reflectometer. 75, 76

PAM4 Pulse Amplitude Modulation. 9

PBS Polarization Beam Splitter. 18

PMD Polarization Mode Dispersion. 9

PON Passive Optical Network. 16, 18

PSE Polarization Sensing Element. 18

Q Quadrature. 9–11

QOT Quality of Transmission. 6, 8, 22

RNN Recurrent Neural Network. 22, 36, 89

ROADM Reconfigurable Add Drop Multiplexer. 73

ROTDR Raman Optical-Time Domain Reflectometry. 19

RSA Rounting and Spectrum Assignment. 7, 8

SDN Software-Defined Networking. 6–9, 12, 69

SEAFOM Fiber Optic Monitoring in Subsea Applications. 14

SNL Shot Noise Limit. 88

SoP State-of-Polarization. 9, 11, 12, 18, 19, 23, 25, 26, 28, 30–32, 35, 37, 45, 58, 60, 66, 69, 70, 73, 75–78, 80, 88, 89

SOPAS State of Polarization Angular Speed. 28, 35, 37, 38, 42, 44, 46, 51–54, 56, 61, 70, 71

TCN Temporal Convolution Network. 37

TFAN Temporal Fusion Attention Network. 37, 39, 46, 48

VAE Variational Autoencoder. 22

XPM Cross-Phase Modulation. 15

References

[1] K. C. Kao and G. A. Hockham. "Dielectric-fibre surface waveguides for optical frequencies". In: *Proc. Inst. Electr. Eng.* 113.7 (1966), pp. 1151–1158. DOI: 10.1049/piee.1966.0189.

[2] P. Boffi. *Sensing Applications in Deployed Telecommunication Fiber Infrastructures*. Paper presented at the European Conference on Optical Communication (ECOC 2022), Basel, Switzerland, 18–22 September 2022; Optica Publishing Group Technical Digest, paper Mo4A.4. 2022.

[3] Grand View Research. "Distributed fiber optic sensor market size, share & trends analysis report by application, by technology (rayleigh Effect, brillouin scattering), By vertical (oil & gas, power & utility), by region, and segment forecasts, 2024 - 2030". In: *www.grandviewresearch.com/industry-analysis/distributed-fiber-optic-sensor-sensing-dfos-market.[Last Accessed: November 12, 2025]* (2025).

[4] M. He, S. Ren, and Z. Tao. "Cross-fault Newton force measurement for Earthquake prediction". In: *Rock Mechanics Bulletin* 1.1 (2022), p. 100006. DOI: https://doi.org/10.1016/j.rockmb.2022.100006.

[5] W. Lin et al. "Stress State in the Largest Displacement Area of the 2011 Tohoku-Oki Earthquake". In: *Science* 339.6120 (2013), pp. 687–690. DOI: https://doi.org/10.1126/science.1229379.

[6] S. Hickman and M. Zoback. "Stress orientations and magnitudes in the SAFOD pilot hole". In: *Advanced Earth and Space Sciences* 31.15 (2004), L15S12. DOI: https://doi.org/10.1029/2004GL020043.

[7] H. Ishii and Y. Asai. "Development of a borehole stress meter for studying earthquake predictions and rock mechanics, and stress seismograms of

the 2011 Tohoku earthquake (M 9.0)”. In: *Earth Planet and Space* 67.26 (2015), pp. 1–15. DOI: https://doi.org/10.1186/s40623-015-0197-z.

[8] M. Gladwin. “High-precision multicomponent borehole deformation monitoring”. In: *American Institute of Physics* 55 (1984), pp. 2011–2016. DOI: https://doi.org/10.1063/1.1137704.

[9] M. Wu, C.Zhang, and T. Fan. “Stress state of the Baoxing segment of the southwestern Longmenshan Fault Zone before and after the Ms 7.0 Lushan earthquake”. In: *Journal of Asian Earth Sciences* 121 (2016), pp. 9–19. DOI: https://doi.org/10.1016/j.jseaes.2016.02.004.

[10] X. Jinlai and X. Zhaohua. “Infrasound waves caused by earthquake on 12 July 1993 in Japan”. In: *Acta Acustica* 21.1 (1996), pp. 55–61. DOI: https://doi.org/10.15949/j.cnki.0371-0025.1996.01.008.

[11] R. Allen and H. Kanamori. “The Potential for Earthquake Early Warning in Southern California”. In: *Science* 300.5620 (2003), pp. 786–789. DOI: https://doi.org/10.1126/science.1080912.

[12] R. Geller et al. “Earthquakes Cannot Be Predicted”. In: *Science* 275.5306 (1997), p. 1616. DOI: https://doi.org/10.1126/science.275.5306.1616.

[13] S. Yamamoto and M. Tomori. “Earthquake early warning system for railways and its performance”. In: *Journal of JSCE* 1 (2013), pp. 322–328. DOI: https://doi.org/10.2208/journalofjsce.1.1_322.

[14] M. R. Fernandez-Ruiz et al. “Distributed acoustic sensing for seismic activity monitoring”. In: *APL Photonics* 5.3 (2020), p. 030901. DOI: https://doi.org/10.1063/1.5139602.

[15] B. Shin, D. Zhang, and B. Wang. “Distributed optical fiber monitoring technologies of geological and geotechnical engineering and its development”. In: *Journal of Engineering Geology* 15.S2 (2007), pp. 109–116.

[16] A. Leivadeas and M. Falkner. “A survey on intent-based networking”. In: *IEEE Communications Surveys & Tutorials* 25.1 (2023), pp. 625–655. DOI: https://doi.org/10.1109/COMST.2022.3215919.

[17] A. Clemm et al. “Intent-Based Networking – Concepts and Definitions”. In: 9315 (2022), pp. 1–23. DOI: https://doi.org/10.17487/RFC9315.

[18] F. Musumeci et al. “An overview on application of machine learning techniques in optical network”. In: *IEEE Communications Surveys & Tutorials* 21.2 (2019), pp. 1383–1408. DOI: https://doi.org/10.1109/COMST.2018.2880039.

[19] J. Zhensheng et al. “Digital coherent transmission for next-generation cable operators’ optical access networks”. In: *SCTE/ISBE and NCTA* (2017), pp. 1–43.

[20] D. Che and X. Chen. “Modulation format and digital signal processing for IM-DD optics at post-200G era”. In: *Journal of Lightwave Technology* 42.2 (2024), pp. 588–605. DOI: https://doi.org/10.1109/JLT.2023.3311716.

[21] P. Castoldi et al. “Shaping the future of optical networks by integrating SDN, telemetry, and AI [Invited]”. In: *Journal of Optical Communications and Networking* 17.7 (2025), pp. C51–C61. DOI: https://doi.org/10.1364/JOCN.553843.

[22] N. Morette et al. “On the robustness of a ML-based method for QoT tool parameter refinement in partially loaded networks”. In: *Optical Fiber Communication Conference (OFC)*. Optica Publishing Group. 2022, pp. 1–3.

[23] M. Ionescu, A. Ghazisaeidi, and J. Renaudier. “Machine learning assisted hybrid EDFA-raman amplifier design for C+L bands”. In: *European Conference on Optical Communications (ECOC)*. VDE Verlag / VDE ITG. 2022, pp. 1–3.

[24] B. Shariati et al. “Learning from the optical spectrum: failure detection and identification”. In: *Journal of Lightwave Technology* 37.2 (2019), pp. 433–440. DOI: https://doi.org/10.1109/JLT.2018.2859199.

[25] T. Anderson et al. “Multi impairment monitoring for optical networks”. In: *Journal of Lightwave Technology* 27.16 (2009), pp. 3729–3736. DOI: https://doi.org/10.1109/JLT.2009.2025052.

[26] J. Babbar et al. “Machine learning models for alarm classification and failure localization in optical transport networks”. In: *Journal of Optical Communications and Networking* 14.8 (2022), pp. 621–628. DOI: https://doi.org/10.1364/JOCN.457687.

[27] D. Maillot-Tchofo et al. "Clustering of live network alarms using unsupervised statistical models". In: *European Conference on Optical Communications (ECOC).* VDE Verlag / VDE ITG. 2023, pp. 1246–1249.

[28] L. Velasco et al. "Intent-based networking and its application to optical networks [Invited Tutorial]". In: *Journal of Optical Communications and Networking* 14.1 (2022), A11–A22. DOI: https://doi.org/10.1364/JOCN.438255.

[29] P. D. Hernández, J. A. Ramírez, and M. A. Soto. "Deep-learning-based earthquake detection for fiber-optic distributed acoustic sensing". In: *Journal of Lightwave Technology* 40.8 (2022), pp. 2639–2650. DOI: https://doi.org/10.1109/JLT.2021.3138724.

[30] W. Yiming, P. Mugen, and L. Yaqiong. "Intent-based networks for 6G: Insights and challenges". In: *Digital Communications and Networks* 6.3 (2020), pp. 270–280. DOI: https://doi.org/10.1016/j.dcan.2020.07.001.

[31] Zhensheng. Jia et al. "Digital coherent transmission for next-generation cable operators' optical access networks". In: *NCTA Technical Papers.* CableLabs. 2017, pp. 1–43.

[32] X. Liu. "Evolution of fiber-optic transmission and networking toward the 5G era". In: *iScience* 22 (2019), pp. 489–506. DOI: https://doi.org/10.1016/j.isci.2019.11.026.

[33] R. Nagarajan, I. yubomirsky, and O. Agazzi. "Low power DSP-Based transceivers for data center optical fiber communicationss". In: *Journal of Lightwave Technology* 39.16 (2021), pp. 5221–5231. DOI: https://doi.org/10.1109/JLT.2021.3089901.

[34] K. Kikuchi. "Fundamentals of coherent optical fiber communications". In: *Journal of Lightwave Technology* 34.1 (2016), pp. 157–179. DOI: https://doi.org/10.1109/JLT.2015.2463719.

[35] E. Collet. *Field guide to polarization.* SPIE, 2005.

[36] W. H. McMaster. "Polarization and the stokes parameters". In: *American Journal of Physics* 22.6 (1954), pp. 351–362. DOI: https://doi.org/10.1119/1.1933744.

[37] J. Liu et al. “Urban sensing using existing fiber-optic networks”. In: *Natural Gas Science and Eng.* 16.1 (Nature Communications), pp. 1–10. DOI: https://doi.org/10.1038/s41467-025-57997-y.

[38] F. Tanimola and D. Hill. “Distributed fibre optic sensors for pipeline protection”. In: *Natural Gas Science and Eng.* 1.4 (2009), pp. 134–143. DOI: https://doi.org/10.1016/j.jngse.2009.08.002.

[39] Z. He et al. “Fiber-optic distributed acoustic sensors (DAS) and applications in railway perimeter security”. In: *Advanced Sensor Systems and Applications VIII*. Ed. by T. Liu and S. Jiang. Vol. 10821. SPIE, 2018, p. 1082102.

[40] M. Landrø et al. “Sensing whales, storms, ships and earthquakes using an Arctic fibre optic cable”. In: *Scientific Rep.* 12 (2022), p. 19226. DOI: https://doi.org/10.1038/s41598-022-23606-x.

[41] S. Dou et al. “Distributed acoustic sensing for seismic monitoring of The near surface: A traffic-noise interferometry case study”. In: *Scientific Rep.* 7 (2017), p. 11620. DOI: https://doi.org/10.1038/s41598-017-11986-4.

[42] Jun Shan Wey. *G.681: Distributed Fibre Optic Sensing System for Terrestrial Optical Transmission Systems*. Recommendation (Consent Stage). Consented on 2025-10-24. Work item for the 2025–2028 study period. Formerly G.dfos. International Telecommunication Union, ITU-T Study Group 15, Oct. 2025. URL: https://www.itu.int.

[43] J. S. Wey. “Distributed fiber optic sensing (DFOS) in telecom networks: industry trends and standards development”. In: *Journal of Lightwave Technology* (2025), pp. 1–7. DOI: https://doi.org/10.1109/JLT.2025.3597192.

[44] J. Wang et al. “Simulation and experimental studies of DWDM nonlinear phase/polarization/power crosstalk between DFOS and communication channels in 27.6Tb/s800ZR metro network”. In: *European Conference on Optical Communication (ECOC)*. IEEE/OPTICA. 2025, pp. 1–4.

[45] K. Abdelli et al. “Faulty branch identification in passive optical networks using machine learning”. In: *Journal of Optical Communications and Networking* 15.4 (2023), pp. 187–196. DOI: https://doi.org/10.1364/JOCN.475882.

[46] International Telecommunication Union – Radiocommunication Sector (ITU-R). *Framework and overall objectives of the future development of IMT for 2030 and beyond (Recommendation M.2160-0)*. Recommendation M.2160-0. Approved 13 Nov 2023. International Telecommunication Union, Nov. 2023. URL: file:///mnt/data/bd277bc7-0761-4dc0-a43f-399ac4edd094.png.

[47] V. Houtsma et al. "Real-time in-service ODN monitoring based on receiver-side DSP for next-generation PONs". In: *European Conference on Optical Communications (ECOC)*. VDE Verlag / VDE ITG. 2025, pp. C127–C135.

[48] D. V. Veen et al. "Polarization based fiber optic sensing and monitoring in real-time IM-DD based PON". In: *Optical Fiber Communications Conference and Exhibition (OFC)*. OPTICA/IEEE. 2025, pp. 1–3.

[49] S. J. Russell and D. Hill. "Distributed acoustic sensing (DAS) a real-world perspective, requirements, applications, and techniques". In: *International Conference on Optical Fiber Sensors (SPIE)*. SPIE. 2025, pp. 33–45.

[50] G. Wang et al. "Urban fiber based laser interferometry for traffic monitoring and analysis". In: *Lighwave Technology* 41.1 (2023), pp. 347–354. DOI: https://doi.org/10.1109/JLT.2022.3209499.

[51] B. Adonis et al. "Sensitive seismic sensors based on microwave frequency fiber interferometry in commercially deployed cables". In: *Nature Scientific Reports* 12.14000 (2022). DOI: https://doi.org/10.1038/s41598-022-18130-x.

[52] L. Zeni et al. "Brillouin optical time-domain analysis for geotechnical monitoring". In: *Rock Mechanics and Geotech Engineering* 12.14000 (2015), pp. 458–462. DOI: https://doi.org/10.1016/j.jrmge.2015.01.008.

[53] J. Li and M. Zhang. "Physics and applications of Raman distributed optical fiber sensing". In: *Light Science and App.* 11.128 (2022). DOI: https://doi.org/10.1038/s41377-022-00811-x.

[54] N. J. Lindsey, T. C. Dawe, and J. B. Ajo-Franklin. "Illuminating seafloor faults and ocean dynamics with dark fiber distributed acoustic sensing". In: *Science* 366.6469 (2019), pp. 1103–1107. DOI: https://doi.org/10.1126/science.aay5881.

[55] P. Jousset et al. “Fibre optic distributed acoustic sensing of volcanic events”. In: *Nature Communications* 13 (2022), p. 1753. DOI: https://doi.org/10.1038/s41467-022-29184-w.

[56] L. Costa et al. “Localization of seismic waves with submarine fiber optics using polarization-only measurements”. In: *Nature Communications* 2.86 (2023). DOI: https://doi.org/10.1038/s44172-023-00138-4.

[57] W. Ma et al. “Deep learning for the design of photonic structures”. In: *Nature Photonics* 15.2 (2021), pp. 77–90. DOI: https://doi.org/10.1038/s41566-020-0685-y.

[58] Y. LeCun, Y. Bengio, and G. Hinton. “Deep learning”. In: *Nature* 521 (2015), pp. 436–444. DOI: https://doi.org/10.1038/nature14539.

[59] D. E Rumelhart, G. E. Hinton, and R. J. Williams. “Learning representations by back-propagating errors”. In: *Nature* 323 (1986), pp. 533–536. DOI: https://doi.org/10.1038/323533a0.

[60] Y. Zhou et al. “Application of machine learning in optical fiber sensors”. In: *Measurement* 28 (2024), p. 114391. DOI: https://doi.org/10.1016/j.measurement.2024.114391.

[61] E. Chemali et al. “Long short-term memory networks for accurate state-of-charge estimation of Li-ion batteries”. In: *IEEE Transactions on Industrial Electronics* 65.8 (2018), pp. 6730–6739. DOI: https://doi.org/10.1109/TIE.2017.2787586.

[62] F. Usmani et al. “Deep learning based early earthquake detection through terrestrial optical networks”. In: *International Conference on Transparent Optical Networks (ICTON)*. IEEE. 2025, pp. 1–6.

[63] W. Zhang et al. “Displacement prediction of Jiuxianping landslide using gated recurrent unit (GRU) networks”. In: *Acta Geotechnica* 17 (2022), pp. 61367–1382. DOI: https://doi.org/10.1007/s11440-022-01495-8.

[64] Z. Zhan et al. “Optical polarization-based seismic and water wave sensing on transoceanic cables”. In: *Science* 371.6532 (2021), pp. 931–936. DOI: https://doi.org/10.1126/science.abe6648.

[65] F. Curti et al. “Statistical treatment of the evolution of the principal states of polarization in single-mode fibers”. In: *Journal of Lightwave Technology* 8.8 (1990), pp. 1162–1166. DOI: https://doi.org/10.1109/50.57836.

[66] S. Pellegrini et al. "Algorithm optimization for rockfalls alarm system based on fiber polarization sensing". In: *IEEE Photonics Journal* 15.3 (2023), pp. 1–9. DOI: https://doi.org/10.1109/JPHOT.2023.3281670.

[67] P. Barcik and P. Munster. "Measurement of slow and fast polarization transients on a fiber-optic testbed". In: *Optics Express* 28.10 (2020), pp. 15250–15257. DOI: https://doi.org/10.1364/OE.390649.

[68] *Istituto Nazionale di Geofisica e Vulcanologia*. Accessed: 20 April 2024 http://ismd.mi.ingv.it/ismd.php?tipo=lista.

[69] F. Usmani et al. "Earthquake early warning through terrestrial optical networks: A Bi-GRU attention model approach on SOP data". In: *Optical Fiber Communication Conference (OFC)*. OPTICA. 2024, Tu3J.2.

[70] Incorporated Research Institutions for Seismology (IRIS). *Syngine: A Community-Driven Software Platform for Seismological Data Science*. 2023. URL: https://ds.iris.edu/ds/products/syngine/.

[71] K. Feigl. "Overview and preliminary results from the PoroTomo project at brady hot springs, nevada: poroelastic tomography by adjoint inverse modeling of data from seismology, geodesy, and hydrology". In: *42nd Workshop on Geothermal Reservoir Engineering*. Stanford University. 2020, pp. 1–13.

[72] H. Awad et al. "Environmental surveillance through machine learning-empowered utilization of optical networks". In: *Sensors* 24.10 (2024), pp. 1–13. DOI: https://doi.org/10.3390/s24103041.

[73] H. Awad et al. "Polarization-based sensing in mesh optical networks for early earthquake detection". In: *European Conference on Optical Communication (ECOC)*. IEEE/OPTICA. 2024, pp. 1672–1675.

[74] H. Li and T. Qiu. "Continuous manufacturing process sequential prediction using temporal convolutional network". In: *International Symposium on Process Systems Engineering*. Elsevier. 2022, pp. 1789–1794.

[75] R. B. Herrmann, L. Malagnini, and I. Munafò. "Regional moment tensors of the 2009 L'Aquila earthquake sequence". In: *Bulletin of the Seismological Society of America* 101.3 (2011), pp. 975–993. DOI: https://doi.org/10.1785/0120100184.

[76] S. Yuan et al. "Near-surface characterization using a roadside distributed acoustic sensing array". In: *The Leading Edge* 39.9 (2020), pp. 646–653. DOI: https://doi.org/10.1190/tle39090646.1.

[77] V. D. E. Martijn et al. "Deep deconvolution for traffic analysis With distributed acoustic sensing data". In: *IEEE Transactions on Intelligent Transportation Systems* 24.3 (2023), pp. 2947–2962. DOI: https://doi.org/10.1109/TITS.2022.3223084.

[78] H. Awad et al. "Experimental validation on using optical network-as-a-sensor for earthquake early warning". In: *International Conference on Optical Network Design and Modeling (ONDM)*. IEEE. 2025, pp. 1–5.

[79] H. Awad et al. "Environmental sensing and localization via SOP monitoring of IM-DD optical data channels". In: *Optica Sensing Congress 2023 (AIS, FTS, HISE, Sensors, ES)*. OPTICA. 2023, JTu4A.8.

[80] R. Bratovich et al. "Surveillance of metropolitan anthropic activities by WDM 10G optical data channels". In: *European Conference on Optical Communication (ECOC)*. IEEE/OPTICA. 2022, Tu3B.6.

[81] Z. X. Liu et al. "A proposed method to measure weak magnetic field based on a hybrid optomechanical system". In: *Scientific Reports, Nature* 7.12521 (2017), pp. 1–8. DOI: https://doi.org/10.1038/s41598-017-12639-2.

[82] B. P. Abbott et al. "Observation of gravitational waves from a binary black hole merger". In: *Physical Review Letter* 116.6 (2016), pp. 061102–061118. DOI: https://doi.org/10.1103/PhysRevLett.116.061102.

[83] B. P. Abbott et al. "Observation of gravitational waves from a binary neutron star inspiral". In: *Physical Review Letter* 119.16 (2017), pp. 161101–161119. DOI: https://doi.org/10.1103/PhysRevLett.119.161101.

[84] Z. X. Liu and H. Xiong. "Highly sensitive charge sensor based on atom-assisted high-order sideband generation in a hybrid optomechanical system". In: *Sensors* 18.11 (2018), p. 3833. DOI: https://doi.org/10.3390/s18113833.

[85] X. Zuo et al. "Quantum-empowered fiber sensing metrology". In: *Photonics* 12.8 (2025), p. 763. DOI: https://doi.org/10.3390/photonics12080763.